TANBUL TECHNICAL UNIVERSITY ★ INSTITUTE OF SCIENCE AND TECHNOLOGY

OPTIMIZATION OF THE COUPLING AMONG AIRCRAFT ANTENNAS VIA THE GENETIC ALGORITHM

Ph.D. Thesis by
M. Emre AYDEMIR, M.Sc.
504002208

Date of submission : 10 June 2005
Date of defence examination: 19 September 2005

Supervisor (Chairman): Prof. Dr. Tayfun GÜNEL

Members of the Examining Committee: Prof.Dr. Filiz GÜNEŞ (Y.T.Ü.)

Prof.Dr. Ercan TOPUZ (İ.T.Ü.)

Prof.Dr. Selim ŞEKER (B.Ü.)

Assoc. Prof.Dr. Cevdet IŞIK (İ.T.Ü.)

OCTOBER 2005

İSTANBUL TEKNİK ÜNİVERSİTESİ ★ FEN BİLİMLERİ ENSTİTÜSÜ

UÇAK ANTENLERİ ARASINDAKİ KUPLAJIN GENETİK ALGORİTMA İLE OPTİMİZASYONU

DOKTORA TEZİ
Y. Müh. M. Emre AYDEMİR
504002208

Tezin Enstitüye Verildiği Tarih : 10 Haziran 2005
Tezin Savunulduğu Tarih : 19 Eylül 2005

Tez Danışmanı: Prof.Dr.Tayfun GÜNEL

Diğer Jüri Üyeleri: Prof.Dr.Filiz GÜNEŞ (Y.T.Ü.)

Prof.Dr.Ercan TOPUZ (İ.T.Ü.)

Prof.Dr.Selim ŞEKER (B.Ü.)

Doç.Dr.Cevdet IŞIK (İ.T.Ü.)

EKİM 2005

ACKNOWLEDGEMENTS

I am grateful to my supervisor, Professor Dr. Tayfun GÜNEL for his zealous guidance throughout this study. He has been very patient in working with me.

I would like to thank Professor Dr. Selim ŞEKER for his inspiration in the initial stages of the study.

This study has been implemented in the facilities of The Scientific and Technical Research Council of Turkey, National Research Institute of Electronics and Cryptology (TUBİTAK-UEKAE) in Gebze-Kocaeli. I would like to thank Assoc. Prof. Dr. Temel YALÇIN and Dr. Fatih ÜSTÜNER for their frank support in experimental part of the study.

I would like to thank Maj. General O. Kapani AKTAŞ, Colonel Dr. Sefer KURNAZ and Lt. Colonel Dr. Serdar KARGIN for their help in taking the grant for me to study at the TUBİTAK-UEKAE.

I would like to thank Colonel Cemal ÖKSÜZ for providing me the laboratory facilities of the Aeronautical Engineering Department of the Turkish Air Force Academy.

I also would like to thank Sergeant Mustafa ÖGEL and Mr. Sefa OGAN who helped me with the preperation of the scaled aircraft.

Finally, I would like to thank my wife and parents for their encouragement during the study.

16 May 2005 M. Emre AYDEMİR

TABLE OF CONTENTS

LIST OF ABBREVIATIONS

CE	: Communication-Electric
CEM	: Computational Electromagnetics Methods
CPGA	: Continuous Parameter Genetic Algorithm
CPMA	: Continuous Parameter Memetic Algorithm
DME	: Distance Measuring Equipment
EFIE	: Electric Field Integral Equation
EM	: Electromagnetics
EMC	: Electromagnetic Compatibility
EMI	: Electromagnetic Interference
EW	: Electronics Warfare
FCC	: Federal Communications Commission
FD	: Frequency Domain
FDTD	: Finite Difference Time Domain
GTD	: Geometrical Theory of Diffraction
GPS	: Global Position System
IFF	: Identification of Friend or Foe
MFIE	: Magnetic Field Integral Equation
MoM	: Method of Moments
NEC	: Numerical Electromagnetics Code
PTD	: Physical Theory of Diffraction
RADAR	: Radio Detection and Ranging
RFI	: Radio-Frequency-Interference
RWR	: Radar Warning Receiver
SIG	: Structural Interpolation and Gridding
SNEC	: Super Numerical Electromagnetics Code
T/R	: Transmitter/Receiver
UHF	: Ultra High Frequency
UTD	: Uniform Theory of Diffraction
VHF	: Very High Frequency

LIST OF TABLES

LIST OF FIGURES

LIST OF SYMBOLS

$\boldsymbol{E}$	: Electric Field Vector
$\boldsymbol{H}$	: Magnetic Field Vector
$\boldsymbol{D}$	: Electric Flux Density Vector
$\boldsymbol{B}$	: Magnetic Flux Density Vector
E_k	: k (x, y or z) Component of Electric Field
H_k	: k (x, y or z) Component of Magnetic Field
E_s	: Scattered Electric Field
E_i	: Incident Electric Field
μ_o	: Free Space Permeability
μ_r	: Relative Permeability
ε_0	: Free Space Permittivity
ε_r	: Relative Permittivity
σ	: Conductivity
σ^*	: Magnetic Conductivity
V	: Voltage
I	: Current
c, u_o	: Speed of the Light in Free Space
γ	: Propagation Constant
α	: Attenuation Constant
ω	: Angular Frequency
f	: Frequency
f_r	: Resonant Frequency
k	: Wave Number
t	: Time
λ_o	: Free Space Wavelength
Γ	: Reflection Coefficient
Z_0	: Intrinsic Impedance of the Free Space

OPTIMIZATION OF THE COUPLING AMONG AIRCRAFT ANTENNAS VIA THE GENETIC ALGORITHM

SUMMARY

In this study, the optimization of the electromagnetic interference induced by two VHF-UHF transreceiver antennas on F-4 Phantom fighter aircraft is aimed. The transreceiver antennas are modelled as single monopole antennas therefore the problem is reduced to antenna to antenna coupling optimization.

Numerical analysis and measurement methods are used in the study. The Method of Moments (MoM) is selected for computing the coupling between the antennas. In the numerical analysis, the wire-grid model of the aircraft is constructed, coupling between the antennas is calculated and optimized by using MATLAB and SuperNEC. The Continuous Parameter Genetic and Memetic Algorithms (CPGA, CPMA) are chosen as the optimization methods.

In the measurement process, coupling and S-parameters are measured on a 1:10 scaled model in an anechoic chamber. The measured data is compared with the results of the numerical analysis.

The outline of the thesis is as follows:

- In Section 1, definitions of Electromagnetic Compatibility (EMC) and Electromagnetic Interference (EMI) are done, The studies up to date are explained and the innovation of the study in the field is expressed.

- In Section 2, the electromagnetic interference is investigated and coupling mechanisms by radiation are dealt with. MoM, CPGA and CPMA are explained in detail. The features and advantages of MoM electromagnetic calculation method is explained in detail, calculation requirements and precisions are given.

- In Section 3, the selected aircraft and the possible source of EMI sub-systems are explained.

- In Section 4, the numerical analysis is explained. After the suitable method is selected, the program algorithm is explained in detail. Preperation of the numerical wire-grid model for the aircraft is explained. Results are given at the end of the section.

- In Section 5, first the construction of the scaled model is explained. Then the measurement setup and parameters are defined and the measurement results are given.

- And finally, in Section 6, the results obtained at the end of the study are evaluated and recommendations for further studies are proposed.

The originality of this study is that it combines the MoM Computational Electromagnetics (CEM), CPGA and CPMA optimization methods for the minimization of coupling between the F-4 Phantom aircraft antennas. When applied together, it is seen that these methods solve very complex and time-consuming problem efficiently. The matching between the numerical analysis and measurement results is an indicator of the accuracy of the selected method. Therefore, it can be concluded that as soon as the numerical model and numerical analysis parameters are set up correctly:

- An accurate and low-cost alternative for the expensive and time-consuming measurement methods and,

- A suitable tool for verifying the validity of the measurement results.

UÇAK ANTENLERİ ARASINDAKİ KUPLAJIN GENETİK ALGORİTMA İLE OPTİMİZASYONU

ÖZET

Bu çalışmada F-4 Phantom savaş uçağı yerleştirilmesi planlanan iki UHF-VHF telsizin birbirlerinin antenleri üzerinde meydana gelebilecek girişim etkisinin optimizasyonu hedeflenmiştir. Elektromanyetik girişim kaynağı olan telsiz alıcı-vericileri basit monopol antenler ile modellenmiş, böylece problem antenden antene kuplaj optimizasyonuna indirgenmiştir.

Çalışmada yöntem olarak ise sayısal analiz ve ölçüm metodları kullanılmıştır. Moment Yöntemi (The Method of Moments - MoM) antenler arasındaki kuplajın hesaplanmasında kullanılmıştır. Sayısal analizde uçağın tel ızgara modeli oluşturulmuş, MoM tabanlı Super NEC programı ile MATLAB birarada kullanılarak antenler arasındaki kuplaj hesaplanmış ve optimize edilmiştir. Optimizasyon metodu olarak Sürekli Parametreli Genetik ve Memetik Algoritmalar (Continuous Parameter Genetic & Memetic Algorithm - CPGA, CPMA) kullanılmıştır.

Ölçüm yönteminde ise, 1:10 ölçekli bakırdan imal edilen uçak modeli üzerinde tam yansımasız odada kuplaj ve S-parametreleri ölçümleri yapılmıştır. Ölçüm sonuçları, sayısal analiz sonuçlarıyla karşılaştırılmıştır.

Tezin ana hatları aşağıdaki gibidir:

- Bölüm 1'de Elektromanyetik Uyumluluk ve Elektromanyetik Girişimin (Electromagnetic Compatibility–EMC, Electromagnetic Interference-EMI) tanımları yapılmış, problemin detaylarıyla tanımlanmasından sonra seçilen yöntemler belirtilmiş ve bu konuda günümüze kadar yapılan çalışmalar listelenmiştir. Çalışmanın literatüre getireceği yenilik belirtilmiştir.

- Bölüm 2'de Elektromanyetik Girişim incelenmiş ve ışıma ile kuplaj mekanizmaları ele alınmıştır. MoM, CPGA ve CPMA detaylara inilerek açıklanmıştır. MoM elektromanyetik hesaplama yöntemi kendine has avantajları ve özellikleri ele alınarak açıklanmış, hesaplama ihtiyaçları ve hassasiyetleri verilmiştir.

- Bölüm 3'te, seçilen uçak tanıtılmış ve platform üzerinde bulunan EMI kaynakları ele alınmıştır.

- Bölüm 4'de sayısal analizi açıklanmıştır. Uçak için sayısal tel-ızgara modelinin hazırlanışı anlatılmıştır. Kuplajın hesaplanması detaylı bir şekilde anlatılmış ve elde edilen sonuçlar bölüm sonunda verilmiştir.

- Bölüm 5'te öncelikle ölçüm metodu için gereken ölçekli modelin inşası anlatılmıştır. Daha sonra ölçüm düzeneği ve parametreleri tanımlanarak ölçüm sonuçları verilmiştir.

- Son olarak Bölüm 6'da, çalışma sonunda elde edilen sonuçlar değerlendirilmiş ve bu doğrultuda gelecekte yapılabilecek çalışmalar için öneriler getirilmiştir.

Bu çalışmanın özgünlüğü, F–4 Phantom uçağının antenleri arasındaki kuplajın minimizasyonu için MoM ile CPGA veya CPMA metodlarının birarada kullanılmasıdır. Birarada uygulandıklarında bu metodların çok karmaşık ve zaman alıcı problemleri etkili bir şekilde çözdükleri görülmüştür. Sayısal analiz ve ölçüm sonuçları arasındaki uyumluluk seçilen yöntemin doğruluğunun bir göstergesi olarak kabul edilebilir. Böylece, sayısal model ve sayısal analizin parametreleri uygun bir şekilde seçildiklerinde:

- Maliyetli ve zaman alıcı ölçüm metodları için doğru ve düşük maliyetli bir alternatif ve

- Ölçüm sonuçlarının doğrulanması için uygun bir araç olduğu söylenebilir.

1. INTRODUCTION

High density of electronic equipment, receiver and transmitters used in modern aircraft makes Electromagnetic Interference (EMI) of high priority concern [1] . In such platforms, providing Electromagnetic Compatibility (EMC) among systems is difficult due to the simultaneous operation modes. Antenna mounting on an aircraft needs special attention and experience. The conducting surfaces of these aircraft seriously affect the radiation patterns of the antennas in a manner of re-radiation or cross polarization (Figure 1.1). If the difference between the operation frequencies of two antennas is not adequate, the simultaneous operation of these two antennas may yield serious problems. Coupling power from one transmitter to another may cause problem or malfunctions at the output stages. In this study, minimization of the negative effects of antennas on each other placed on aircraft (coupling optimization) is aimed. The study aims a systematical EMC in which devices and sub-systems are modelled as black boxes having pre-defined input-output characteristics.

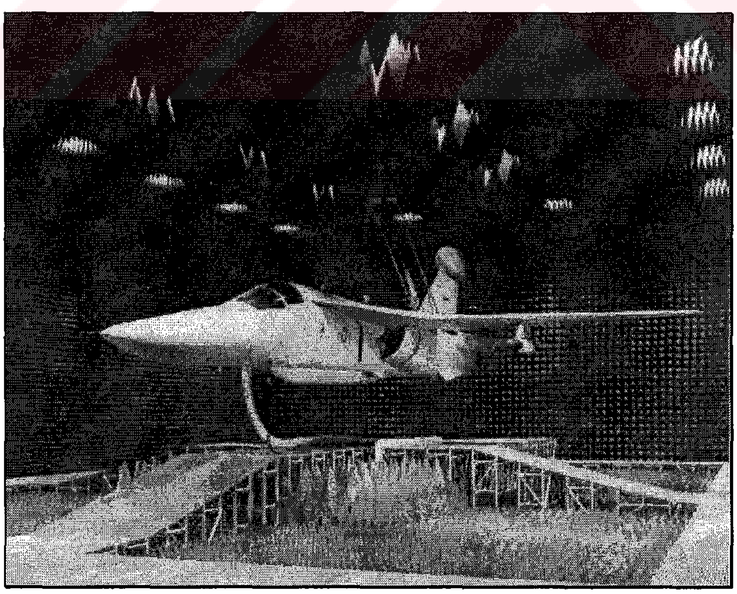

Figure 1.1: Airborne platforms provide challenges for the EMC designer [1]

The selected method for electromagnetic modelling is the Method of Moments (MoM) [3] which is an integral equation based sub-class of Computational Electromagnetics (CE) in the frequency domain. For the optimization part, Continuous Parameter Genetic and Memetic (CPGA, CPMA) [4,5] stochastic search algorithms are chosen. The combination of MoM and CPGA or CPMA methods for the minimization of the coupling between the aircraft antennas is unique in the literature. The study is based on analysis and measurement approaches. When implemented together, the match in results of these two methods becomes an indicator of the accuracy and reliability of the methods involved.

1.1. Definition of Electromagnetic Compatibility

Almost every aspect of modern life is significantly influenced by and depends on the use of the electromagnetic spectrum. This permits production and transmission of electrical power, communications, navigation, radar and the like. Without the use of this valuable and essential natural resource, the basic nature of our society would be completely different.

Eletromagnetic compatibility (EMC) is a necessary condition for effective communication-electronic (CE) system performance [1]. EMC is the ability of equipments and systems to function as designed in their intended operational environment without adversely affecting the operation of, or being interfered adversely by, other equipments or systems. This sort of interference is called Electromagnetic Interference (EMI). Thus, the manner and efficiency in which modern life is conducted depends on the ability to achieve and maintain EMC.

In order to permit efficient use of the frequency spectrum, engineers, technicians and users responsible for the planning, design, development, installation and operation of telecommunications systems must have a methodology for achieving EMC. The control or reduction of EMI or its predecessor names, radio noise, electrical noise or radio-frequency-interference (RFI) is a rapidly expanding technology. It covers the frequency spectrum from dc to about 40 GHz. EMI can result in a jammed radio, heart-pacer failures, navigation errors and many other nuisance or catastrophic events. Therefore, it follows that this spectrum pollution problem has reached international levels of concern and must be dealt with in proportion to the safety and economic impact involved.

The basic EMC requirement is to plan, specify and design telecommunication systems that can be installed in their operational environment without creating or being susceptible to interference. In order to help satisfying this requirement, careful consideration must be given to a number of factors that influence EMC. It is particularly necessary to consider major sources of EMI, modes of coupling and points or conditions of susceptibility.

1.1.1. Effects of EMI

EMI may directly influence the performance of any CE equipment or system, and it can indirectly affect the overall accomplishment of an operation or mission [2]. Examples of direct influences of EMI on system performance are: false targets and missed targets in a radar display system, wrong navigation data or landing system errors in an aircraft, lost or garbled messages in a communications system, false commands to a missile or electro-explosive device or triggering a heart pacemaker demand-mode of operation. Some resulting indirect effects corresponding to the above include: false alerts in an air-defense system as a result of false targets, surprise enemy attacks as a result of missed targets, aircraft mid-air collisions as a result of navigation errors, aircraft crashes while landing because of altitude or glide-slope errors, ineffective control of riots or fires because of lost or garbled emergency fire or police communications, accidental launching of missiles or detonation of explosives because of wrong electrical commands and the fainting, collapse or even death of the person having a heart pacemaker. All of these effects, both direct and indirect, have happened as a result of EMI. They can recur, and with the increase of EMI sources and receptors every year the situations will probably become more frequent.

1.2. Selected Methods

Two methods are applicable for analysing the problem of antenna-to-antenna coupling. The first one is the calculation of coupling among the antennas by analysing the system. This procedure is called the analysis method which is based on MoM. In order to find the optimum antenna positions, CPGA or CPMA are used with the MoM. The second one is the measurement method in which the coupling level is found by measurements made on the real or scaled three-dimensional model. In this study, the first step is the analysis which is based on MoM with CPGA or CPMA. Next, a 1:10 scaled model is constructed and measurements are implemented in the anechoic chamber for verification of the results.

1.3. Literature Search

In the search for literatre on the subject, around 55 papers are found in IEEE Xplore and NATO AGARD scientific databases. The initial studies made on aircraft EMI were mostly based upon the effects of interfering devices on the onboard radio and navigation systems [6]. Lee K. and Marin L. published some of the first studies, which were based upon finding the wide-band radiation patterns of the aircraft antennas [7]. In their study, the aircraft was modelled as a combination of simple objects like cylinder and cube. In a following study by Burnside W., a Boeing 737 aircraft was modelled as a combination of elliptical and cylindirical objects and the near field radiation patterns of the antennas on aircraft were obtained by high accuracy [8].

In the 1980's, C. Ryan and W. Cooke tried Geometrical Theory of Diffraction (GTD) methods instead of the Numerical Methods for Aircraft EMI problems [9]. In a short period of time, this method was applied for a wide range of applications [10]. O. Givati and et.al. found the near and far-field radiation patterns of antennas mounted on a Mirage fighter aircraft by using the Method of Moments (MoM) and verified the results by making experients using the anechoic chamber on a 1:10 scale model [11].

As the processing capabilities of computers improved in time, EMI problems at higher frequencies could be investigated with higher accuracy in less computation time [12-14]. In a recent study by Dr. Fatih Üstüner, the EMI problem caused by an Electronic Warfare (EW) system on the onboard transmitter/receiver antennas of an UH-1 general utility helicopter was simulated by personal computers (PC) and measurements were made at the anechoic chamber on a scaled model [15]. In this study, the emphasis was on the effects of the helicopter rotor on the coupling levels of the onboard antennas.

One of the latest studies in the literature is the one made by F. Obelleiro and his colleauges. In this study, the desired radiation patterns were acquired for the antenna arrays on the aircraft fuselage [16]. The innovation brought by this study was besides obtaining the desired radiation pattern, keeping the current densities low on precise regions of the fuselage inflicted by the antenna arrays. Also in a very recent study, Eric M. Koper and Stephen W. Schneider also implemented the genetic algorithm for EMI reduction among VHF antennas on a Boeing-747. However, in their study they utilized the Uniform Theory of Diffraction (UTD) method with some approximations due to computational difficulties [17].

On the other hand, the Genetic Algorithms (GA) developed by Dr Holland in the 1990's have found a wide range of scientific applications. The GA was inspired from the genetical processes in the live organisms' reproduction mechanisms and they accepted wide recognition in optimization based engineering problems [4]. In 1995 R.L. Haupt showed that the GA's can be succesfully applied for antenna design techniques [18]. While the first EM applications of the GA were limited with simple dipole antenna designs, in time, the range of applications are widened [19-30]. One of the recent studies in the field is done by J.M. Jonson and Y.R.Samii. In this study, a combination of the GA and MoM is used in the design of microstrip integrated antennas [31]. In a very recent study, S. Caorsi et.al have tried a different version of the Genetic Algoritm called “Memetic Algorithm” [5] in a study for detecting buried objects. In our study both the CPGA (Continuous Parameter Genetic Algorithm) and CPMA (Continuous Parameter Memetic Algorithm) methods are used for the optimization method.

1.4. The Contribution of the Study to the Literature

The combination of methods selected for the study is unique. These methods are being used extensively in their own fields, however, we have not met a study that combines the MoM with the CPGA or CPMA methods for EMI optimization between the aircraft antennas in the literature. Besides being a novel scientific approach for the problem of coupling optimization for the antennas, the study is also well suited for the requirements of military & civilian vehicle or installation antenna placement decisions. The methods and software selected for this study are up-to-date and we beleive that the study will contribute to the aviation electronics and communications research and develeopment (R&D) activities.

2. EMI AND ANALYSIS METHOD

In this section the definition of the EMI will be done and the selected analysis method will be explained.

2.1. Sources of EMI

Any electrical, electromechanical or electronic device is a potential source of EMI. In general, EMI sources can be classified either as transmitters (equipment whose primary function is to intentionally generate or radiate electromagnetic signals) or incidental sources (equipments that generate electromagnetic energy as an unintended product in the process of performing their primary function). Sometimes sources of EMI are divided into natural and man-made sources. Figure 2.1 [1] shows such an organization.

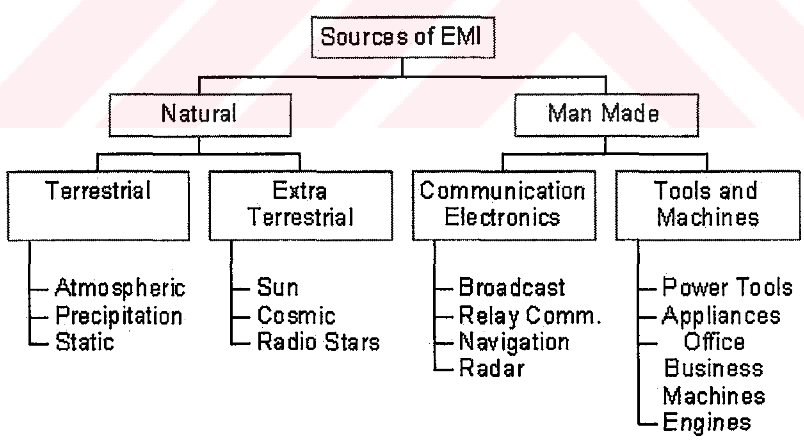

Figure 2.1: Sources of EMI

All electrical equipments can be potential sources of incidental radiation. Although the levels associated with these sources are usually relatively low, they often are the cause of interference because of their broadband characteristics. Here, significant emissions occupy several octaves or more the frequency spectrum. Some of the more important sources include: power lines, automobile engine ignition systems, fluorescent lamps, electrical motors, switches and relays [2]. Because the limitations on system performance may be determined by the environmental signals and ambient noise levels present in the vicinity of a potentially susceptible device, it is important to consider these sources of EMI in planning and designing systems.

Transmitters generate electromagnetic energy not only in the basic or intended frequency range, but also over a wide range of other frequencies on both sides of the fundamental carrier, harmonics of the fundamental and other undesired or spurious frequencies. These undesired emissions result from carrier spreading by the baseband transmitter modulation spectrum, production of broadband noise in the output stages and generation of harmonics of the fundamental as a result of nonlinearities in the equipment output stages. Because of transmitter nonlinearities, signals from two or more transmitters can heterodyne in the output stages of one to produce additional signals at totally different frequencies. This is called "transmitter intermodulation". In designing a telecommunication system, all of these transmitter outputs must be carefully considered.

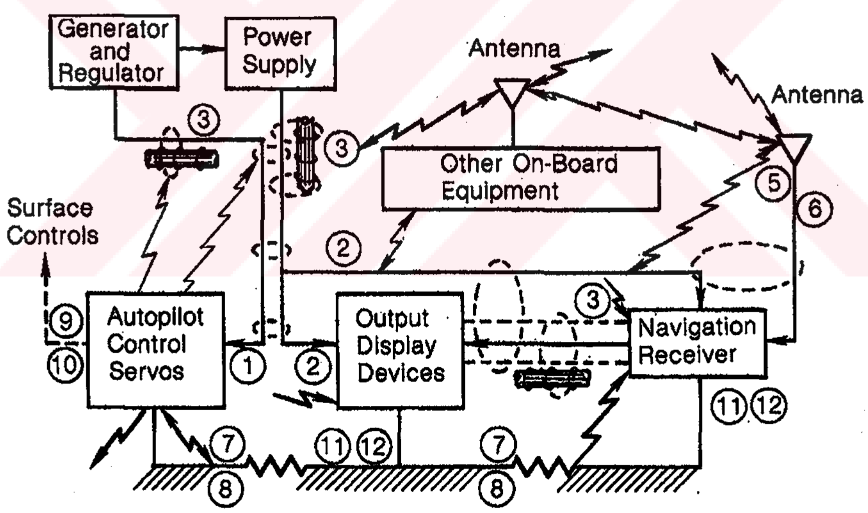

1. Power-Cable Conducted Emission
2. Power-Cable Conducted Susceptibility
3. Interconnecting-Cable Conducted Emission
4. Interconnecting-Cable Conducted Susceptibility
5. Antenna-Lead Conducted Emission
6. Antenna-Lead Conducted Susceptibility
7. Common Ground Impedance Emission Coupling
8. Common Ground Impedance Suscept. Coupling
9. H-Field Radiation
10. E-Field Radiation
11. H-Field Susceptibility
12. E-Field Susceptibility

Figure 2.2: Paths of coupling on aircraft [2]

2.2. Paths of Coupling

Emissions may be coupled (Figure 2.2) by one or more paths from the interference source to the susceptible receiving device(s) [1]. Basically, these paths are classified as either (1) conduction patlıs, which include all forms of direct hardline, wire or cable coupling, or (2) radiation paths, which involve propagation through the environment or induction (near-field) therein.

Among all of the EMI paths in Figure 2.2, the most important one is generally the coupling between antennas in which the conducting surface of the aircraft has significant effects.

2.3. Analysis Methods

The electric and magnetic fields emerging from complex metal structures sheltering cable and antennas can not be solved by direct application of Maxwell's equations. In analysis of such problems, methods used for calculating the electric fields emerging from point scatterers are no adequate. Such problems can only be solved with Computational Electromagnetics Methods (CEM) which are Numerical or Asymptotical Methods (Figure 2.3). Methods of all types, including analytical techniques, are very important and widely used today, and there is much overlap between these three broad areas. The historical development of the CEM methods can be summarized as:

Mid 1900's, Asymptotic Methods [6-9]:

- High frequency regime (Uniform Theory Of Diffraction (UTD))

Late 1900's: Numerical Methods:

- Finite Difference Time Domain Method (FDTD) [10]
- The Method of Moments (MOM) [3]
- Finite Element Method (FEM) and 1971–TLM (Transmission Line Matrix) [11]

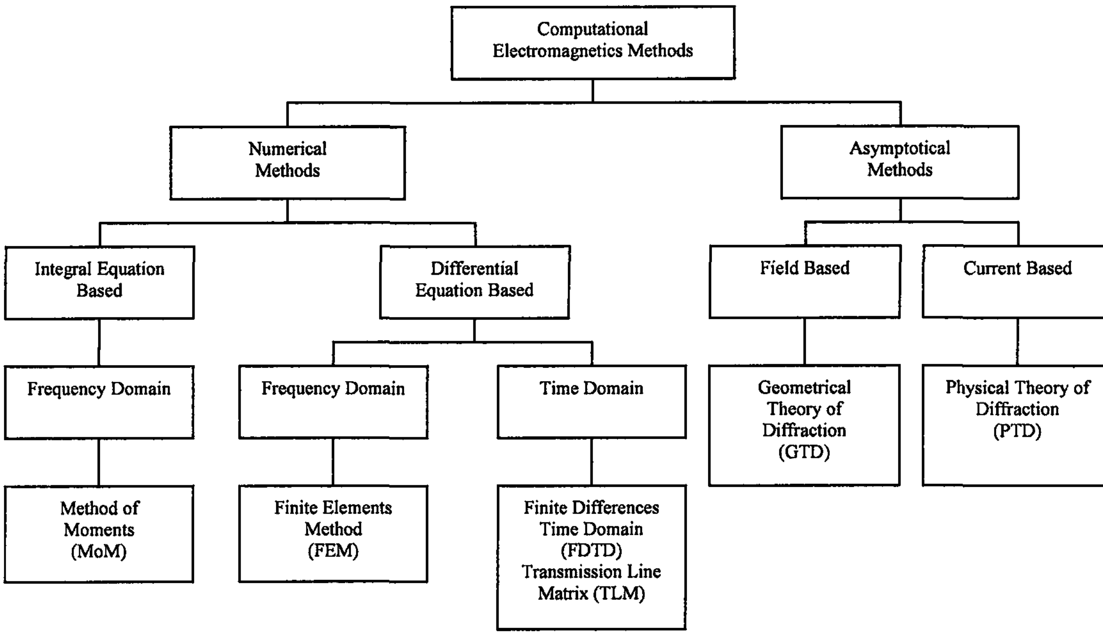

Figure 2.3: CEM methods [15]

In the MoM, the dimensions of the Electomagnetic structure must be comparable with the wavelength as shown in Figure 2.4 [15]. However, the Asymptotical Methods are used in cases where the dimensions of the electromagnetic structure are much higher than the wavelength applied.

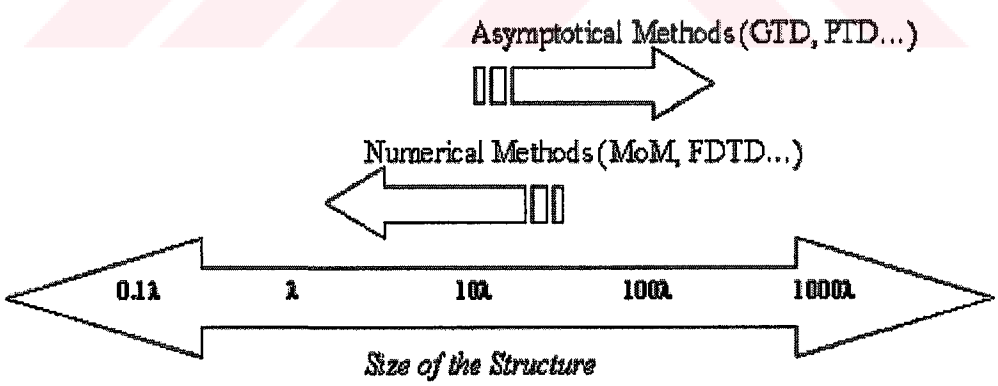

Figure 2.4: The effective utilization range of the CEM

2.3.1. Types of CEM methods

The main categories of CEM methods in Figure 2.3 which are used in electromagnetics are:

- Differential equation based methods: FEM, FDTD, and TLM
- Integral equation based method: MoM
- Uniform Theory of Diffraction methods based on asymptotic approximations: GTD, PTD.

As a summary, UTD methods are more flexible than analytical solutions, but accuracy of approximation is difficult to improve. MoM and FEM are highly flexible, but computationally intensive for large or complex problems. For this study, both approaches are tested and the suitable method is selected as the MoM in the Numerical Analysis section.

2.3.1.1. The Method of Moments

For a given antenna structure the conductors can be broken into "segments", and the currents on the segments can then be determined [3,35]. The "moment" is numerically the size of the current times the vector describing the little segment (length and orientation). One matches the currents at the ends of the segments. A set of "basis functions" may be assumed into which the current distributions are decomposed.

In the simplest case, the basis functions are rectangular approximations to the Dirac delta function. Because the widths of the rectangular sections are non-zero, only a finite (reasonably small) number of them are needed to cover the antenna wire structure. The next more complicated basis functions are triangular in shape. This gives a smoother approximation to the current distribution, in which the current distribution is piecewise-linear between the matching points. In general, the "n-th moment" is obtained by integrating the product of the Green's function with the n-th basis function. In the case of rectangular basis functions this gives the interpretation of "moment" set out simply above. However, for more complicated basis function shapes the "moment" is a more abstract concept. For example, we could start with an infinite set of basis functions which were the sinusoidal and co-sinusoidal Fourier components with spatial period equal to the size of the antenna. We then truncate this infinite Fourier series to make the calculation tractable in a sensible time on a computer.

The MoM, unlike conventional propagation models, takes into account the total complex structure as appropriate. Complex structures may be represented by thin wires, wire grids or surface patches as appropriate to the specific problem. Examples of the representation of an aircraft are shown in Figures (2.5-7) [2]. The stick model representation would be used at low frequencies where the wavelength is large relative to the radius of the fuselage or the cord of the wings or stabilizers. Thus, for low frequencies, the aircraft surfaces may be represented as thin wires. At higher frequencies, the detailed geometry of the aircraft becomes important and it is necessary to model the aircraft in terms of wire grids or surface patches.

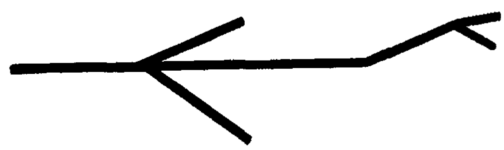

Figure 2.5: Thin wire representation of an aircraft for MoM

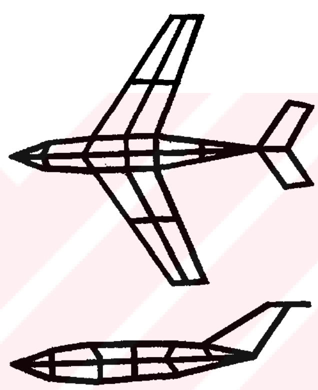

Figure 2.6: Wire-grid representations of aircraft for MoM

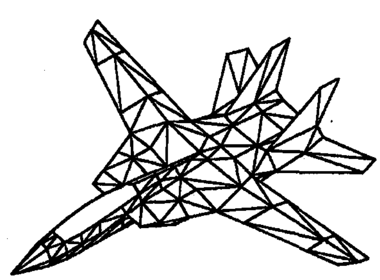

Figure 2.7: Triangular surface patch representation of aircraft for MoM

The MoM starts from deriving the currents on each segment, or the strength of each moment, by using a coupling Green's function. This Green's function incorporates electrostatic coupling between the moments for if the spatial change of the currents is known accurately then one can compute the build up of charges at points on the structure. There is some debate as to whether the electrostatic coupling is as accurately calculated as is the current coupling; and it is usual to approximate antennas having area by wire grid approximations, which also have to be chosen extremely carefully. As one always is presented with a computed result for a simulation, even if the model is in error, one can see that replacement of areas of metal by wire grids requires physical insight into the processes involved, rather than blind application of an algorithm. Most of the EM problems can be expressed as:

$$L\Phi = g \tag{2.1}$$

where L is a linear operator, g is a known source function and Φ is the function to be determined [15]. The MoM is a computational technique used in the solution of this equation. The procedure is as follows:

- Formation of the integral equation representing the EM problem
- Conversion of the integral equation to a matrix equation by using the basis and weighting functions
- Calculation of the matrix equation and
- Solution of the matrix equation and calculation of the desired parameters.

The two integral equation formulations upon which the MoM is based are the electric field integral equation (EFIE) and the magnetic field integral equation (MFIE). EFIE is appropriate for thin-wire structrues while MFIE is suitable for structures having flat surfaces and volume.When the EFIE is applied onwire structures, the following assumptions are assumed:

- Currents perpendicular to the wire are neglected w.r.t. the wires parallel ones.
- The circular variation of the current parallel to the wire axis is neglected.
- The current is expressed as a part of the wire axis.

These assumptions are valid only when the wire radius is much smaller than the wavelength and the wire length. The MoM is generally applied at the EM problems utilizing the EFIE.

The MoM is a low frequency approach. The wavelength decreases as the frequency increases and the number of segments length of which are proportional with the wavelength increases. The dimension of the matrix representing the EM problem is proportional with the square of the number of segments. Therefore the solution of big matrices is time consuming.

2.4. Searching Techniques

All the problem solving and optimisation techniques involve a decision about the goodness, or utility, of a method and an object way of evaluating that decision. For problem solving and optimisation in engineering, most of the traditional search techniques are divided into two categories [36], blind search and heuristic search. Based on the structure of the search technique, blind search is suitable for simple problems, which are relatively straightforward, no guiding, and presence of definite result [37]. In addition, in the blind search, it is possible to find no solution during the search operation. Moreover, Depth-First Search and Breadth-First Search are the typical examples. Heuristic search technique is designed to solve the relatively difficult problems. They are based on a structured searching methodology, and a guidance mechanism to search towards a better solution. In addition, this kind of search technique is able to provide a nearest solution, when there is no definite solution to the particular problem.

Moreover, Hill-climbing Search, Beam-Search, and Best-First Search are the current examples of heuristic search techniques. Indeed, these search techniques work properly when searching for any solution that satisfy the target requirements and also tries to guide the search in order to reduce the time and effort involved in searching. In addition, the Hill-climbing search techniques are commonly employed to find the optimal solution in most engineering search problems. However, in many situations it is not possible to find a definite solution, and the only solutions are the best results the techniques find. In addition, by using these search techniques, it is possible to stick to local optimal rather than the global optimal.

For search problems without a known solution, there are several traditional searching techniques. A-Star, MiniMax, and Alpha-Beta Search are commonly used for optimal searching in engineering problems. Higher structural algorithms are applied in these searching techniques. Moreover, many recent studies have focused on using Meta-heuristics searching techniques in the search for the global optimal. In addition, Meta-heuristics is a general structure for heuristics with continuous changing and alternating solution for solving problems. By combining with biological metaphor, Artificial Intelligent techniques are implemented for optimal searching. Ant colony optimisation [38] Neural Networks, Scattered Search, Tabu Search [39], Target Analysis, Simulated Annealing [40] and Genetic Algorithm [4] are some of the most popular Meta-heuristics searching techniques. In addition, the GA search technique is commonly used in solving engineering optimisation problems over the last ten years. It is a fast and efficient global search technique in multiple objective optimization.

2.4.1. The Genetic Algorithm

GA's are numerical search algorithms, which are based on both natural heredity and natural selection in order to search for the optimal point. In addition, it is a computer-based search technique achieved by replicating nature's genetic mechanisms of living organism. When compared with other traditional optimisation techniques, it is seen that GA's are more suitable to implement for a broad range of problems, and there normally are three major purposes for the implementation of GAs;

- They create an opportunity to recognise some processes of the spontaneous development and spontaneous dynamics.
- GAs are able to help the understanding and improving techniques in computer science, and,
- GAs can solve the wide range of difficult problems for the major usage in physics, life, computer and social sciences, and in engineering [41].

Moreover, by co-operating with other Intelligent Systems, such as Neural Networks, the stochastic GAs techniques can help to identify some important factors in the particular optimisation, when the absence of clear idea the relationship between these factors and the problem in the research areas.

2.4.1.1. Genetic Algorithm overview

One of the central challenges of computer science is to get a computer to do what needs to be done, without telling it how to do it [42]. Genetic programming addresses this challenge by providing a method for automatically creating a working computer program from a high-level problem statement of the problem.

Genetic programming is a domain-independent method that genetically breeds a population of computer programs to solve a problem. Specifically, genetic programming iteratively transforms a population of computer programs into a new generation of programs by applying analogs of naturally occurring genetic operations. The genetic operations include crossover, mutation, reproduction, gene duplication, and gene deletion.

2.4.1.2. Preparatory steps of genetic programming

Genetic programming starts from a high-level statement of the requirements of a problem and attempts to produce a computer program that solves the problem. The human user communicates the high-level statement of the problem to the genetic programming system by performing certain well-defined preparatory steps.

- The five major preparatory steps for the basic version of genetic programming require the human user to specify:

- The set of terminals (e.g., the independent variables of the problem, zero-argument functions, and random constants) for each branch of the program,

- The set of primitive functions for each branch of the to-be-evolved program,

- The fitness measure (for explicitly or implicitly measuring the fitness of individuals in the population),

- Certain parameters for controlling the run, and

- The termination criterion and method for designating the result of the run.

Figure 2.8 shows the five major preparatory steps for the basic version of genetic programming. The preparatory steps (shown at the top of the figure) are the human-supplied input to the genetic programming system. The computer program (shown at the bottom) is the output of the genetic programming system.

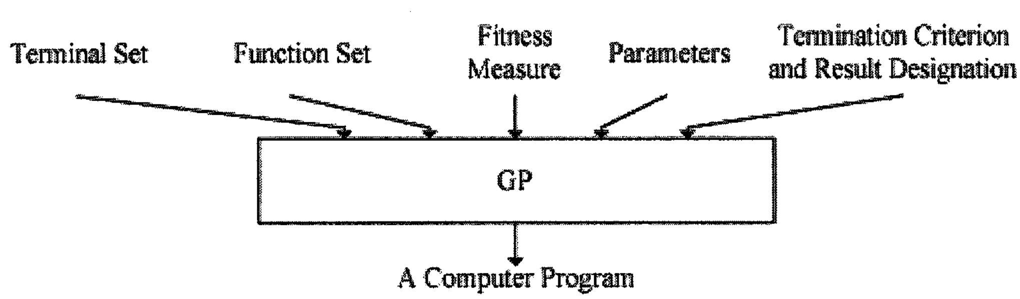

Figure 2.8: Five major preparatory steps for the genetic programming [36]

2.4.1.3. Executional steps of genetic programming

Genetic programming is problem-independent in the sense that the flowchart specifying the basic sequence of executional steps is not modified for each new run of the problem. There is usually no discretionary human intervention or interaction during a run of genetic programming (although a human user may exercise judgment as to whether to terminate a run).

Figure 2.10 is a flowchart showing the executional steps of a run of genetic programming. The flowchart shows the genetic operations of crossover, reproduction, and mutation as well as the architecture-altering operations. This flowchart shows a two-offspring version of the crossover operation. The executional steps of genetic programming are as follows:

1. Randomly create an initial population (generation 0) of individual chromosomes composed of the available genes and cost functions. The encoding of the chromosomes is given in Figure 2.9.

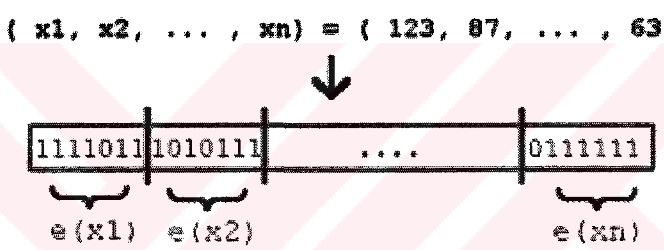

Figure 2.9: Encoding of the chromosomes in the binary Genetic Algorithm (BGA)

2. Iteratively perform the following sub-steps (called a *generation*) on the population until the termination criterion is satisfied:

   a. Execute each program in the population and ascertain its fitness (explicitly or implicitly) using the problem's fitness measure.

   b. Select one or two individuals from the population with a probability based on fitness (with reselection allowed) to participate in the genetic operations in (c).

   c. Create new individuals for the population by applying the following genetic operations with specified probabilities:

      i. *Reproduction:* Copy the selected individual to the new population.

      ii. *Crossover:* Create new offsprings for the new population by recombining randomly chosen parts from two selected induviduals (Figure 2.11).

iii. *Mutation:* Create one new offspring program for the new population by randomly mutating a randomly chosen part of one selected induvidual (Figure 2.12).

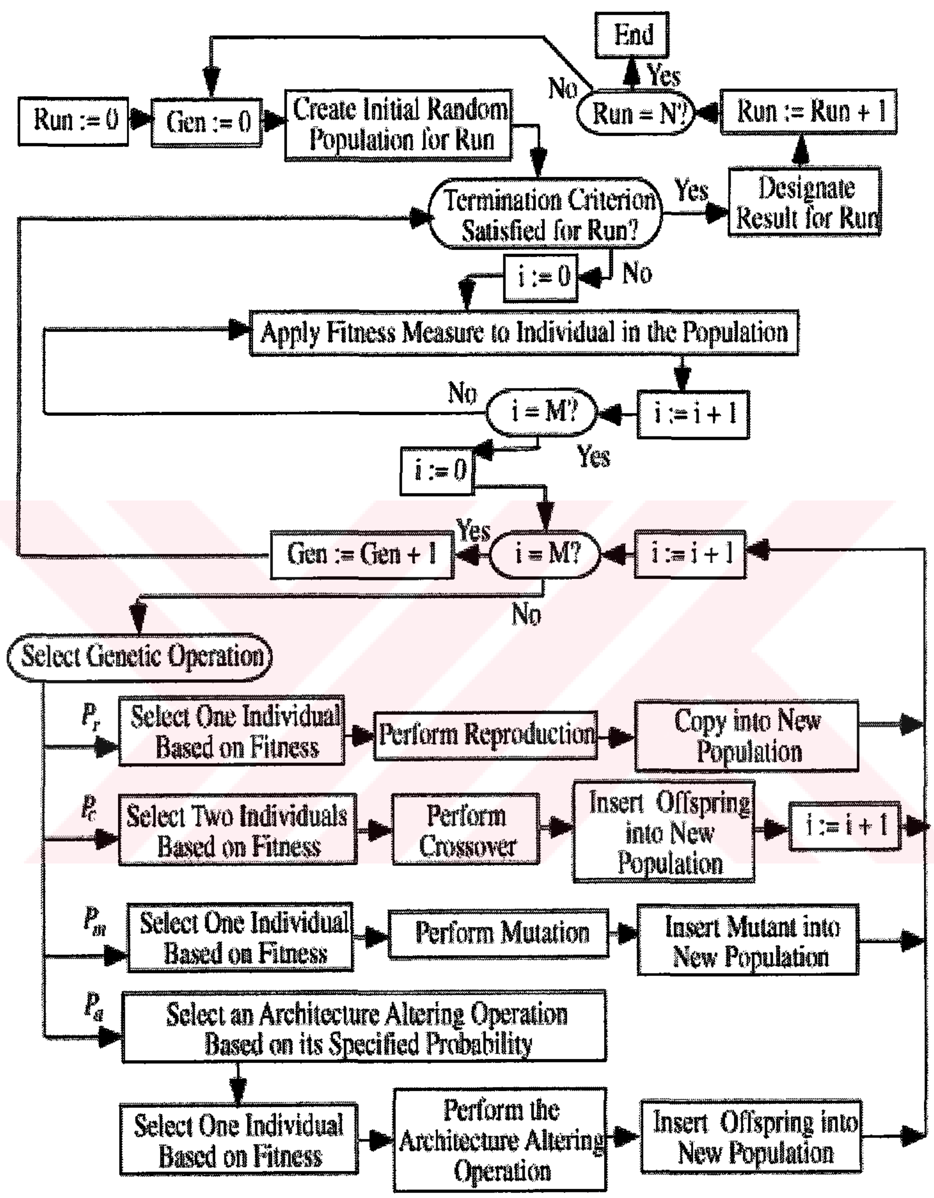

Figure 2.10: The GA flowchart [36]

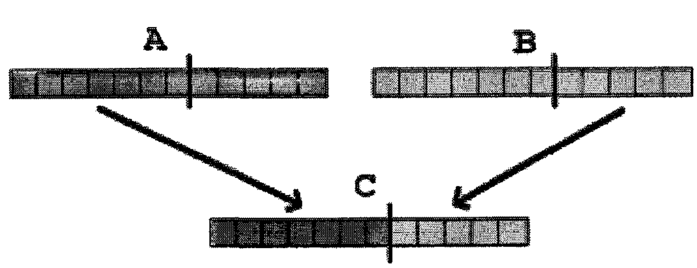

Figure 2.11: Crossover of the chromosemes in the GA

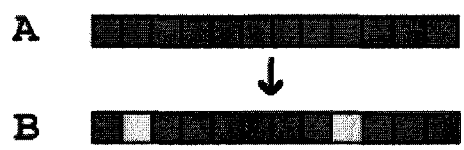

Figure 2.12: Mutation of the chromosomes in the GA

3. After the termination criterion is satisfied, the single best program in the population produced during the run (the best-so-far individual) is harvested and designated as the result of the run. If the run is successful, the result may be a solution (or approximate solution) to the problem.

2.4.2. The Memetic Algorithm

Up to now, several different implementations of the genetic algorithm have been used; concerning both the coding of the unknowns and the genetic operators. Actually, one of the main features of the the genetic algorithm is the possibility of using specific implementations. In this study also a new version of an evolutionary algorithm, called memetic algorithm is utilized [5]. The Memetic Algorithm, during the iterative evolution, considers only local minima of the cost function, so that a great speed-up is introduced in the search process.

2.4.2.1. Memetic Algorithm Overview

Memetic algorithms are optimization methods that belong to the family of evolutionary methods. In particular, they can be thought as hybrid genetic algorithms which are explained in the previous sections. The basic idea of the memetic algorithm is to enhance the typical Genetic Algorithm with well-known optimizatiom methods.

To this end, the new approach is based on the concept of meme [5]. A meme is a unit of information that can be transmitted when people exchange ideas. Memetic algorithms are population-based algorithms, in which every "idea" is an individual. Since people process any idea to obtain a personal optimum before propagating it, each individual is a point of local minima of the cost function.

The evolution of the population is modeled by using the same operators of the genetic algorithm, i.e., selection, crossover and mutation. Since these operators are not generally able to produce local optima, a local optimization procedure is needed.

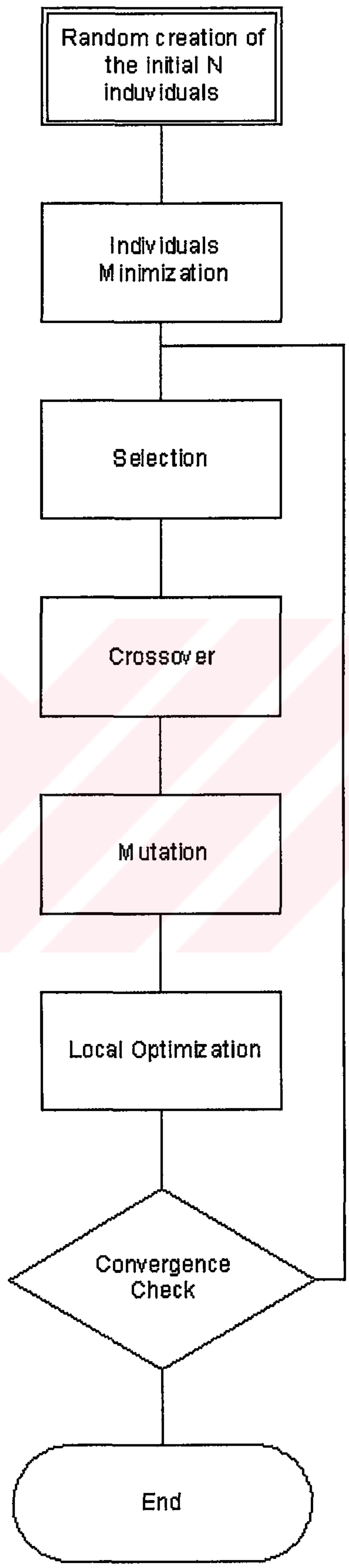

Figure 2.13: Memetic algorithm flowchart [5]

The general schema of a memetic algorithm is shown in Fig. 2.13. Let us consider a generic individual denoted by x_k

$$x_k = \left(x_k^1, \ldots x_k^m\right) \tag{2.2}$$

where x_k^i belongs to $\Re$ (real number set). The population of the algorithm is composed by N individuals:

$$P_i = \{x_k : k = 1, \ldots, N\} \tag{2.3}$$

where the subscript "i" indicates the generation's number. An initial population P_0 is generated by randomly choosing N arrays in the search domain. Generally, these arrays are not points corresponding to local minima of the cost function; consequently, a local optimization procedure is applied to every vector x_k in order to obtain a point of minimum x_k. Such a procedure is denoted by $O(x_k)$ and is defined as

$$O : \Re^m \ni x_k \longrightarrow x_k^* \in \Re^m \tag{2.4}$$

where $\Re^m$ is the search space. The new individuals, x_k^*, $k = 1, \ldots, N$ generated by the optimization process, represent the new initial population P_0^* of the algorithm [5]. The algorithm core is composed by three operations, i.e., selection, reproduction and mutation, which are applied sequentially. These operations are the same with the Genetic Algorithm.

Since the population is composed by only local minima, the individuals evolve over the search domain by "jumping" from a minimum to another one and a great speed up in the optimization procedure is obtained. Moreover, since the population is only composed by local minima, a reduced number of elements can be considered (e.g., equal to the number of unknown), with a significant computational saving.

3. THE PLATFORM AND SUBSYSTEMS

In this section the selected platform will be explained and the possible sources of EMI will be investigated.

3.1. The Platform

The platform chosen for research is the F-4 Phantom fighter-aircraft (Figure 3.1). F-4 Phantom is a multi-role fighter aircraft. It can fly day or night regardless of the weather. The Phantom is the backbone of the Turkish Air Force. Although it was designed more than 30 years ago, the design was refined by many updates up to now. Almost half of the fighter aircraft in the Turkish Air Force constitute of the Phantoms. Nowadays the modernization of the Phantom's engines, radar and avionics is under way and the aircraft is being planned to be used for a few decades.

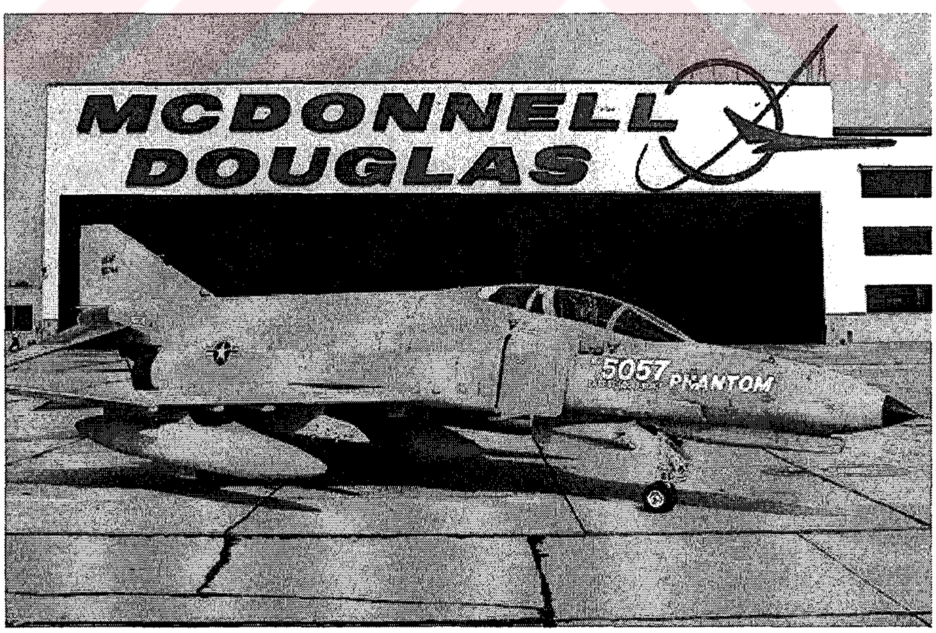

Figure 3.1: The phantom was built in USA in the 1970's [32].

The Phantom may carry huge variety of weapons exceeding 12 tons. (Figure 3.2).

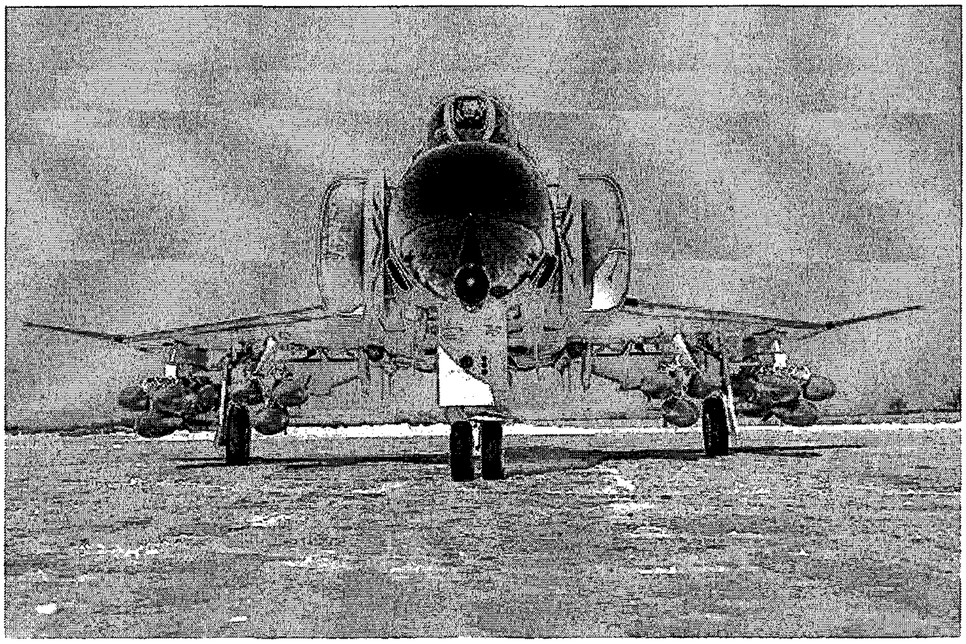

Figure 3.2: The Phantom loaded with free-fall bombs [32].

The dimensions of the Phantom are given in Table 3.1 [33].

Table 3.1 Dimensions of the F-4 Phantom

Length	18.75 m
Wingspan	12.04 m
Height	3.1 m

The dimensions in Table 3.1 are shown in Figure 3.3 and Figure 3.4 [33].

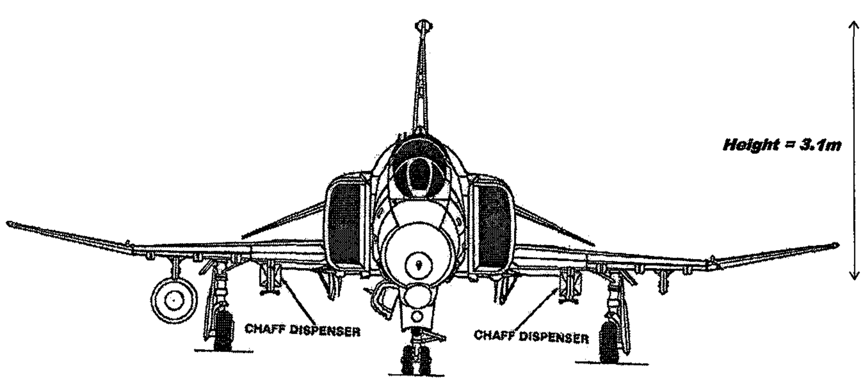

Figure 3.3: Scene of the F-4 Phantom from the front

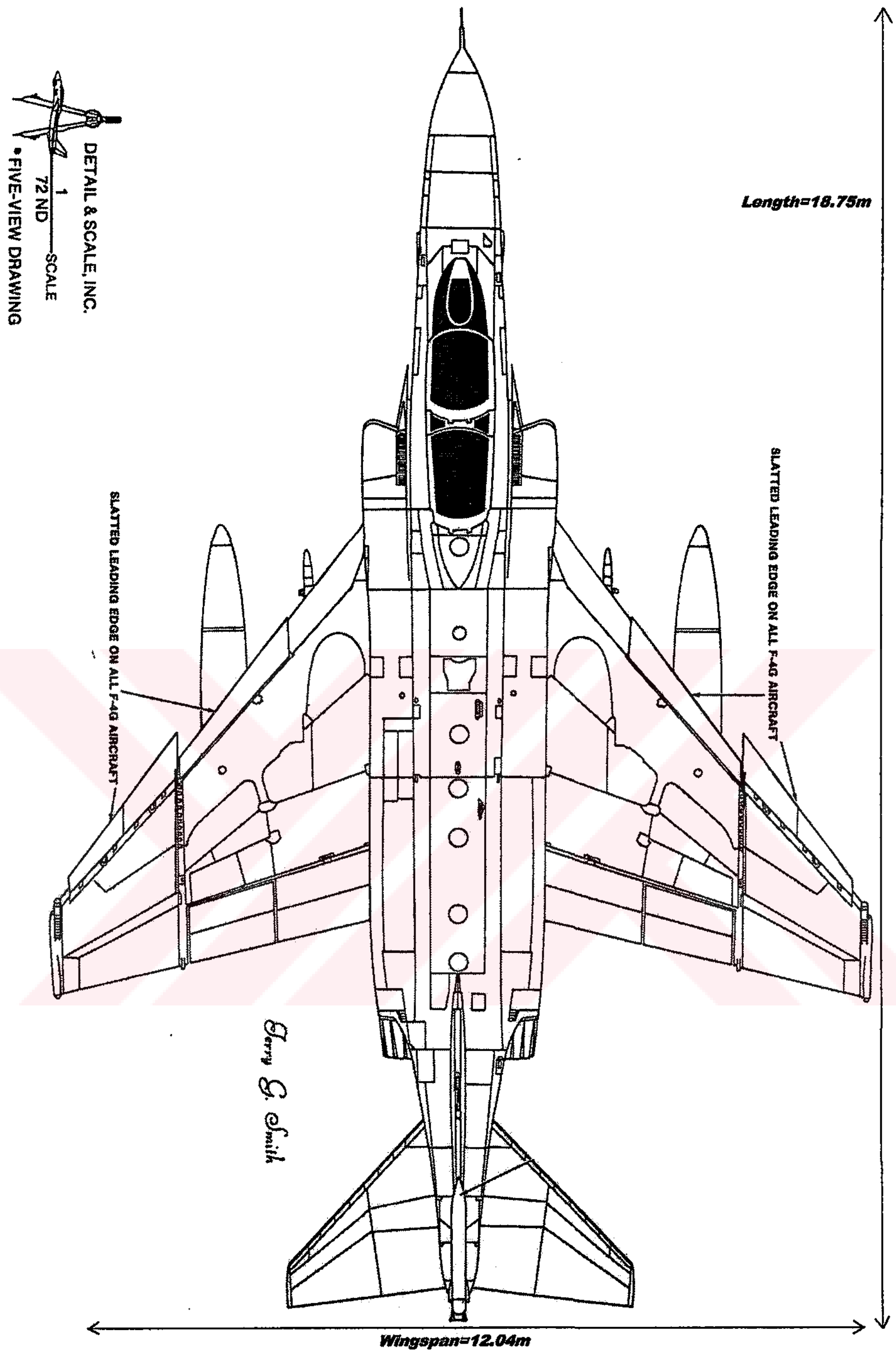

Figure 3.4: Scene of the F-4 Phantom from the top [33]

3.2. The Source of EMI Sub-System

In this study it is assumed that, during the modernization process the standart ARC 186/164 VHF/UHF voice communication transreceivers are being planned to be replaced by ASELSAN MXF-483/484 state-of-the-art transreceivers. This system is designed and produced by ASELSAN in Ankara/TURKEY with many superior features (Figure 3.5). The system consists of two seperate transreceivers and a pair of seperate antennas.

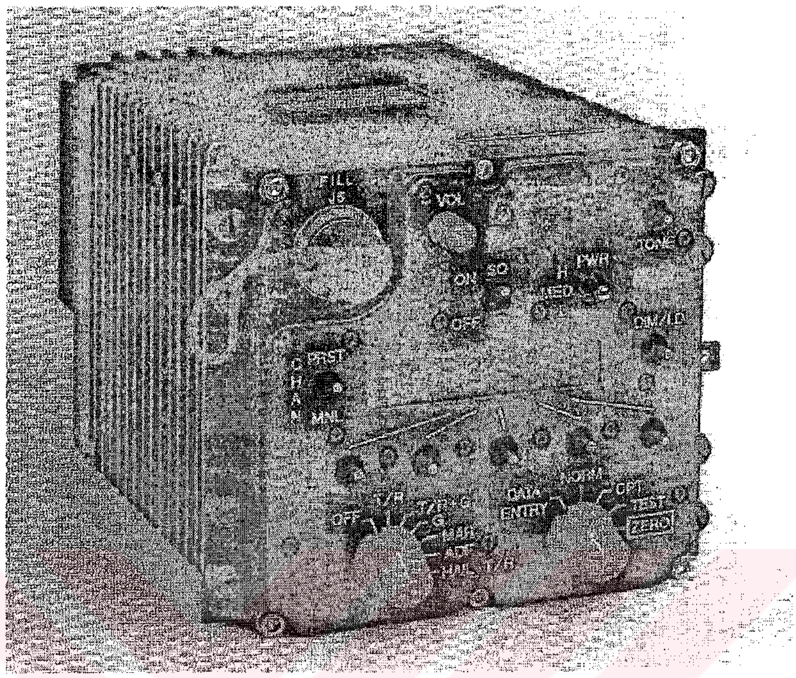

Figure 3.5: ASELSAN MXF-483/484 integrated transreceiver

During operation, the transmitters emit high levels of radiation. In the next chapter where the numerical analysis is held, we have seen that this level may exceed the EMI limit levels [34] (Figure 3.6). However, further techial information about the allowed levels of EMI is confidental and inacessible, even accessed, this information is prohobited for use in this academic study.

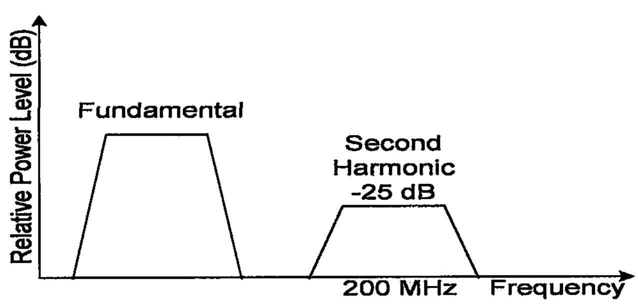

Figure 3.6: EMI limit levels for the VHF-UHF antennas

Considering the simple nature of the VHF-UHF communication via the Frequency Modulation (FM), the antenna pairs are modelled as $\lambda/4$ (quarter wavelength) monopole antennas.

3.3. The Other Sub-Systems

In the Phantom there are a variety of EM propagating sub-systems. These systems are listed in Table 3.2.

Table 3.2: EM Propagating Sub-Systems on the Phantom

ANTENNA		**RECEIVER/ TRANSMITTER**	**FREQUENCY RANGE (MHz)**
SYSTEM	**TYPE**		
RADAR	PLANAR/ ARRAY	R/T	8700-9400
IFF	OMNI	R/T	1030/1090
DME	OMNI	R/T	962-1213
RADIO ALTIMETER	HORN	R/T	4250/4350
GPS	OMNI	R	1575
RWR	SPIRAL	R	2000-18000

The sub-systems listed on Table 3.2 have navigational, defence and attack related purposes. The system abbrevations can be listed as:

- RADAR : Radio Detection and Ranging (Missile Homing)
- IFF : Identification of Friend or Foe (Defensive)
- DME : Distance Measuring Equipment (Navigational)
- GPS : Global Position System (Navigational) and
- RWR : Radar Warning Receiver (Defensive)

All these sub-systems are already electromagnetically compatible with the VHF/UHF antennas. The study will focus on the EMI problems between the mentioned VHF-UHF communication antennas. The suitable positions and orientations for the antennas where the coupling is minimum will be investigated.

4. THE NUMERICAL ANALYSIS

4.1. Application of System Equations to EMC Analysis

In order to determine whether an EMI problem exists between a potentially interfering transmitter and a receiver, it is necessary to consider the susceptibility of the receiver to both the design and spurious outputs (individually and collectively) of the potentially interfering transmitters. The factors that must be included in the analysis for each transmitter output (or group of transmitter outputs) include [15]:

- The transmitter power (P_T),
- The transmitting antenna gain in the direction of the receiver (G_T),
- The propagation loss between the transmitter and receiver (L),
- The receiver antenna gain in the direction of the transmitter (G_R) and
- The amount of power required to produce interference in the receiver (P_R) in the presence of the desired signal.

Factors that must be considered in EMC analysis include both the design (intentional) and operational performance characteristics of equipment and the nondesign (unintentional) and nonoperational characteristics. The necessity of considering parameters such as transmitter spurious output emissions, receiver spurious responses, antenna side-and-back lobe radiation and unintentional propagation paths introduces complications since it is now necessary to obtain information on equipment nondesign characteristics.

The procedure that is used for each transmitter output emission can be demonstrated by considering the interference situation that exists between a particular output of one of a number of potentially interfering transmitters and a particular receiver. In the case of a particular transmitter output (which may be either a fundamental or a spurious emission), the power available at the receiver is given by [15]:

$$P_A(f,t,d,p) = P_T(f,t) + C_{TR}(f,t,d,p) \tag{4.1}$$

where,

- $P_T(f,t)$ = transmitter power (in dBm) and
- $C_{TR}(f,t,d,p)$ = transmission coupling between the transmitter and receiver (in dB).
- $P_A(f,t,d,p)$ = the power available at the receiver (in dBm) which is a function of frequency (f), time (t), distance separation (d) and direction (p) of both transmitter and receiver and their antennas,

The requirement for EMC is that the power available at the receiver be less than the power required to produce interference in the receiver. Thus, the condition for electromagnetic compatibility is:

$$P_A(f,t,d,p) < P_R(f,t) \tag{4.2}$$

On the other hand, if the power available at the receiver input terminals is equal to or greater than the power required to produce interference in the receiver ($P_R(f,t)$), as given below, an electromagnetic interference problem may exist:

$$P_A(f,t,d,p) \geq P_R(f,t) \tag{4.3}$$

While the foregoing may seem basic, it is the essence of all intersystem EMI situations. The P_R term appearing in (4.2) is rather complicated. First, P_R in reality is greater than the receiver internal noise referred to the input and is related to the intended signal reception level. Secondly, to determine if interference is actually disturbing or damaging, calculations must be made to compare with a particular signal-to-interference (S/I) ratio and the impact that this will have on system performance.

4.1.1. Electric Field Integral Equation for MoM

This section can be described as a summary of the MoM Technical Reference Manual [43]. The form of the Electric Field Integral Equation (EFIE)used in NEC follows from an integral representation for the electric field of a volume current distribution $\mathbf{J}$.

$$\mathbf{E}(\mathbf{r}) = \frac{-j\eta}{4\pi k} \int_V \mathbf{J}(\mathbf{r}').\overline{\overline{G}}(\mathbf{r},\mathbf{r}')dV' \tag{4.4}$$

where,

$\overline{\overline{G}}(\mathbf{r}, \mathbf{r}') = (k^2\bar{I} + \nabla\nabla)\, g(\mathbf{r}, \mathbf{r}')$, $g(\mathbf{r}, \mathbf{r}') = e^{\frac{-jk|\mathbf{r} - \mathbf{r}'|}{|\mathbf{r} - \mathbf{r}'|}}$, $k = \omega\sqrt{\mu_0\varepsilon_0}$, $\eta = \sqrt{\frac{\mu_0}{\varepsilon_0}}$ and the time convention is $e^{j\omega t}$.

$\bar{I}$ is the identity dyad $(\hat{x}\hat{x} + \hat{y}\hat{y} + \hat{z}\hat{z})$. When the current distribution is limited to the surface of a perfectly conducting body, (4.4) becomes :

$$\mathbf{E}(\mathbf{r}) = \frac{-j\eta}{4\pi k}\int_s \mathbf{J}_s(\mathbf{r}').\overline{\overline{G}}(\mathbf{r},\mathbf{r}')dA' \tag{4.5}$$

where $\mathbf{J}_s$ is the surface current density.

The observation point $\mathbf{r}$ is restricted to be off the surface S so that $\mathbf{r} \neq \mathbf{r}'$. If $\mathbf{r}$ approaches S as a limit, (4.5) becomes :

$$\mathbf{E}(\mathbf{r}) = \frac{-j\eta}{4\pi k}\int_s \mathbf{J}_s(\mathbf{r}').\overline{\overline{G}}(\mathbf{r},\mathbf{r}')dA' \tag{4.6}$$

where the $\int_S$ now represents a principal value integral. It is a principle value integral since $g(\mathbf{r},\mathbf{r}')$ is now unbounded.

An integral equation for the current induced on S by an incident field $\mathbf{E}^I$ can be obtained from (4.6) and the boundary condition for $r \in S$:

$$\hat{n}(\mathbf{r}) \times \left[\mathbf{E}^s(\mathbf{r}) + \mathbf{E}^I(\mathbf{r})\right] = 0 \tag{4.7}$$

where , $\hat{n}(\mathbf{r})$ is the unit normal vector of the surface at $\mathbf{r}$ and $\mathbf{E}^s$ is the field due to the induced current $\mathbf{J}_S$.

Substituting (4.6) for $\mathbf{E}^s$ yields the integral equation :

$$-\hat{n}(\mathbf{r}) \times \mathbf{E}^I(\mathbf{r}) = \frac{-j\eta}{4\pi k}\hat{n}(\mathbf{r}) \times \int_S \mathbf{J}_s(\mathbf{r})(k^2\bar{I} + \nabla\nabla)g(\mathbf{r},\mathbf{r}')dA' \tag{4.8}$$

The vector integral in (4.8) can be reduced to a scalar integral equation when the conducting surface S is that of a cylindrical thin wire, thereby making the solution much easier. The assumptions applied for a thin wire, known as the thin-wire approximation, are as follows:

1. Transverse currents can be neglected relative to axial currents on the wire.

2. The circumferential variation in the axial current can be neglected.

3. The current can be represented by a filament on the wire axis.

4. The boundary condition on the electric field need be enforced in the axial direction only.

These widely used approximations are valid as long as the wire radius is much less than the wavelength and much less than the wire length. An alternate kernel for the EFIE, based on an extended thin-wire approximation in which condition 3 is relaxed, is also included in NEC for wires having too large a radius for the thin-wire approximation [35]. From assumptions 1, 2 and 3, the surface current $\mathbf{J}_S$ on a wire of radius can be replaced by a filamentary current I : $I(s)\hat{s} = 2\pi \mathbf{J}_s(\mathbf{r})$ where

s = distance parameter along the wire axis at $\mathbf{r}$

$\hat{s}$ = unit vector tangent to the wire axis at $\mathbf{r}$

Equation (4.8) then becomes

$$-\hat{n}(\mathbf{r}) \times \mathbf{E}^I(\mathbf{r}) = \frac{-j\eta}{4\pi k}\hat{n}(\mathbf{r}) \times \int_S \mathbf{I}(s')(k^2\hat{\mathrm{s}}' - \nabla\frac{\partial}{\partial s'})g(\mathbf{r},\mathbf{r}')ds' \tag{4.9}$$

where the integration is over the length of the wire. Enforcing the boundary condition in the axial direction reduces (4.9) to the scalar equation,

$$-\hat{s}.\mathbf{E}^I(\mathbf{r}) = \frac{-j\eta}{4\pi k}\int_S \mathbf{I}(s')(k^2\hat{\mathrm{s}}.\hat{\mathrm{s}}' - \frac{\partial^2}{\partial s \partial s'})g(\mathbf{r},\mathbf{r}')ds' \tag{4.10}$$

Since $\mathbf{r}'$ is now the point at s' on the wire axis while $\mathbf{r}$ is a point at s on the wire surface $|\mathbf{r} - \mathbf{r}'| \geq a$ and the integrand is bounded.

4.1.2. Numerical solution with MoM

The integral equation in (4.10) is solved numerically in NEC by a form of the method of moments. An excellent general introduction to the method of moments can be found in R.F. Harrington's book, "Field Computation by Moment Methods" [3]. A brief outline of the method follows.

The method of moments applies to a general linear-operator equation,

$$Lf = e \tag{4.11}$$

where f is an unknown response, e is a known excitation, and L is a linear operator (an integral operator in the present case). The unknown function f may be expanded in a sum of basis functions, f_j, as :

$$f = \sum_{j=1}^{N} \alpha_j f_j \tag{4.12}$$

A set of equations for the coefficients α_j are then obtained by taking the inner product of (4.12) with a set of weighting functions $\{w_i\}$

$$< w_i, Lf >=< w_i, e > \tag{4.13}$$

Due to the linearity of L, substituting (4.13) for f yields,

$$\sum_{j=1}^{N} \alpha_j < w_i, Lf_j >=< w_i, e > \tag{4.14}$$

This equation can be written in matrix notation as :

$$[G][A] = [E] \tag{4.15}$$

where

$$\begin{aligned} G_{ij} &=< w_i, Lf_j > \\ A_j &= \alpha_j \\ E_i &=< w_i, e > \end{aligned} \tag{4.16}$$

The solution is then

$$[A] = [G]^{-1}[E] \tag{4.17}$$

the solution of equation (4.10), the inner product is defined as:

$$< f, g >= \int_S f(\mathbf{r}) g(\mathbf{r}) dA' \tag{4.18}$$

The integration is over the structure surface. Various choices are possible for the weighting functions $\{w_i\}$ and basis functions $\{f_i\}$. When $w_i = f_i$, the procedure is known as Galerkin's method. In NEC the basis and weight functions are different, $\{w_i\}$ being chosen as a set of delta functions

$$w_i(\mathbf{r}) = \delta(\mathbf{r} - \mathbf{r}_i) \tag{4.19}$$

$\{\mathbf{r}_i\}$ a set of points on the conducting surface. The result is a point sampling of the integral equations known as the collocation method of solution. Wires are divided into short straight segments with a sample point at the centre of each segment.

The choice of basis functions is very important for an efficient and accurate solution. In NEC, the support of $\{f_i\}$ is restricted to a localised subsection of the surface near $\mathbf{r}_i$. This choice simplifies the evaluation of the inner-product integral and ensures that the matrix $[G]$ will be well conditioned. For finite N, the sum of $\{f_j\}$ cannot exactly equal a general current distribution so the functions $\{f_i\}$ should be chosen as close as possible to the actual current distribution. The basis functions used in NEC are explained in the following sections.

4.1.3. Current expansions on wires

Wires in NEC are modelled by short straight segments with the current on each segment represented by three terms - a constant, a sine, and a cosine. This expansion was first used by Yeh and Mei [44] and has been shown to provide rapid solution convergence. It has the added advantage that the fields of the sinusoidal currents are easily evaluated in closed form. The amplitude of the constant, sine, and cosine terms are related such that their sum satisfies physical conditions on the local behaviour of current and charge at the segment ends. This differs from cases where the current was extrapolated to the centres of the adjacent segments, resulting in discontinuities in current and charge at the segment ends. Matching at the segment ends improves the solution accuracy, especially at the multiple-wire junctions of unequal length segments where inother cases segment ends are extrapolated to an average length segment, often with inaccurate results. The total current on segment number j in NEC has the form :

$$I_j(s) = A_j + B_j \sin k(s - s_j) + C_j \cos k(s - s_j), \left|s - s_j\right| < \frac{\Delta_j}{2} \tag{4.20}$$

where s_j is the distance value at the centre of segment j and Δ_j is the length of segment j. Of the three unknown constants Aj, Bj and Cj two are eliminated by local conditions on the current leaving one constant, related to the current amplitude, to be determined by the matrix equation. The local conditions are applied to the current and to the linear charge density, q, which is related to the current by the equation of continuity :

$$\frac{\partial I}{\partial s} = -j\omega q \tag{4.21}$$

At a junction of two segments with uniform radius, the obvious boundary conditions are that the current and charge are continuous at the junction. At a junction of two or more segments with unequal radii, the continuity of current is generalised to Kirchoff's current law that the sum of currents into the junction is zero. The total charge in the vicinity of the junction is assumed to distribute itself on individual wires according to the wire radii. T.T. Wu and R.W.P. King [45] have derived a condition for the linear charge density on a wire at a junction that neglects local coupling effects. Using their derivation, $\frac{\partial I}{\partial s}$, can be determined by :

$$\left.\frac{\partial I(s)}{\partial s}\right|_{s \text{ at junction}} = \frac{Q}{\ln\left(\frac{2}{ka}\right) - 0.5772} \tag{4.22}$$

e a is the wire radius and k is the wave number. Q is related to the total charge in the vicinity of the junction and is constant for all wires at the junction.

At a free wire end, the current may be assumed to go to zero. On a wire of finite radius, however, the current can flow into the end cap and hence be nonzero at the wire end. In one study of this effect, a condition relating the current at the wire end to the current derivative was derived [45]. For a wire radius a, this condition is :

$$I(s)\big|_{s \text{ at end}} = \left.\frac{-(\hat{s}.\hat{n}_c)}{k}\frac{J_1(ka_j)}{J_0(ka_j)}\frac{\partial I(s)}{\partial(s)}\right|_{s \text{ at end}} \tag{4.23}$$

J_o and J_I are Bessel functions of order 0 and 1 respectively. The unit vector $\hat{n}_c$ is normal to the end cap. Hence, $\hat{s}.\hat{n}_c$ is +1 if the reference direction, $\hat{s}$ is toward the end, and -1 if $\hat{s}$ is away from the end. Thus, for each segment two equations are obtained from the two ends. At free ends the following holds :

$$I_j\left(s_j \pm \frac{\Delta_j}{2}\right) = \left.\frac{\pm 1}{k}\frac{J_1(ka_j)}{J_0(ka_j)}\frac{\partial I(s)}{\partial(s)}\right|_{s=s_j \pm \frac{\Delta_{j2}}{2}} \tag{4.24}$$

When the end of a segment connects to other segments, a second equation is obtained:

$$\left.\frac{\partial I_j(s)}{\partial s}\right|_{s_j \pm \frac{\Delta_j}{2}} = \frac{Q_j^{\pm}}{\ln\left(\frac{2}{ka}\right) - 0.5772} \tag{4.25}$$

Two additional unknowns Q_j^- and Q_j^+ are associated with the junctions but can be eliminated by Kirchoff's current equation at each junction. The boundary condition equations provide the additional equation-per-segment to completely determine the current function of equation (4.20) for every segment. To apply this condition, the current is expanded as a sum of selected basis functions so that they satisfy the local conditions on current and charge in any linear combination. A typical set of basis functions and their sum on a four-segment wire are shown in Figure 4.1. For a general segment I in Figure 4.2 the i^{th} basis function has a peak on segment i and extends onto every segment connected to i, going to zero with zero derivative at the outer ends of the connected segments.

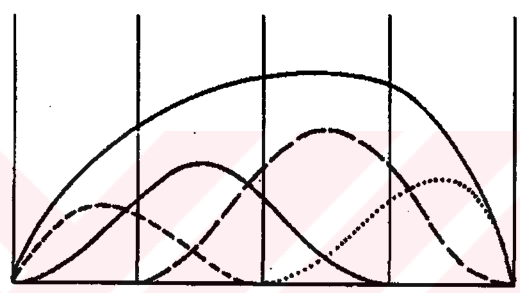

Figure 4.1: Current basis function and sim on a four segment wire.

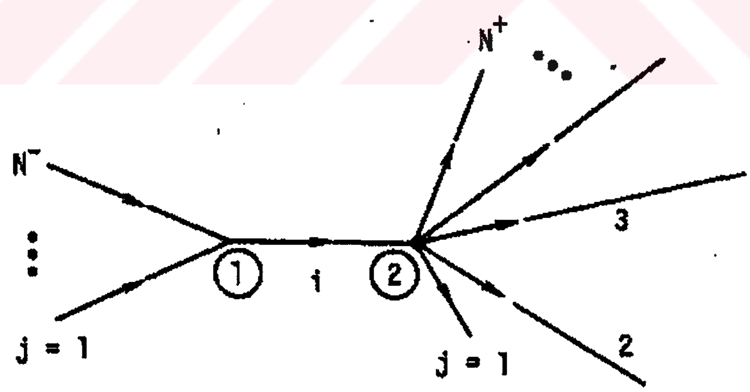

Figure 4.2: Segments covered by the i^{th} basis function.

The general definition of the i^{th} basis function is given below. For the junction and end conditions described above, the following definitions apply for the factors in the segment end conditions:

$$a_i^- = a_i^+ = \left[\ln\left(\frac{2}{ka_i}\right) - 0.5772 \right]^{-1} \tag{4.26}$$

and

$$X_i = \frac{J_1(ka_i)}{J_0(ka_i)} \tag{4.27}$$

The condition of zero current at a free end may be obtained by setting X_i to zero. The portion of the i^{th} basis function on segment i in Figure 4.1 is then :

$$f_i^0(s) = A_i^0 + B_i^0 \sin k(s-s_i) + C_i^0 \cos k(s-s_i), \left|s-s_i\right| < \frac{\Delta_i}{2} \tag{4.28}$$

If $N^- \neq 0$ and $N^+ \neq 0$ in Figure 4.2, the end conditions are :

$$\left.\frac{\partial}{\partial s} f_i^0(s)\right|_{s=s_i-\frac{\Delta_i}{2}} = a_i^- Q_i^- \tag{4.29}$$

$$\left.\frac{\partial}{\partial s} f_i^0(s)\right|_{s=s_i-\frac{\Delta_i}{2}} = a_i^+ Q_i^+ \tag{4.30}$$

If $N^- = 0$ and $N^+ \neq 0$, end conditions are :

$$f_i^0\left(s_i - \frac{\Delta_i}{2}\right) = \frac{1}{k} X_i \left.\frac{\partial}{\partial s} f_i^0(s)\right|_{s=s_i-\frac{\Delta_i}{2}} \tag{4.31}$$

$$\left.\frac{\partial}{\partial s} f_i^0(s)\right|_{s=s_i+\frac{\Delta_i}{2}} = a_i^+ Q_i^+ \tag{4.32}$$

If $N^- \neq 0$ and $N^+ = 0$, end conditions are :

$$f_i^0\left(s_i + \frac{\Delta_i}{2}\right) = \frac{-1}{k} X_i \left.\frac{\partial}{\partial s} f_i^0(s)\right|_{s=s_i+\frac{\Delta_i}{2}} \tag{4.33}$$

$$\left.\frac{\partial}{\partial s} f_i^0(s)\right|_{s=s_i-\frac{\Delta_i}{2}} = a_i^- Q_i^- \tag{4.34}$$

Over segments connected to end 1 of segment i, the i^{th} basis function is :

$$f_j^-(s) = A_j^- + B_j^- \sin k(s-s_j) + C_j^- \cos k(s-s_j),\ \left|s-s_j\right| < \frac{\Delta_j}{2},\ j = 1 \ldots N^- \tag{4.35}$$

End conditions are :

$$f_j^-\left(s_j - \frac{\Delta_j}{2}\right) = 0 \tag{4.36}$$

$$\frac{\partial}{\partial s} f_j^-(s)\bigg|_{s=s_j-\frac{\Delta_j}{2}} = 0 \tag{4.37}$$

$$\frac{\partial}{\partial s} f_j^-(s)\bigg|_{s=s_j+\frac{\Delta_j}{2}} = a_j^+ Q_i^- \tag{4.38}$$

Over segments connected to end 2 of segment i, the i^{th} basis function is :

$$f_j^+(s) = A_j^+ + B_j^+ \sin k(s-s_j) + C_j^+ \cos k(s-s_j), \ \left|s-s_j\right| < \frac{\Delta_j}{2}, \ j = 1 \ldots N^+ \tag{4.39}$$

End conditions are :

$$\frac{\partial}{\partial s} f_j^+(s)\bigg|_{s=s_j-\frac{\Delta_j}{2}} = a_j^- Q_i^+ \tag{4.40}$$

$$f_j^+\left(s_j - \frac{\Delta_j}{2}\right) = 0 \tag{4.41}$$

$$\frac{\partial}{\partial s} f_j^+(s)\bigg|_{s=s_j+\frac{\Delta_j}{2}} = 0 \tag{4.42}$$

Equations (4.35) and (4.39), defining the complete basis function, involve $3(N^- + N^+ + 1)$ unknown constants. Of these, $3(N^- + N^+) + 2$ unknowns are eliminated by the end conditions in terms of Q_i^- and Q_i^+ which can then be determined from the two Kirchoff's current equations:

$$\sum_{j=1}^{N^-} f_j^-\left(s_j + \frac{\Delta_j}{2}\right) = f_i^0\left(s_i - \frac{\Delta_i}{2}\right) \tag{4.43}$$

$$\sum_{j=1}^{N^+} f_j^+\left(s_j + \frac{\Delta_j}{2}\right) = f_i^0\left(s_i - \frac{\Delta_i}{2}\right) \tag{4.44}$$

The complete basis function is then defined in terms of one unknown constant. In this case A_i^0 was set to -1 since the function amplitude is arbitrary, being determined by the boundary condition equations. The final result is given below:

$$A_j^- = \frac{a_j^+ Q_i^-}{\sin k\Delta_j} \tag{4.45}$$

$$B_j^- = \frac{a_j^+ Q_i^-}{2\cos k\frac{\Delta_j}{2}} \tag{4.46}$$

$$C_j^- = \frac{-a_j^+ Q_i^-}{2\sin k\frac{\Delta_j}{2}} \tag{4.47}$$

$$A_j^+ = \frac{-a_j^- Q_i^+}{\sin k\Delta_j} \tag{4.48}$$

$$B_j^+ = \frac{a_j^- Q_i^+}{2\cos k\frac{\Delta_j}{2}} \tag{4.49}$$

$$C_j^+ = \frac{a_j^- Q_i^+}{2\sin k\frac{\Delta_j}{2}} \tag{4.50}$$

For $N^- \neq 0$ and $N^+ \neq 0$:

$$A_i^0 = -1 \tag{4.51}$$

$$B_i^0 = (a_i^- Q_i^- + a_i^+ Q_i^+)\frac{\sin\frac{k\Delta_i}{2}}{\sin k\Delta_i} \tag{4.52}$$

$$C_i^0 = (a_i^- Q_i^- - a_i^+ Q_i^+)\frac{\cos\frac{k\Delta_i}{2}}{\sin k\Delta_i} \tag{4.53}$$

$$Q_i^- = \frac{a_i^+(1-\cos k\Delta_i) - P_i^+ \sin k\Delta_i}{(P_i^- P_i^+ + a_i^- a_i^+)\sin k\Delta_i + (P_i^- P_i^+ - P_i^+ a_i^-)\cos k\Delta_i} \tag{4.54}$$

$$Q_i^+ = \frac{a_i^-(\cos k\Delta_i - 1) - P_i^- \sin k\Delta_i}{(P_i^- P_i^+ + a_i^- a_i^+)\sin k\Delta_i + (P_i^- P_i^+ - P_i^+ a_i^-)\cos k\Delta_i} \tag{4.55}$$

For $N^- = 0$ and $N^+ \neq 0$:

$$A_i^0 = -1 \tag{4.56}$$

$$B_i^0 = +a_i^+ Q_i^+ \frac{\cos\frac{k\Delta_i}{2} - X_i \sin\frac{k\Delta_i}{2}}{\cos k\Delta_i - X_i \sin k\Delta_i} \tag{4.57}$$

$$C_i^0 = \frac{\cos\frac{k\Delta_i}{2}}{\cos k\Delta_i - X_i \sin k\Delta_i} + a_i^+ Q_i^+ \frac{\sin\frac{k\Delta_i}{2} - X_i \cos\frac{k\Delta_i}{2}}{\cos k\Delta i - X_i \sin k\Delta_i} \tag{4.58}$$

$$Q_i^+ = \frac{\cos k\Delta_i - 1 - X_i \sin k\Delta_i}{(a_i^+ + X_i P_i^+)\sin k\Delta_i + (a_i^+ X_i - P_i^+)\cos k\Delta_i} \tag{4.59}$$

For $N^- \neq 0$ and $N^+ = 0$:

$$A_i^0 = -1 \tag{4.60}$$

$$B_i^0 = \frac{-\sin\frac{k\Delta_i}{2}}{\cos k\Delta_i - X_i \sin k\Delta_i} + a_i^- Q_i^- \frac{\cos\frac{k\Delta_i}{2} - X_i \sin\frac{k\Delta_i}{2}}{\cos k\Delta_i - X_i \sin k\Delta_i} \tag{4.61}$$

$$C_i^0 = \frac{\cos\frac{k\Delta_i}{2}}{\cos k\Delta_i - X_i \sin k\Delta_i} - a_i^- Q_i^- \frac{\sin\frac{k\Delta_i}{2} - X_i \cos\frac{k\Delta_i}{2}}{\cos k\Delta_i - X_i \sin k\Delta_i} \tag{4.62}$$

$$Q_i^+ = \frac{1 \quad - \cos k\Delta_i + X_i \sin k\Delta_i}{(a_i^- + X_i P_i^-)\sin k\Delta_i + (P_i^- + a_i^- X_i)\cos k\Delta_i} \tag{4.63}$$

For all cases:

$$P_i^- = \sum_{j=1}^{N^-}\left(\frac{1-\cos k\Delta_i}{\sin k\Delta_j}\right) a_j^+ \tag{4.64}$$

$$P_i^+ = \sum_{j=1}^{N^+}\left(\frac{\cos k\Delta_j - 1}{\sin k\Delta_j}\right) a_j^- \tag{4.65}$$

where the sum of P_i^- is over segments connected to end 1 of segment i, and the sum for P_i^+ is over segments connected to end 2. If $N^- = N^+ = 0$ the complete basis function is :

$$f_i^0 = \frac{\cos k(s - s_i)}{\cos k\frac{\Delta_i}{2} - X_i \sin\frac{\Delta_i}{2}} - 1 \tag{4.66}$$

It should be noted that the basis function f_i has unit value at the centre of segment i and zero value at the centres of connected segments although it does extend onto the connected segments. As a result, the amplitude of f_i is the total current at the centre of segment i must be computed by summing the contributions of all basis functions extending onto segment i.

4.1.4. The matrix equation for current

For a structure having N_S wire segments, the order of the matrix in equation (4.15) is N_S. The matrix equation has the form :

$$[G][I]=[E] \tag{4.67}$$

I is then the column vector of segment basis function amplitudes. The elements of E are the left-hand side of equation (4.10) evaluated at the segment centres. A matrix element G_{ij} in matrix G represents the electric field at the centre of segment i due to the jth segment basis function, centred on segment j. The matrix equation in (4.67) is solved in NEC by Gauss elimination [43]. The basic step is factorisation of the matrix G into the product of an upper triangular matrix U and a lower triangle matrix G where

$$G=[L][U] \tag{4.68}$$

The matrix equation is then

$$[L][U][I]=[E] \tag{4.69}$$

from which the solution, I, is computed in two steps as

$$[L][F]=[E] \tag{4.70}$$

and

$$[U][I]=[F] \tag{4.71}$$

Equation (4.70) is first solved for F by forward substitution, and equation (4.71) is then solved for I by backward substitution. The major computational effort is factoring G into L and U. This takes approximately $\frac{1}{3}N^3$ multiplication steps for a matrix of order N compared to N^3 for inversion of G by the Gauss-Jordan method. Solution of equations (4.70) and (4.71), making use of the triangular properties of L and U, takes approximately as many multiplications as would be required for multiplication of G^{-1} by the column vector E. The factored matrices L and U are saved in NEC since the solution for induced current may be repeated for a number of different excitations. This, then, requires only the repeated solution of equations (4.70) and (4.71).

Computation of the elements of the matrix G and solution of the matrix equation are the two most time-consuming steps in computing the response of a structure, often accounting for over 90% of the computation time. This may be reduced substantially by making use of symmetries of the structure, either symmetry about a plane, or symmetry under rotation.

In rotational symmetry, a structure having M sectors is unchanged when rotated by any multiple of *360/M* degrees. If the equations for all segments in the first sector are numbered first and followed by successive sectors in the same order, the matrix equation can be expanded in submatrices in the form :

$$\begin{bmatrix} A_1 & A_2 & A_3 & & A_{M-1} & A_M \\ A_M & A_1 & A_2 & & A_{M-2} & A_{M-1} \\ A_{M-1} & A_M & A_1 & & A_{M-3} & A_{M-2} \\ & & & & & \\ & & & & & \\ A_2 & A_3 & A_4 & & A_M & A_1 \end{bmatrix} \begin{bmatrix} I_1 \\ I_2 \\ I_3 \\ \\ \\ I_M \end{bmatrix} = \begin{bmatrix} E_1 \\ E_2 \\ E_3 \\ \\ \\ E_M \end{bmatrix} \tag{4.72}$$

If there are N_c equations in each sector, E_i and I_i are N_c element column vectors of the excitations and currents in sector *i*. A_i is a submatrix of order N_c containing the interaction fields in sector 1 due to currents in sector *i*. Due to symmetry, this is the same as the fields in sector *k* due to currents in sector $i+k$, resulting in the repetition pattern shown. Thus, only matrix elements in the first row of submatrices need be computed, reducing the time to fill the matrix by a factor of *1/M.*

The time to solve the matrix equation can also be reduced by expanding the excitation sub-vectors in a discrete Fourier series as :

$$E_i = \sum_{k=1}^{M} S_{ik} E_k, \quad i = 1 \ldots M \tag{4.73}$$

where

$$S_{ik} = e^{\frac{j2\pi(i-1)(k-1)}{M}} \tag{4.74}$$

Examining a component in the expansion,

$$E = \begin{bmatrix} S_{1k}E_k \\ S_{2k}E_k \\ \\ \\ S_{Mk}E_k \end{bmatrix} \tag{4.75}$$

it is seen that the excitation differs from sector to sector only by a uniform phase shift. This excitation of a rotationally symmetric structure results in a solution having the same form as the excitation, i.e.,

$$I = \begin{bmatrix} S_{1k}I_k \\ S_{2k}I_k \\ \\ \\ S_{Mk}I_k \end{bmatrix} \tag{4.76}$$

It can be shown that this relation between solution and excitation holds for any matrix having the form of that in equation (4.72) Substituting these components of E and I into equation (4.72) yields the following matrix equation of order N_c relating I_k to E_k:

$$\left[S_{1k}A_1 + S_{2k}A_2 + \ldots + S_{Mk}A_M\right]\left[I_k\right] = S_{1k}\left[E_k\right] \tag{4.77}$$

The solution for the total excitation is then obtained by an inverse transformation,

$$I_i = \sum_{k=1}^{M} S_{ik}I_k, \quad i = 1\ldots M \tag{4.78}$$

The solution procedure, then, is first to compute the M submatrices A_i and Fourier-transform of these to obtain

$$A_i = \sum_{k=1}^{M} S_{ik}A_k, \quad i = 1\ldots M \tag{4.79}$$

The matrices Ai of order Nc are then each factored into upper and lower triangular matrices by the Gauss elimination method. For each excitation vector, the transformed sub-vectors are then computed by equation (4.73),

$$\left[A_i\right]\left[I_i\right] = \left[E_i\right] \tag{4.80}$$

The total solution is then given by (4.80). NEC includes a provision to generate and factor an interaction matrix and save the result of a file. A later run, using the file, may add to the structure and solve the complete model without unnecessary repetition of calculations. This procedure is called the Numerical Green's Function option since the effect is as if the free space Green's function in NEC were replaced by the Green's function for the structure on the file. The NGF is particularly useful for a large structure, such as a ship, on which various antennas will be added or modified. It also permits taking advantage of partial symmetry since a NGF file may be written for the symmetric part of a structure, taking advantage of the symmetry to reduce computation time. Unsymmetric parts can be added in a later run.

For the NGF solution the matrix is partitioned as

$$\begin{bmatrix} A & B \\ C & D \end{bmatrix} \begin{bmatrix} I_1 \\ I_2 \end{bmatrix} = \begin{bmatrix} E_1 \\ E_2 \end{bmatrix} \tag{4.81}$$

where A is the interaction matrix for the initial structure, D is the matrix for the added structure, and B and C represent mutual interactions. The currents are computed as

$$I_2 = \left[D - CA^{-1}B\right]^{-1}\left[E_2 - CA^{-1}E_1\right] \tag{4.82}$$

$$I_1 = A^{-1}E_1 - A^{-1}BI_2 \tag{4.83}$$

after the factored matrix A has been read from the file along with other necessary data.

Electrical connections between the new structure and the old structure require special treatment. If a new wire connects to an old wire the current basis function for the old wire segment is changed by the modified condition at the junction. The old basis function is given zero amplitude by adding a new equation having all zeros except for a one in the column of the old basis function. A new column is added for the corrected basis function.

4.1.5. Calculation of antenna to antenna coupling

In this study, coupling between antennas is the parameter of interest, in case when a receiving system must be protected from a nearby transmitter. Maximum power transfer between antennas occurs when the source impedance and receiver load impedance are conjugate-matched to their antennas. Determination of this condition is complicated by the antenna interaction, however, since the input impedance of one antenna depends on the load connected to the other antenna. it is conceivable that one can obtain highly accurate predictions of antenna-to-antenna coupling within the accuracy of the models.

The most popular approximate technique is to use the Friis transmission equation modified to account for (in an approximate sense) the shading and diffraction imposed by the physical shape of the system structure [47]. The Friis transmission equation gives the ratio of the power received at an antenna, P_r to the power transmitted by another antenna, P_t in terms of the antenna gains, G_r and G_t the separation distance between the two, d, and the wavelength, λ, at the frequency of transmission:

$$C = 10\log\frac{P_r}{P_t} = 10\log\left[G_r G_t\left(\frac{\lambda}{4\pi d}\right)^2\right] \tag{4.84}$$

where, C is the coupling between antennas. This model is strictly valid only for the two antennas in the far field of each other, matched polarization and matched termination impedances. Many experimental tests have indicated prediction accuracies on aircraft of within typically 6 dB [15]. Equation (4.84) is modified by terms which account for shading or diffraction. Although the Friis transmission equation modified by shading and diffraction factors forms the heart of many antenna-to-antenna coupling codes, there exist much more accurate prediction models. The MoM, which is from most popular of these, is also the selected method for this study [3]. In the Numerical Electromagnetics Code (NEC), the isolation value between antennas are calculated from the admittance parameters of the antenna feed segments. Two antennas between which coupling is investigated may be considered as a two-port network (Figure 4.3).

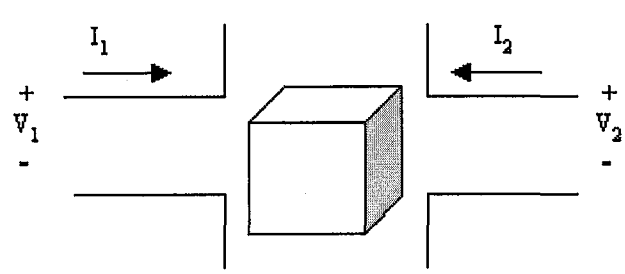

Figure 4.3: Representation of two antennas as a two-port network

The Y-matrix can be represented as:

$$\begin{bmatrix} I_1 \\ I_2 \end{bmatrix} = \begin{bmatrix} Y_{11} & Y_{12} \\ Y_{21} & Y_{22} \end{bmatrix} \begin{bmatrix} V_1 \\ V_2 \end{bmatrix} \tag{4.85}$$

where,

$$Y_{11} = \left. \frac{I_1}{V_1} \right|_{V_2=0} \tag{4.86}$$

$$Y_{12} = \left. \frac{I_1}{V_2} \right|_{V_1=0} \tag{4.87}$$

$$Y_{21} = \left. \frac{I_2}{V_1} \right|_{V_2=0} \quad \text{and,} \tag{4.88}$$

$$Y_{22} = \left. \frac{I_2}{V_2} \right|_{V_1=0} \tag{4.89}$$

The coupling problem can be solved in closed form by the Linville Method [48], a technique used in RF amplifier design. The first step is to determine the two-port admittance parameters for the coupled antennas by exciting each antenna with the other short-circuited and computing the self and mutual admittance from the currents computed by NEC. The maximum coupling is then :

$$C_{\max} = \frac{1}{L}\left[1 - \sqrt{1 - L^2}\right] \tag{4.90}$$

where,

$$L = \frac{\left[Y_{12} Y_{21}\right]}{2\,\mathrm{Re}\left[Y_{11}\right].\mathrm{Re}\left[Y_{22}\right] - \mathrm{Re}\left[Y_{12} Y_{21}\right]} \tag{4.91}$$

4.2. Analysis Output

Following quantities are obtained after the analysis:

- Maximum coupling between the two antennas (C_{max}),
- The input impedance of the source antenna (Z_{in}),
- The load impedance of the receiver antenna (Z_L).

With these quantities, the input and output reflection coefficients (S_{11} and S_{22}) of the same circuit are calculated as:

$$S_{11} = \frac{\dfrac{1}{Y_{IN}} - Z_0}{\dfrac{1}{Y_{IN}} + Z_0} \tag{4.92}$$

The input admittance of the first antenna is:

$$Y_{IN} = Y_{11} - \frac{Y_{21}Y_{12}}{Y_L + Y_{22}} \tag{4.93}$$

$$S_{22} = \frac{\dfrac{1}{Y_L^*} - Z_0}{\dfrac{1}{Y_L^*} + Z_0} \tag{4.94}$$

where,

$$Y_L = \left[\frac{1-\rho}{1+\rho} + 1\right]\mathrm{Re}\left[Y_{22}\right] - Y_{22} \tag{4.95}$$

$$\rho = \frac{C_{\max}\left(Y_{12}Y_{21}\right)^*}{\left|Y_{12}Y_{21}\right|} \tag{4.96}$$

where Z_0 stands for the characteristic impedance of the system that is 50 Ohms. These calculated parameters will later be used for comparison of the analysis and measurement results.

4.2.1. Selection of the analysis method

The ratio of the investigated UHF/VHF wavelength to the dimensions of the aircraft are within the acceptable range of both the MoM and the UTD metgods. For selecting the most appropriate method a trial is done on a cylinder representing the body of the aircraft. Two monopole antennas are placed on the center of the cylinder in opposite directions and the coupling is calculated. The parameters for the trial computation are given in Table 4.1 From the results in Figure 4.4, it is seen that there is a decade of difference between the two methods. The result for the MoM calculation can be considered 'exact' as long as the segmentation rules given in the next section are applied.

Table 4.1: Parameters for the aircraft-like structure

Unit	Value
Cylinder radius (m)	1.2
Cylinder length (m)	5
Antenna length (m)	1.071

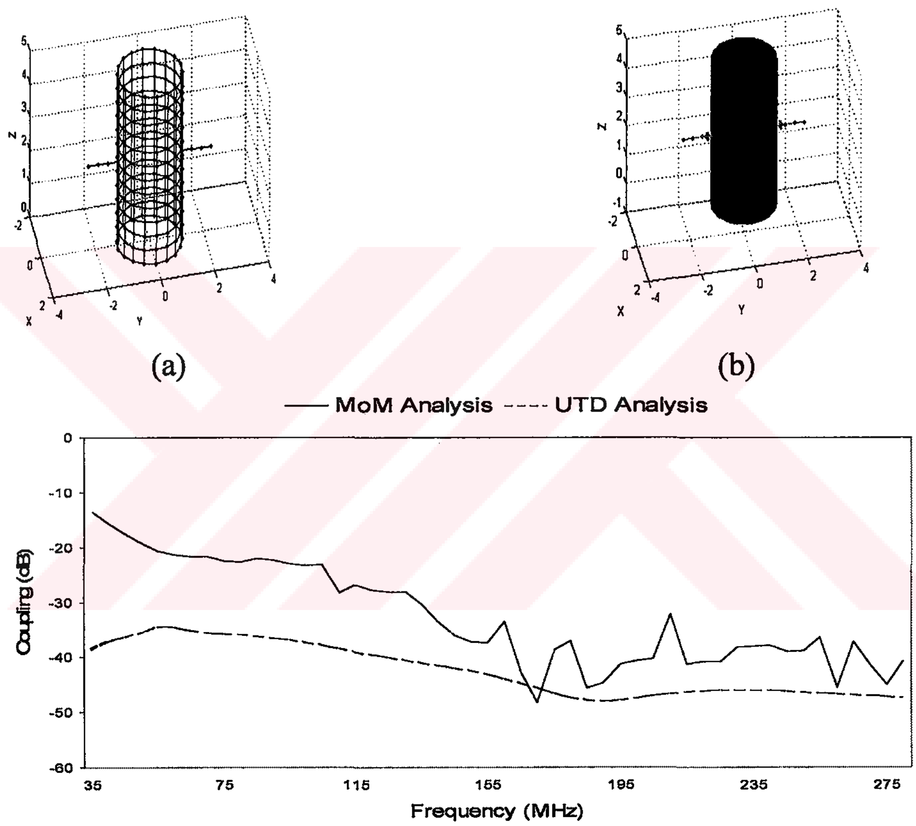

(c)

Figure 4.4: (a) Aircraft-like structures and monopole antentannas modelling by the MoM, (b) UTD and (c) coupling vs. frequency

4.3. Preperation of the Numerical Model

The digitized model of the Phantom can be implemented in two ways: The first is modelling the surface of the aircraft using the surface patches. In this solution, the magnetic field integral equation (MFIE) is utilized. In this method, the surface has to be completely closed. The patches must also be as small as possible for in-detail representation of the aircraft fuselage.

The other way of digitizing the EM structure is the wire-grid representation. In the solution of wire-grid structure, the electric field integral equation (EFIE) is utilized. In this study, the wire-grid method is used for modelling of the surfaces. Therefore only the EFIE is utilized. The reason is the easier implementation of the wire-grid modelling, high accuracy and easier matching with the antennas.

The fuselage of the Phantom is constructed of highly conductive metal alloys. So the body of the aircraft has considerable effect on the antenna coupling and radiation patterns. Recalling the wire-grid structure in the previous chapter, the body has to be modelled as a mesh of segments matching the criteria in Table 4.2 [43].

Table 4.2: Segmentation criteria for the MoM (Δ = segment length, λ = the wavelength and a = the segment radius)

Individual Segments	Acceptable Range
Segment length	$\frac{\lambda}{10} < \Delta < \frac{\lambda}{5}$
Radius	$30 < \frac{\lambda}{a} < 100$
Segment length to radius ratio	$0.5 < \frac{\Delta}{a} < 2$

The MXF-483/484 transreceiver utilizes the Very High Frequency/ Ultra High Frequency (VHF/UHF) range, therefore the segmentation has to be done around 140 MHz. Therefore, from Table 4.2, coupling in the frequency range from 70 MHz to 280 MHz can be investigated.

Three-Dimensional (3-D) model of the Phantom was required for preparing the input file representing the wire-grid model of the aircraft.

4.3.1. The wire-grid model

The cross-sections of the F-4 Phantom obtained from the PM company are shown in Figure 4.5 [33]. These cross sections on various parts of the aircraft are 1:72 scaled on a A-4 paper. In order to assure the validity of these cross sections, some key distances such as the wingspan, air intake width etc. are compared with the original values and an existing 1:32 scaled model and it was seen that the the drawings are in good agreement with the original values. This step is very important, because any error introduced at this stage will lead to higher analysis and measurement erros at the preceeding stages. The body centerline of the aircraft is assumed as the z-axis. So, at each cross-section the z-coordinate is constant while x and y coordinates vary.

At the next step, these cross sections are scanned and converted to raster files by the TraceArt software. In this form, the cross sections are readable by the CAD software. The cross-sections are then re-scaled & re-oriented to original sizes and digitized by using a CAD software (Figure 4.6).

After the x-y coordinates of each segment are obtained, the input file for the Structural Interpolation and Gridding (SIG) software is prepared. The only way to prepare wire-grid structures for complex objects is using special software. The NEC wire-grid input file contains;

- A single z-cordinate and various x-y coordinates for each cross-section,
- The frequency at which the segmentation will be done according to the Table 4.2 and
- Additional labels and coordinates for planar parts such as wings that do not need cross-section data.

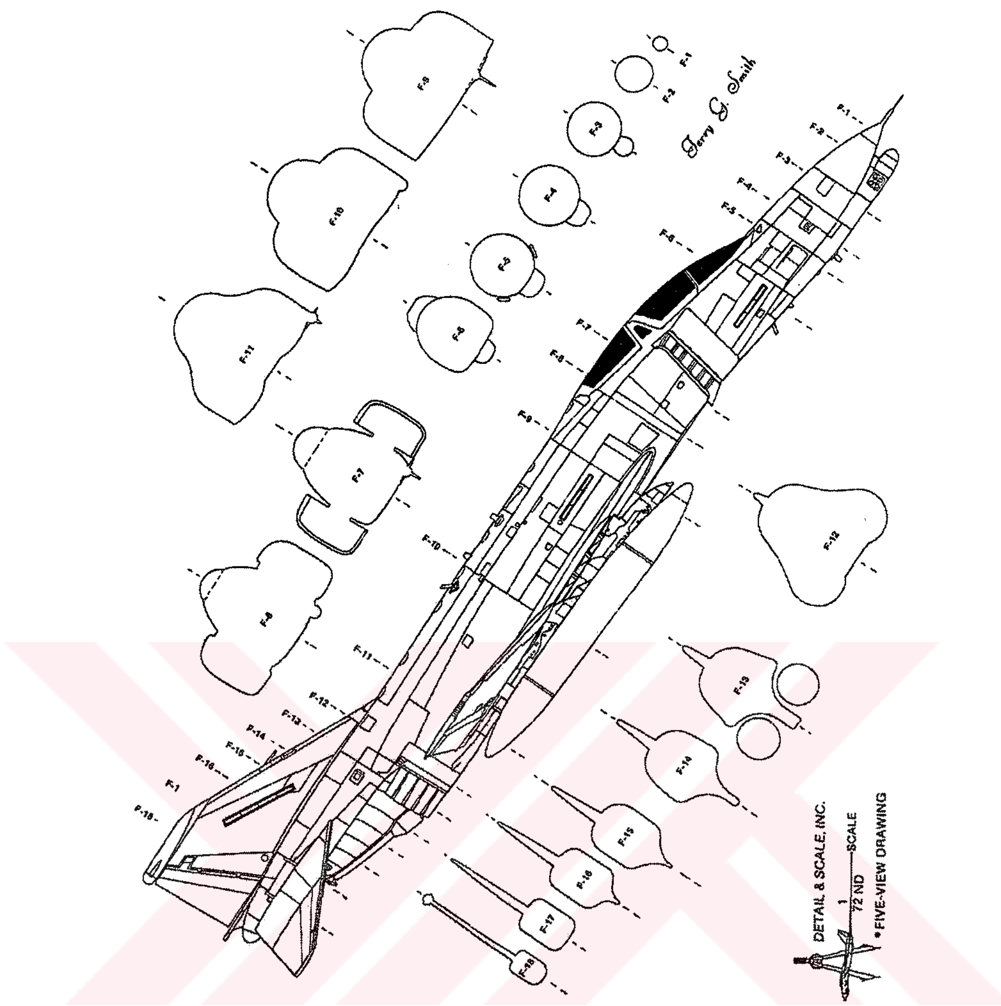

Figure 4.5: 1:72 Scaled cross-sections of the Phantom [33]

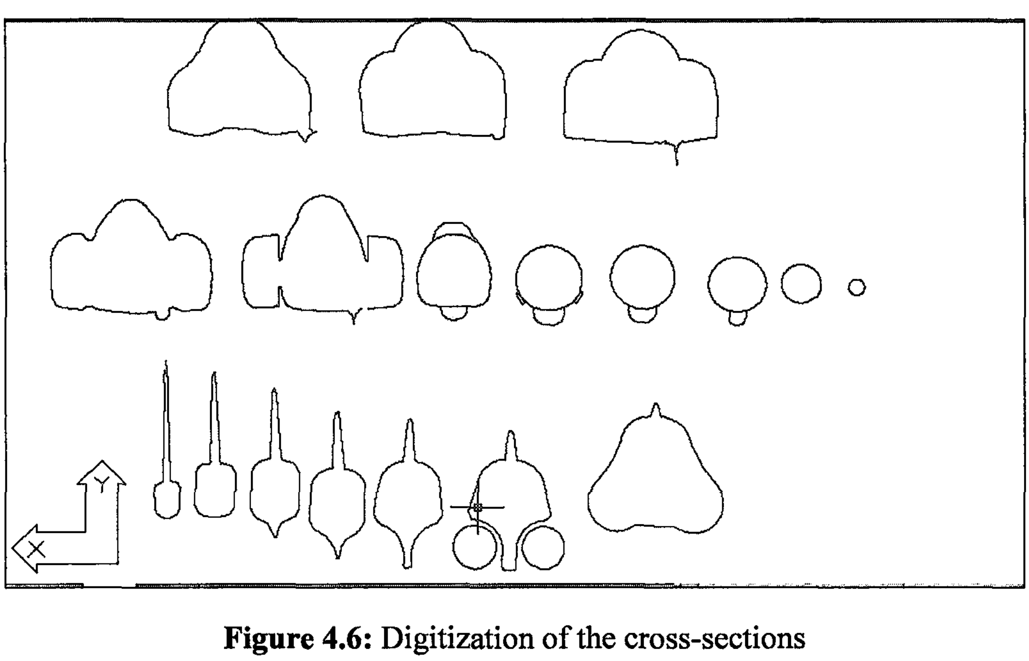

Figure 4.6: Digitization of the cross-sections

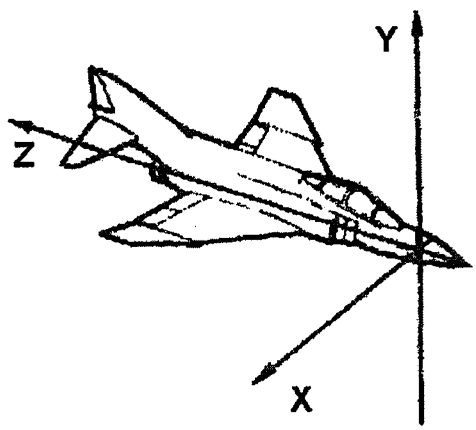

Figure 4.7: Axes of the aircraft [54]

The whole structure is automatically augmented i.e. additional cross sections are generated providing the wire segments at Table 4.2. The process is illustrated in Figure 4.8. However, some of the segments may contain errors. The SuperNEC automatically detects these errors. Some errors are corrected by the program but most of them are corrected by hand. The final wire-grid model is shown in Figure 4.9. The model is segmented at 140 MHz. There are 6855 segments and the average segment size is 20 cm's. This model enables analysis in the 70-280 MHz range which covers the spectrum of the VHF-UHF transreceivers.

The final digitized model is an input file for the SNEC. The model is checked for the criteria in Table 4.2 and all the errors are fixed.

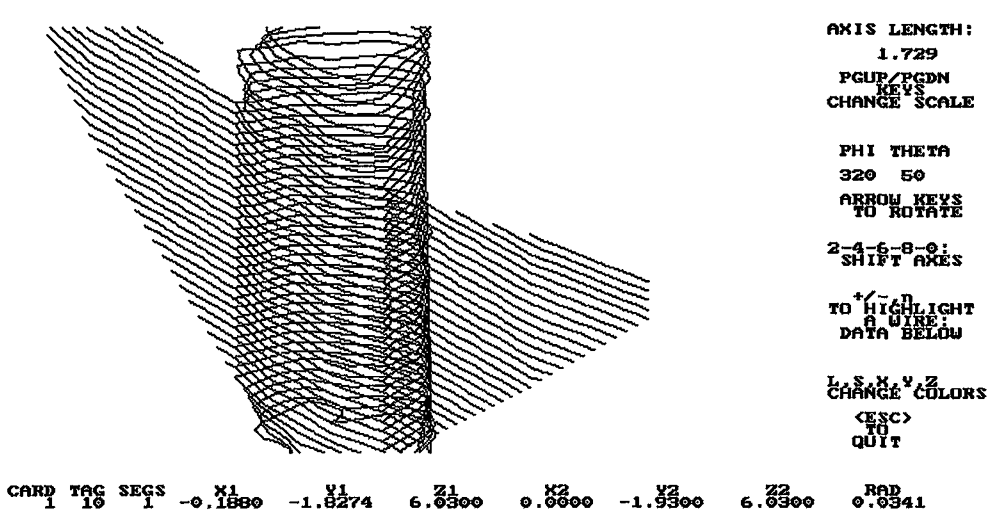

Figure 4.8: Augmentation of cross-sections by using the SIG

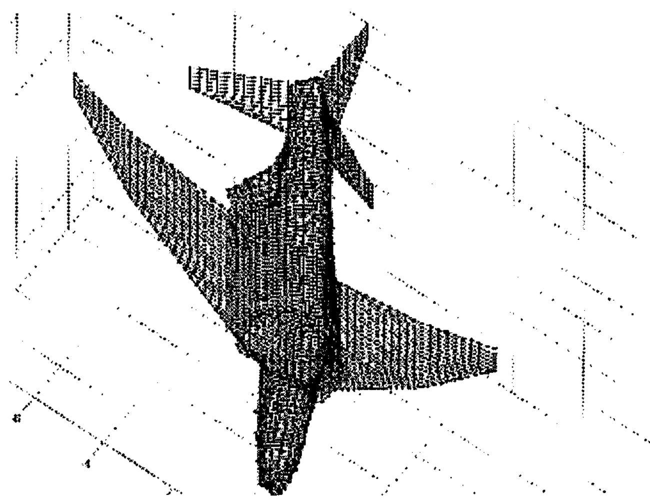

Figure 4.9: Final wire-grid model of the Phantom

4.3.2. EMI induced by the transmitters

The main reason of EMI during the simultaneous operation of the two transreceivers is the one caused by the harmonic emissions. These emissions are illustrated in Figure 4.10. Harmonically related transmitter emissions include those undesired spurious emissions that are integer multiples of either the fundamental frequency or frequencies used to generate the fundamental, e.g., a master oscillator or crystal-controlled clock. Precise specification of harmonic-output power is complicated because of significant variations from serial number to serial number for a particular transmitter nomenclature. As a result, harmonic output power level must be represented statistically. For harmonic emissions, as for the fundamental emission, power is spread over a frequency range. The overall broadband noise emission is shown in Figure 4.11.

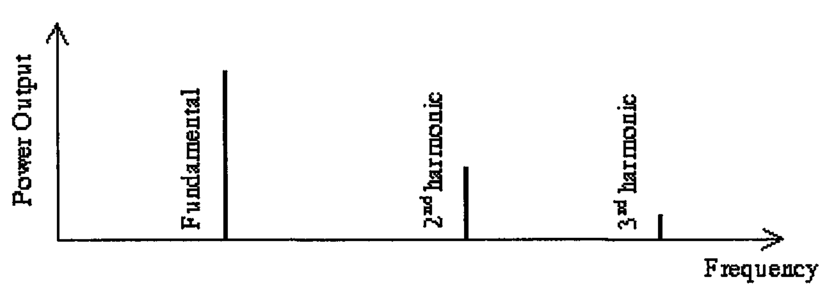

Figure 4.10: Fundamental and harmonic emissions [2]

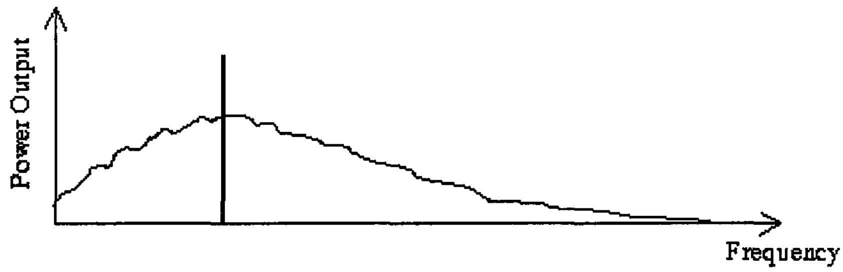

Figure 4.11: Broadband noise emission [2]

Bearing in mind that the transreceivers operate at the VHF and UHF frequency range and in no circumtances both transmitters operate at the same frequencies, minimization of coupling caused by the second harmonic is aimed. The frequency range of the transreceivers is given in Table 4.3.

Table 4.3: Operation ranges of the transmitters

Frequency Range	**Mode of Operation**
30-88 MHz	VHF-FM
108-118 MHz	VHF-AM (Receive Only)
118-174 MHz	VHF-FM/AM (ATC, Air to Air and Marine Communication)
225-400 MHz	UHF-AM/FM

4.4. Coupling Optimization

In the previous sections the suitable search method for the analysis, the method for calculating the coupling by the Linville Method and the explanation of wire-grid NEC input file representing the aircraft was presented. The next step is setting up the structure and the parameters of the CPGA and CPMA

4.4.1. Optimization with the CPGA

The CPGA is a proven method for solving complex problems. In the previous studies, it was seen that the CPGA is superior to the BGA in terms of higher precision and faster calculation [22]. The necessary steps for optimization with the

CPGA is setting up the chromosome type, the population type and the cost function. These steps will be implemented in the next sections respectiveliy.

4.4.1.1. The chromosome type

In this study, the EMC will be will be provided by changing the antenna position and orientations. Therefore the main parameters of the cost function to be used in the CPGA are the antenna coordinate and orientations. The designated positions of the antennas are on the spine and the under parts of the center fuselage (Figure 4.12). These parameters in cartesian coordinates are given in Table 4.4. These parameters are bounded with the physical dimensions of the aircraft. The positions are free of other antennas and sub-systems. The existance of the wing between the antennas also provides a good isolation.

The structure of the CPGA consists of chromosomes. For the current situation a chromosome is in the form of Figure 4.13. Some of the parameters in Table 4.4. constitute the genes in the chromosome.

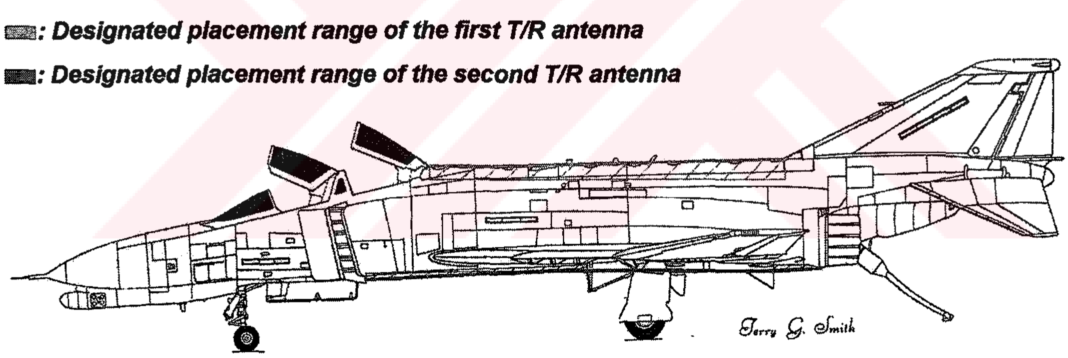

Figure 4.12: Designated positions of the transreceiver antennas [33]

Table 4.4: The available placement ranges of the transreceiver antennas

Parameter	**Abbreviation**	**Range**
Upper antenna x-axis	X_{up}	+0.19...-0.19 m
Upper antenna y-axis	Y_{up}	0.0...-0.097 m
Upper antenna z-axis	Z_{up}	+7.087...+14.006 m
θ Upper Antenna (the angle between the y and z axis)	θ_{up}	+45...+135 degrees
Φ Upper Antenna (the angle between the y and x axis)	Φ_{up}	+27...-27 degrees
Lower antenna x-axis	X_{down}	+0.21...-0.21 m
Lower antenna y-axis	Y_{down}	-1.93...-1.95 m
Lower antenna z-axis	Z_{down}	7.087...14.006 m
θ Lower Antenna	Θ_{down}	-45...-135 degrees
Φ Lower Antenna	Φ_{down}	+5...-5 degrees

X_{up}	Z_{up}	θ_{up}	X_{down}	Z_{down}	θ_{down}	reserve	reserve	reserve	reserve

Figure 4.13: The chromosome structure in the GA

4.4.1.2. The population type

The population is a collection of the chromosomes. The population size and number of iterations required to solve the problem are inversely proportional. There is no 'exact' ratio between the number of genes and the size of the population. In the previous applications, the population size was taken 100 times the number of genes. However, for the current situation, the physical boundaries are in the order of meters and the antennas can be placed only at the segment intersections. Considering that the average segment length is around 20 cm's, the resolution of antenna placement coordinates is approximately 20 cm's. Putting the antennas at somewhere else than the segment intersection may lead to substantial errors because in MoM the wire currents are calculated at the segment intersection points. The process is shown in Figure 4.14.

Figure 4.14: Right and wrong placement of the antennas on the wire-grid structure

This is a very important point in terms of the search space reduction. The calculation duration of coupling between antennas for a single frequency on the final model is in the order of ten minutes on a Pentium-4 PC with 1 Gigabytes of RAM. Taking into account the quantized search-space, the number of the population is decided to be taken as five times the number of genes which makes 30 chromosomes. For the crossover a typical ratio of 30 percent is selected [30]. However, for the mutation, a higher than usual ratio of 30 percent is selected due to high number of local minimums in the cost function. The population of the CPGA is founded as in Table 4.5.

Table 4.5: Population structure of the CPGA

Number of Genes	6
Gene Type	Floating Point Real Variables
Number of Chromosomes	30
Crossover Ratio	% 30
Mutation Ratio	% 30
Iteration Stop Criteria	Differerence between 2 sequantial cost functions is less than one percent

4.4.1.3. The cost function

The second important step in the CPGA is the determination of the cost function. The cost function is the criteria upon which the problem is founded. For the current case, the minimization of the coupling caused by the second harmonic EMI is aimed. The second harmonics of the frequencies and their intended EMI frequencies are given in Table 4.6.

Table 4.6: Possible EMI between the VHF/UHF transmitters

1st antenna Mode of Operation	**2nd Harmonic Frequency**	**2nd Antenna EMI Frequency**
35 MHz VHF-FM	70 MHz	70 MHz VHF-FM
70 MHz VHF-FM	140 MHz	140 MHz VHF-FM/AM ATC and Marine
140 MHz VHF-FM/AM ATC and Marine	280 MHz	280 MHz UHF-FM/AM

The formulation of the coupling can than be defined as:

$$cost\ function = (C_{70Mhz} + C_{140Mhz} + C_{280Mhz}) / 3 \qquad (4.97)$$

where C_{iMhz} is a coupling value at (ith MHz) frequency.

4.4.1.4. The flowcarts of CPGA and CPMA

The parameters and the structure of the search algorithm are defined in the previous sections. The main programs flowcharts are given in Figure 4.15.

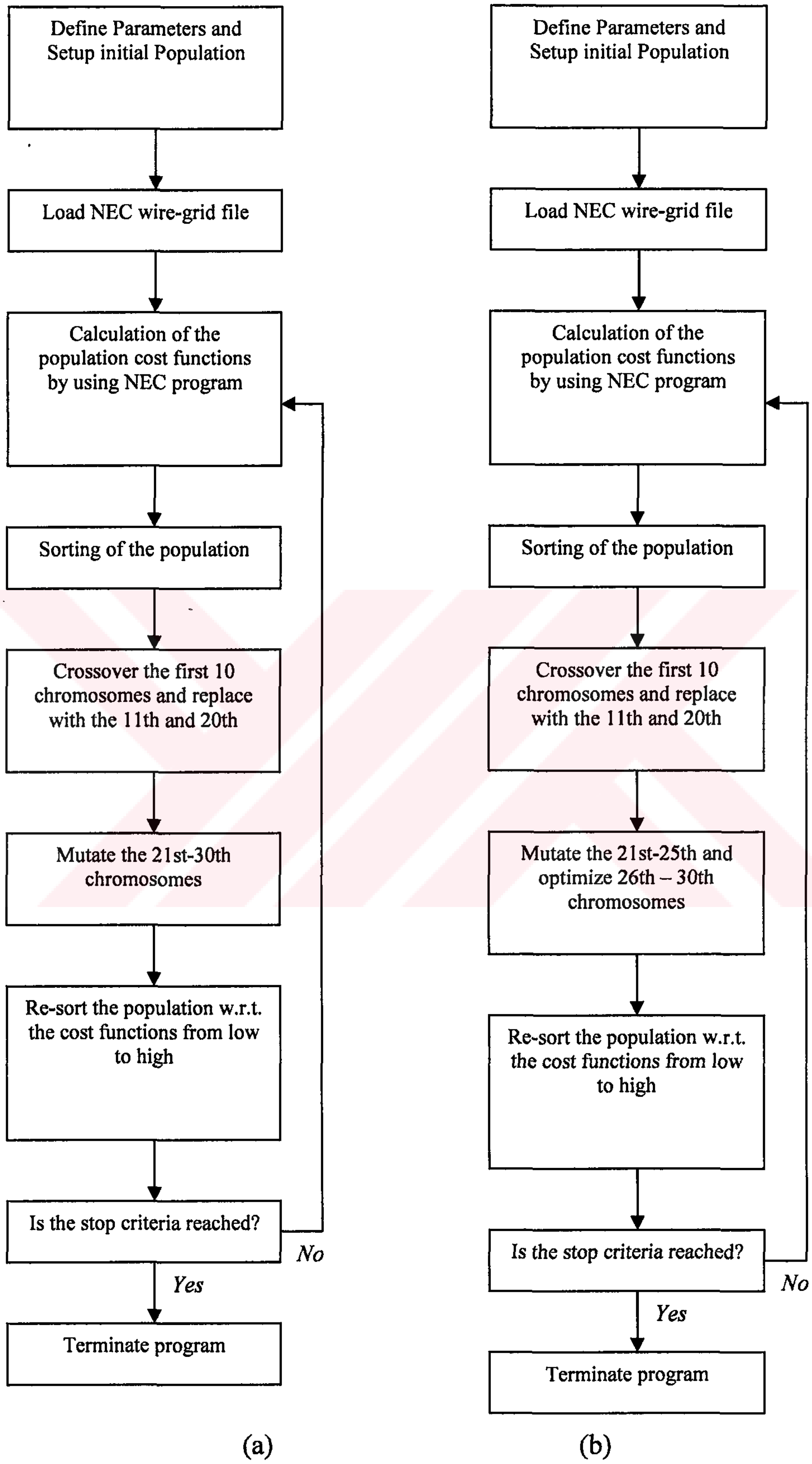

Figure 4.15: (a) The CPGA and (b) CPMA flowcharts for coupling optimization

4.4.2. Optimization with the CPMA

The CPMA is a newly emerging method for solving complex problems [5]. The necessary steps for optimization with the CPMA are setting up the chromosome type, the population type and the cost function. For an accurate comparison with the CPGA, the chromosome and population types and numbers are kept the same. However, the flowchart of the main program is altered as in (b) where the mutation process is decreases fifty percent and local optimization with simplex searh method is implemented. The Simplex-search is a direct search method that does not require gradients or other derivative information [49,50]. If n is the length of x, a simplex in n-dimensional space is characterized by the n+1 distinct vectors which are its vertices. In two-space, a simplex is a triangle; in three-space, it is a pyramid. At each step of the search, a new point in or near the current simplex is generated. The function value at the new point is compared with the function's values at the vertices of the simplex and, usually, one of the vertices is replaced by the new point, giving a new simplex. This step is repeated until the diameter of the simplex is less than the specified tolerance.

4.5. Results of the Numerical Analysis

The CPGA and CPMA programs were run on a Pentium IV personal computer with four gigabyes of RAM. For the CPGA and CPMA methods, it took 64 hours and 47 hours respectively to find the desired parameters. It was also seen that on any other computer with less configuration the program simply rejects to run due to the high number of segments. The results are given in Table 4.6. The variation of the cost function w.r.t. the iteration is given in Figure 4.16. From this figure it can be seen that after the 8^{th} iteration, the cost function stays constant for CPGA. Therefore it is assumed that the algorithm finds the desired global minimum point at this stage. Increasing the number of iterations after this step does not change the result too much.

Table 4.7: The antenna positions

Parameter	Calculated Value	
	CPGA	**CPMA**
Upper antenna x-axis	-0.10 m	-0.17 m
Upper antenna z-axis	8.74 m	10.30 m
Upper antenna θ angle	-63.68degrees	-55.78 degrees
Lower antenna x-axis	0.04 m	-0.19 m
Lower antenna z-axis	8.97 m	10.26 m
Lower antenna θ angle	67.94 degrees	123.29 degrees
Normalized calculation time	100 units	72 units
Average Coupling	-57.54 dB	-50.22 dB

In Figure 4.16, the variation of the cost function w.r.t. the iteration numbers for the CPGA and CPMA are seen. It is seen that the CPGA reaches the global minimum point after the 8 th iteration. However, the CPMA reaches a local optimum at the 5 th iteration. From previous trials on MoM CEM problems where the cost function has discontinuties and many local minimums, it was seen that the CPGA performs better than the CPMA due to higher number of iterations.

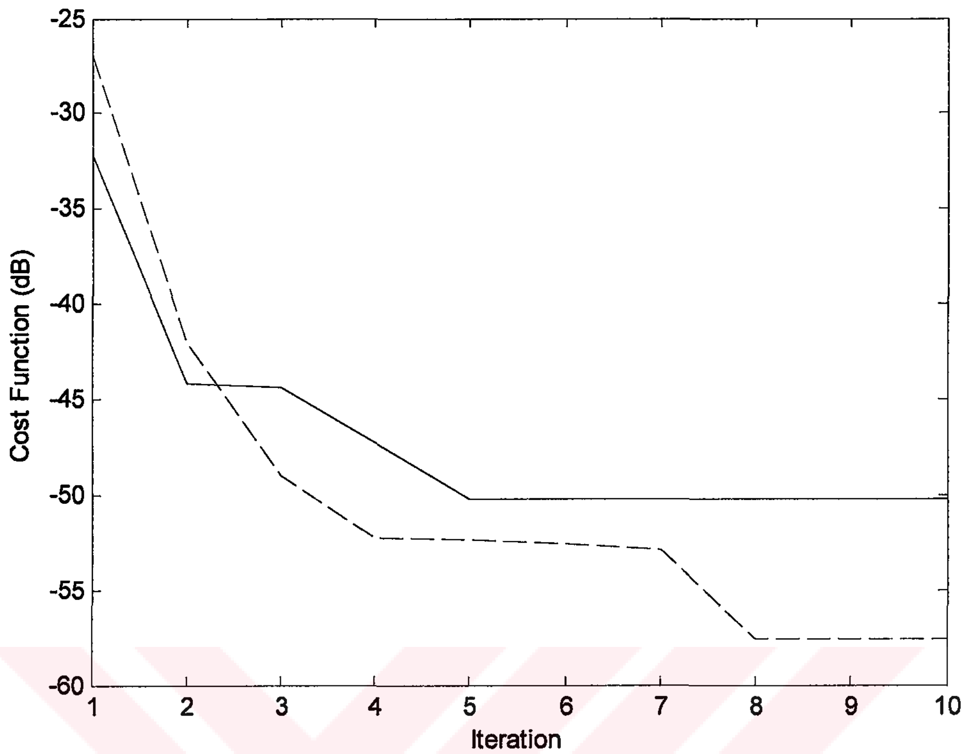

Figure 4.16: Variation of cost function w.r.t. number of iterations for the CPGA (dashed) and CPMA (Solid)

Although the CPMA converges faster than the CPGA, the difference between the final cost functions for both algorithms is considerable. Therefore, the antenna position (Table 4.6) found by the CPGA is selected. However, for making a wide-range frequency comparison between the two algorithms, also the antenna positions found by the CPMA will be investigated in the next section.

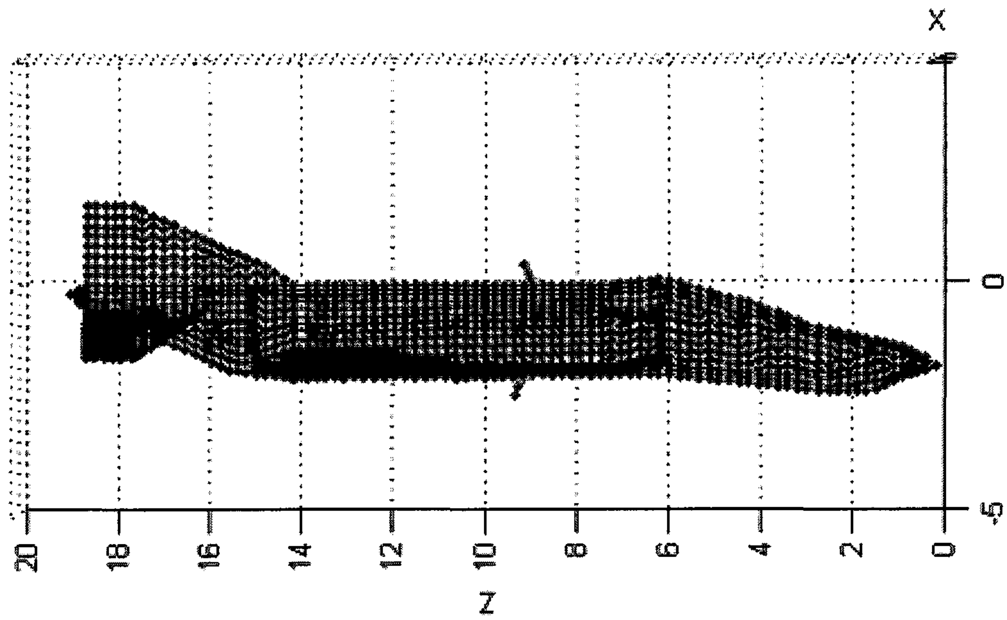

Figure 4.17: Calculated positions of the antennas

4.5.1. Evaluation of the results

The accuracy of the results has aready been verified by checking the structure for the segment requirements at the frequencies of operation. In order to determine whether the found coordinates provide the "global minimum" coupling between the antennas some calculations are made for measuring the coupling vs. the,

- orientation of the antennas,
- antenna lengths,
- diameters of the segments representing the antennas,
- number of segments representing the antennas,
- antenna positions and
- propagation frequency

4.5.1.1. Coupling vs. the orientation of the antennas

The coupling of the antennas are calculated for -45<θ<-135 degrees while keeping the other parameters at Table 4.4 constant. The placement of the antennas are shown in Figure 4.18. The variation of coupling vs. θ for the upper antenna is shown in Figure 4.19.

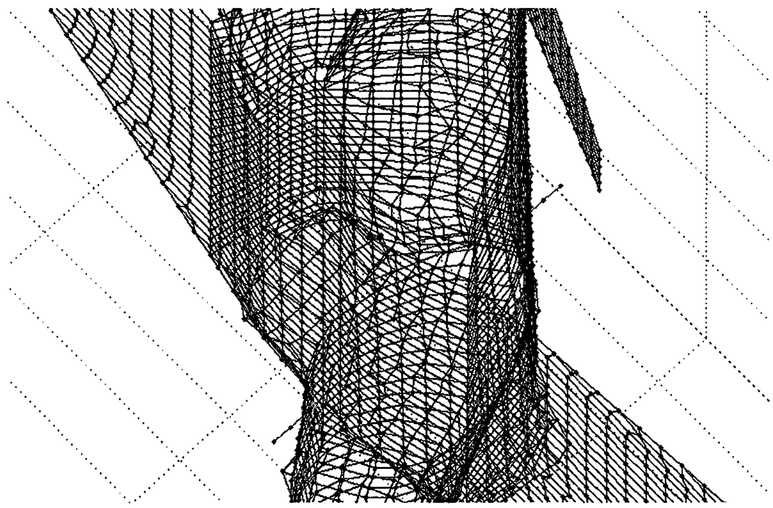

Figure 4.18: Positions of the antennas (red segments)

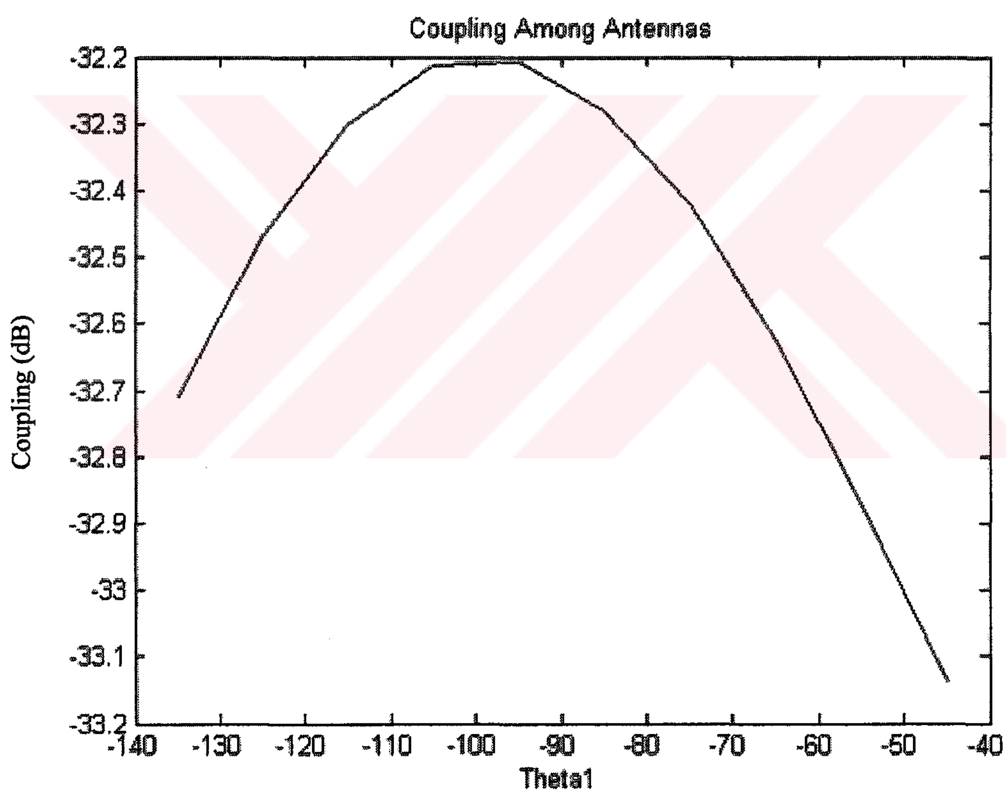

Figure 4.19: Coupling w.r.t. the θ angle of the upper antenna

From Figure 4.19 it can be concluded that the dependence of the coupling on θ is approximately three percent.

4.5.1.2. Coupling w.r.t. the antenna length

The length of the antenna considered in the study is switched electronically at $\lambda/4$ for the operation of frequency. The same variation is also implemented in the simulation. For giving an idea of the dependence of coupling on the antenna lengths, the plot of coupling w.r.t. the antenna lengths is given in Figure 4.20.

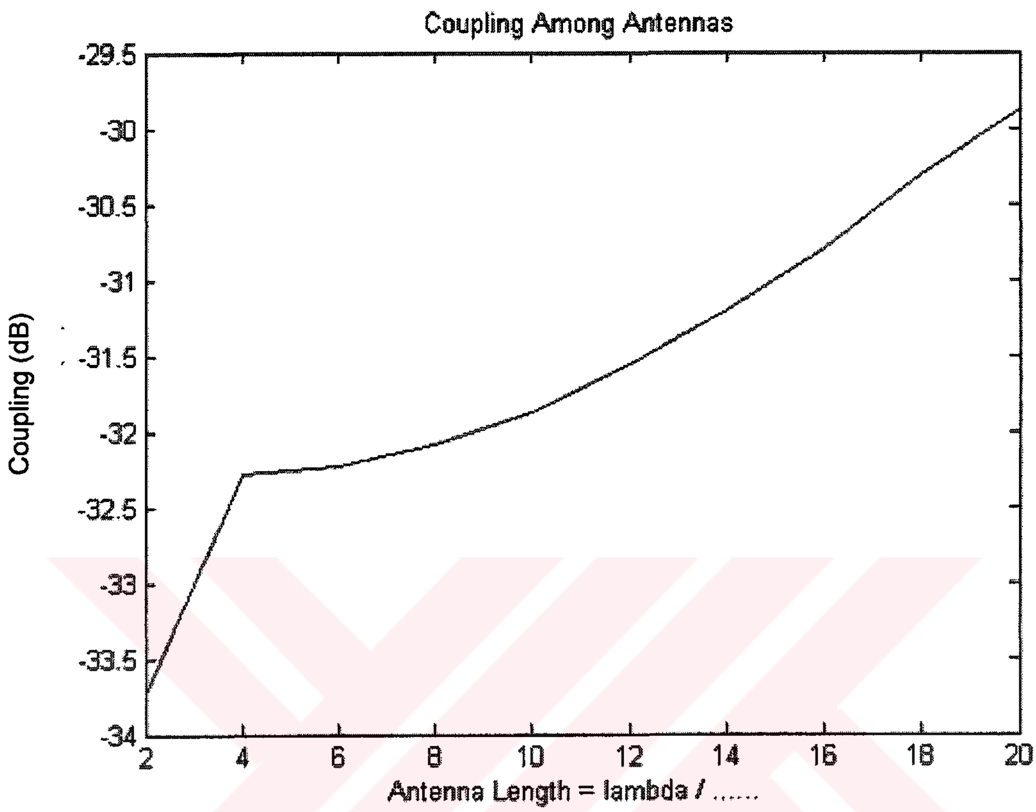

Figure 4.20: Coupling w.r.t. the antenna lengths

4.5.1.3. Coupling w.r.t. the antenna wire radius

The dependence of coupling on the wire radius is shown in Figure 4.21. From this figure it can be concluded that the wire radius has very little effect on coupling.

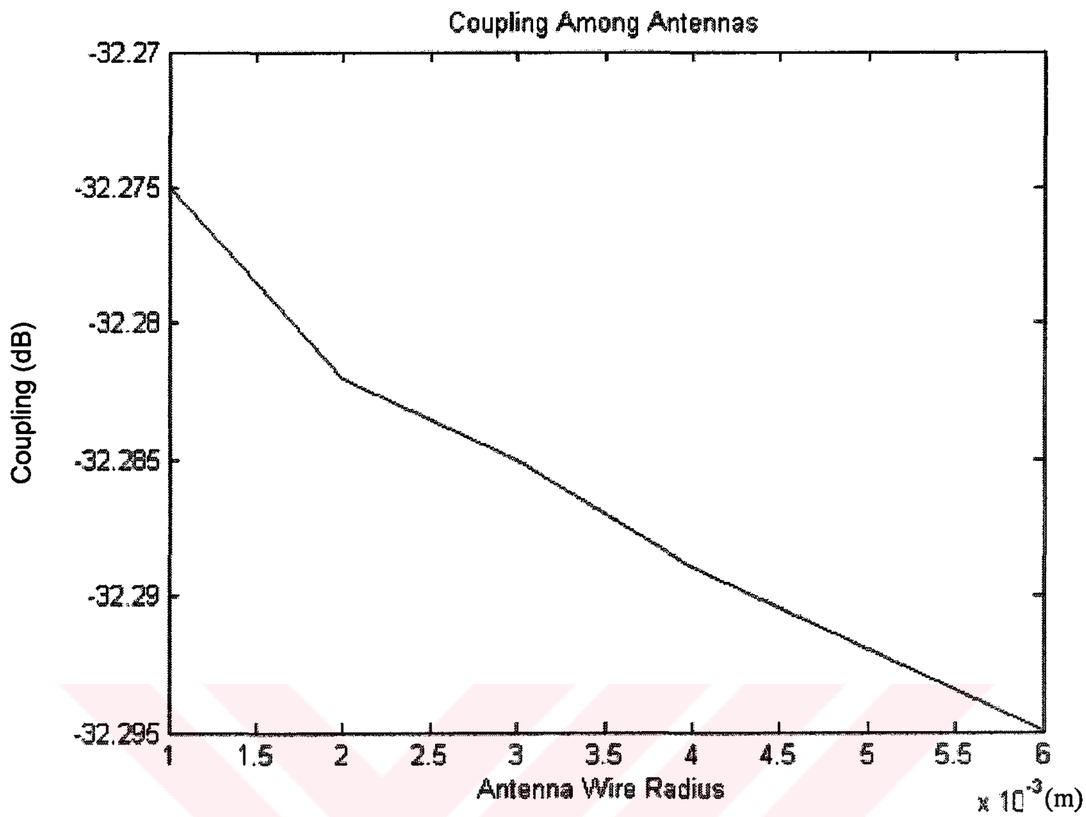

Figure 4.21: Coupling w.r.t. the antenna wire radius

4.5.1.4. Coupling w.r.t. the number of antenna segments

It had already been explained that in the MoM, the length of the segments had to be 1/10 of the wavelength. As the model segmentation was for 140 MHz and the validity of the model was from 70 to 280 MHz, antennas varying in this frequency range can be placed on the structure. However for the UHF frequency range the number of segments decreases with the wavelength. This may pose a problem in terms of simulation frequency. For such cases, in [51] it is reported that this limitation can be decreased from $\lambda/10$ to $\lambda/25$ for the feeding structures. The dependence of coupling on the number of segments is shown in Figure 4.22. In the simulation, number of the antenna segments is taken constant at four.

4.5.1.5. Coupling w.r.t. the antenna positions

Among all the parameters of the antennas the most dominant ones are the antenna positions. From (4.74), the coupling is inversely proportional with the square of the distance between the antenna pairs. When the conductive structure is added to the system, the coupling between the antennas vary in a unpredictable manner due to the scattering and diffraction from the surface.

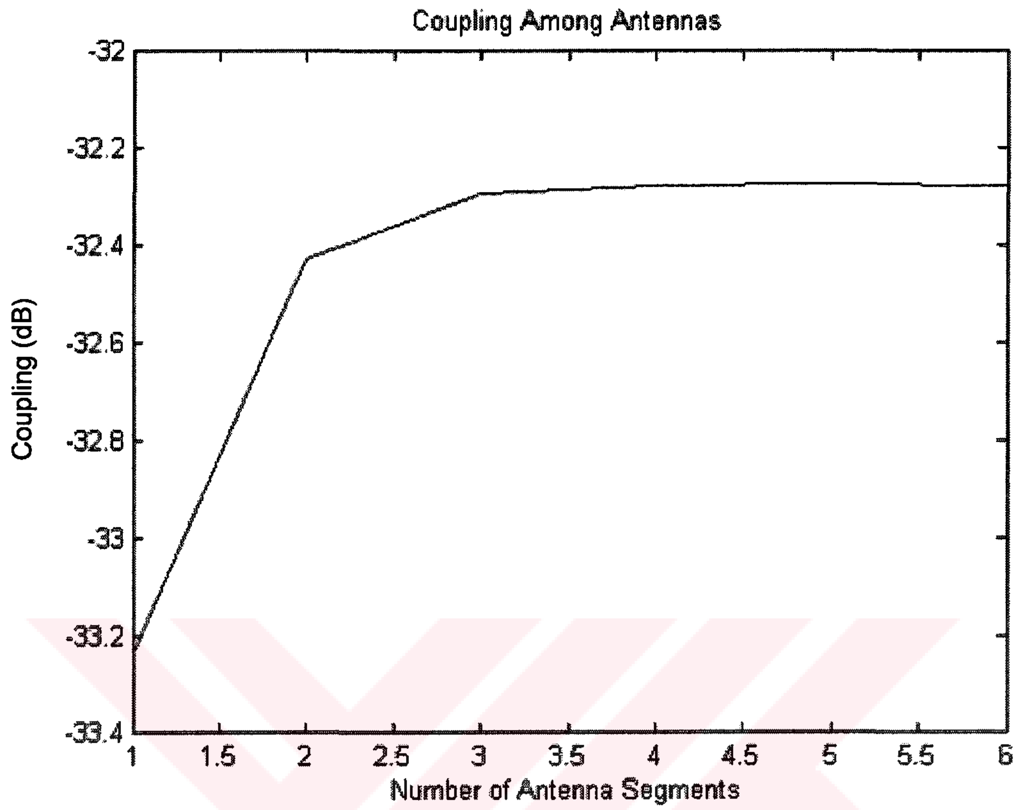

Figure 4.22: Coupling w.r.t. the number of antenna wire segments

For having an idea of how the coupling varies with various antenna positions, the coupling at 140MHz is calculated for 6 discrete, equally-spaced z-values of both the upper and lower antennas in the 7.087m < z < 14.006m range which makes a total of 36 calculations. Meanwhile, the other parameters are kept constant . The contour plot of the simulation is shown in Figure 4.23.

From Figure 4.21 it is seen that, the variation of the coupling is mostly dependent on the complex shape of the aircraft but not on the distance between the antenas. The contours between the sampled points are not actual data but interpolated values for a smooth graphic. As the coupling between the antennas is dependent on 6 different parameters for the problem, these plots will change seriously with the parameters. There are many local minimum and maximums which make the CPGA a suitable optimization method for the selected problem.

4.5.1.6. Coupling w.r.t. frequency

Coupling is plotted for the three discrete frequency values in the cost function in Figure 4.24 where L denotes the antenna length.

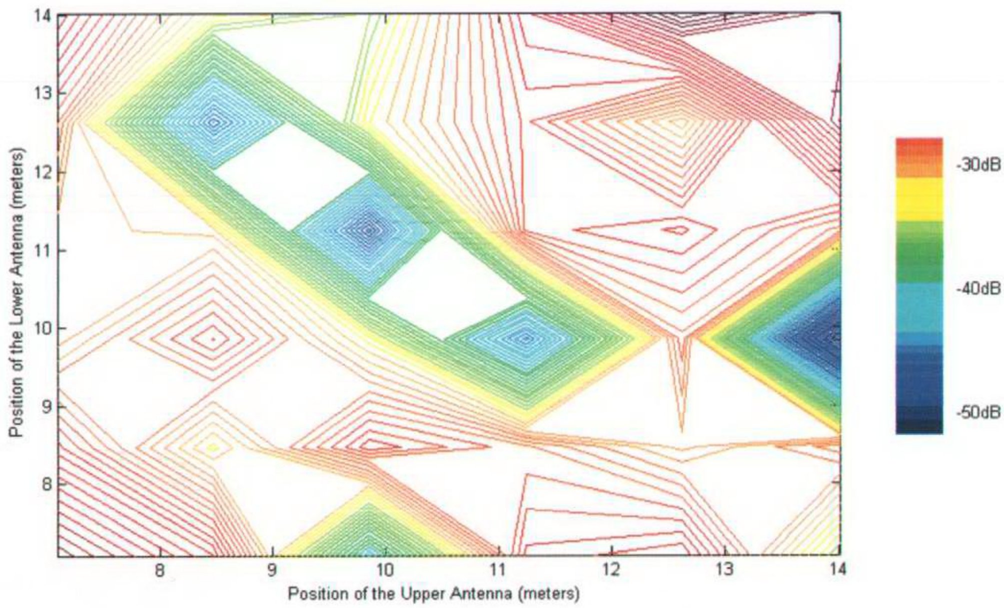

Figure 4.23: Coupling w.r.t. the antenna positions

It is clearly seen that the coupling varies between -5 and -62 dB's which is a large range. Antenna positions corresponding to coupling values in the lower than 25 dB regions are not suitable for mounting [34]. Therefore it can be said that, taking in to account the cost function's value of -57.54 dB's, the numerical analysis is effective in terms of finding the lowest coupling posiiton and orientations. For the validity of the numerical analysis, these results will be compared with the measurements in the anechoic chamber on the scaled model.

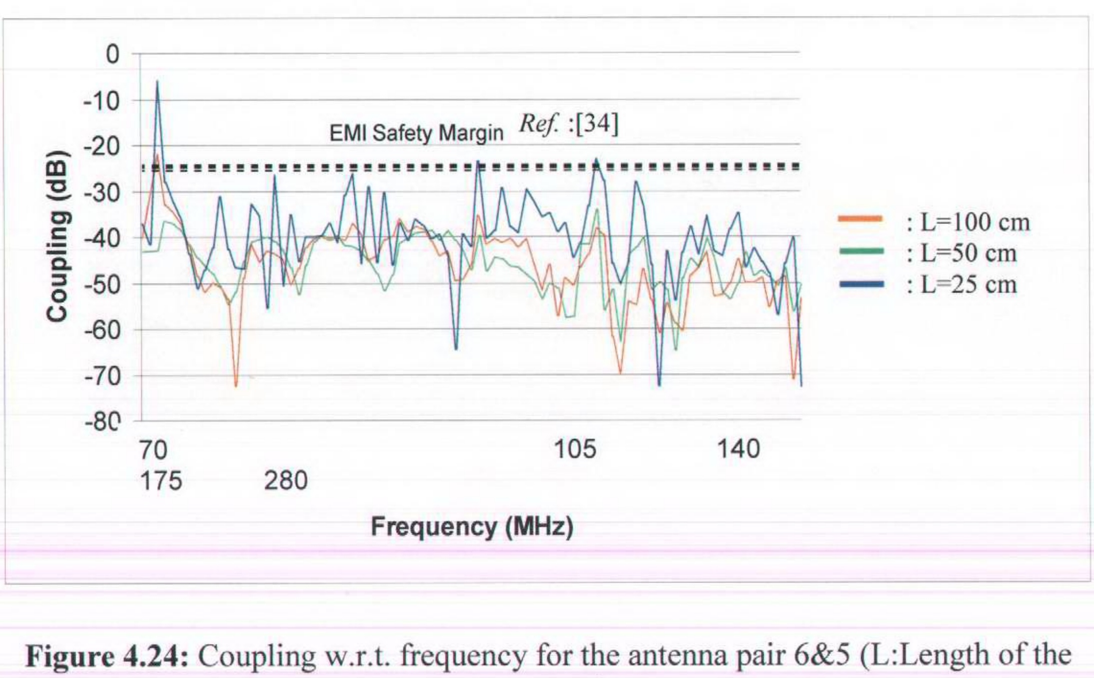

Figure 4.24: Coupling w.r.t. frequency for the antenna pair 6&5 (L:Length of the antennas)

4.6. Radiated Field Calculation

The radiated field of an antenna or re-radiated field of a scattered can be computed from the induced current. The far-field approximation, valid when the distance from the current distribution to the observation point is large compared to both the wavelength and the dimensions of the current distribution, treats the distances $|\mathbf{r}-\mathbf{r}'|$ as constant within the integral except in the phase term, $e^{-jk|\mathbf{r}-\mathbf{r}'|}$. For a structure consisting of a wire portion with contour L and current distribution $\mathbf{I}(s)$, the far-zone field is [43] :

$$E(r) = \frac{jk\eta}{4\pi}\frac{e^{-jkr}}{r}\int_L \left[\left(\hat{k}.\mathbf{I}(s)\right)\hat{k} - \mathbf{I}(s)\right]e^{-j\mathbf{k}.\mathbf{r}}ds \tag{4.98}$$

where r is the position of the observation point $\hat{k} = \frac{\mathbf{r}_0}{|\mathbf{r}_0|}$ and $k = \frac{2\pi}{\lambda}$. The first term inside the bracket can be evaluated in closed form over each straight wire segment for the constant, sine, and cosine components of the basis functions, and reduces to a summation over the wire segments. The radiation pattern of an antenna can be computed by exciting the antenna with a voltage source and using (4.98) to compute the radiated field for a set of directions in space. Alternatively, since the transmitting and receiving patterns are required by reciprocity to be the same, the pattern can be determined by exciting the antenna with plane-wave incident from the same directions and computing the currents at the source point. Procedure of the solution in NEC does not guarantee reciprocity, since the different expansion and weighting functions may produce asymmetry in the matrix. Large differences between the receiving and transmitting patterns or a significant lack of reciprocity in bistatic scattering are indications of inaccuracy in the solution, possibly from the coarse segmentation of the wires.

4.6.1. Radiation Patterns

Radiation patterns are important in terms of evaluating the antenna directivity. The radiation patterns of the antennas are calculated for the upper and lower VHF-UHF antennas. An intermediate frequency of 140 MHz is selected for propagation and the antennas are positioned by CPGA as in Table 4.7. The radiation patterns for the lower antenna from two different aspects is given in Figure 4.25 and Figure 4.26.

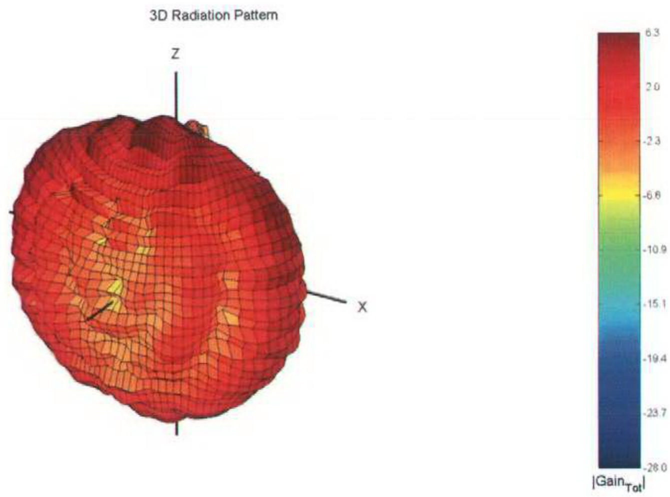

Figure 4.25: Radiation pattern of the lower antenna when looked from the bottom of the aircraft

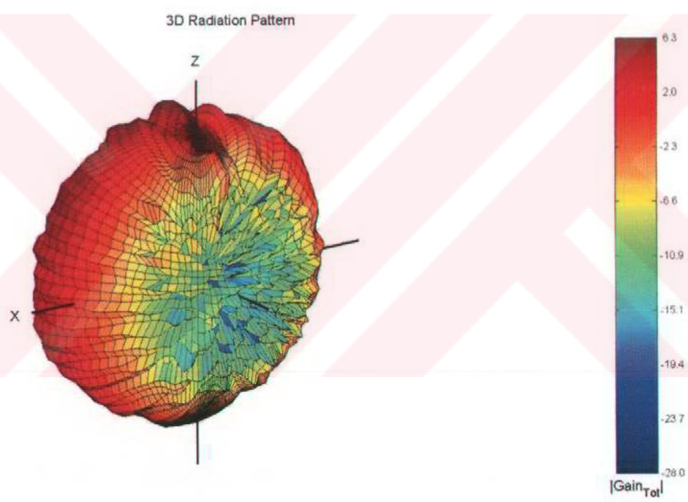

Figure 4.26: Radiation pattern of the lower antenna when looked from the top of the aircraft

The radiation patterns for the upper antenna from two different aspects is given in Figure 4.27 and Figure 4.28.

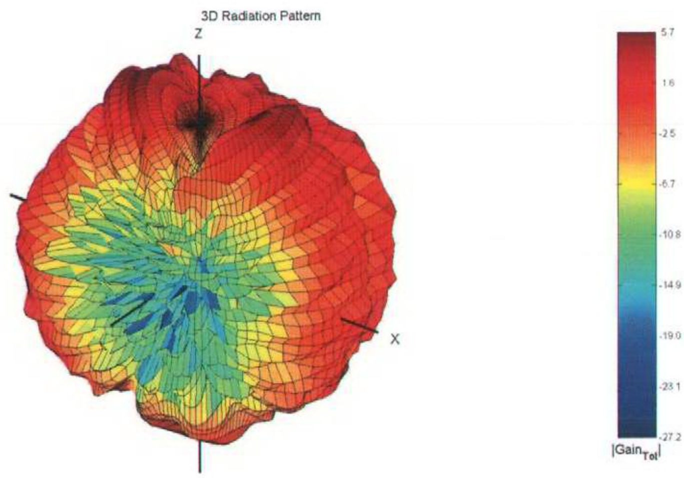

Figure 4.27: Radiation pattern of the upper antenna when looked from the bottom of the aircraft

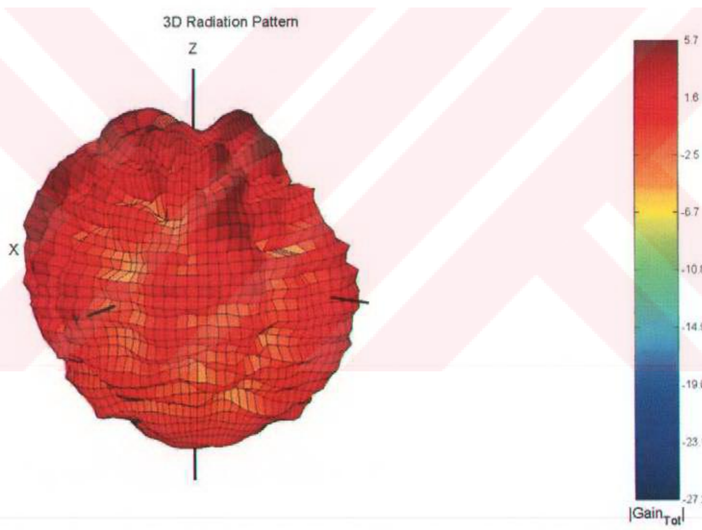

Figure 4.28: Radiation pattern of the upper antenna when looked from the top of the aircraft

From these patterns it is possible to conclude that the transmitters propagate like an omnidirectional antenna. The directivity decreases at the positive y axis (towards the top of the aircraft) for the lower antenna and decreases at the negative y-axis (towards the bottom of the aircraft) for the upper antenna. Considering that this region is very limited, the directivity of the antennas for the calculated positions can be considered adequate for communication.

Most connectorized RF and/ microwave devices have an impedance of 50 W. Free space (generally the transmission media) has an impedance of 377 W. To further complicate matters, most antennas have a free space impedance of their own (a helix

From these patterns it is possible to conclude that the transmitters propagate like an omnidirectional antenna. The directivity decreases at the positive y axis (towards the top of the aircraft) for the lower antenna and decreases at the negative y-axis (towards the bottom of the aircraft) for the upper antenna. Considering that this region is very limited, the directivity of the antennas for the calculated positions can be considered adequate for communication.

Most connectorized RF and/ microwave devices have an impedance of 50 W. Free space (generally the transmission media) has an impedance of 377 W. To further complicate matters, most antennas have a free space impedance of their own (a helix 140 W and ½ wave dipole 70 W). The most efficient transfer of power occurs when the antenna matches the transmission media and/or source impedance. Not all sources are 50 W (CATV is 75W and wave-guide 377 W) and not all impedance is real but for explanation purposes we will use a real impedance of 50 W and ignore imaginary contributions.

Matching the antenna and transmission line to the source impedance is important for a transmitter. The most accepted description of that match is the Voltage Standing Wave Ratio of VSWR. A perfect match is 1.0:1, which indicates the source and load impedance are the same. A bad match depends on the application. For very high power applications (EW systems, radar, radio/television transmitters) anything over 1.5:1 may be unacceptable. Wide band test antennas may have a VSWR of 3.5:1 or more. The ratio describes how much power will be transmitted into the antenna and how much power will be reflected back to the source (see table B-1). The VSWR is then an indication of the efficiency of an antenna. An antenna, which has a poor match, will not be an efficient radiator but an antenna with a good match is not necessary an efficient radiator. In addition to matching the impedance, most transmission sources have coaxial outputs. This type of connector has a grounded shield surrounding the center conductor, which carries the RF/Microwave energy. Many antennas are balanced and both sides of the transmission line are active (such as 300 W twin lead for radio and television). This requires that not only the impedance be transformed but that the unbalanced coax transmission line is transformed into a balanced condition prior to connection to the antenna. The device that accomplishes this is generally referred to as a balun. It is important to note that the best match is obtained with a dummy load, which does not generally radiate at all. This leads to the efficiency.

Antenna efficiency is a complicated and often misused figure. All antennas suffer from losses. A simple horn antenna for example will not be as efficient as a perfect aperture of the same size because of phase offset. The real efficiency of an antenna combines impedance match with other factors such as aperture and radiation efficiency to give the overall radiated signal for a given input. The best and most widely used expression of this efficiency is to combine overall efficiency with directivity (of the antenna) and express the efficiency times directivity as gain.

5. THE MEASUREMENT METHOD AND RESULTS

In this section the measurement procedure is explained and the measurement results are given.

5.1. The Measurement Parameters

The most accurate EM measurements are the ones made on actual platforms. However, due to very high operational costs the measurements can also be implemented on scaled models with reasonable accuracy [2] (Figure 5.1).

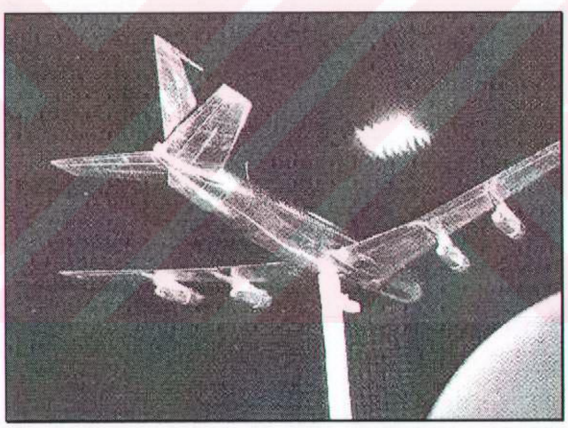

Figure 5.1: Scaled model of a Boeing 707 inside an anechoic chamber [13]

During the preperation of the scaled model, the parameters of the model and measurement setup are altered as in Table 5.1 [15,52-55].

According to these parameters, the frequency for the 1:10 scaled model is 10 times than that of the simulation frequency. Another parameter of interest is the conductivity. The fuselage of the actual F-4 Phantom is aluminium while it is copper in the scaled model due to ease of soldering and shaping. The error introduced can be evaluated by investigating the change in the reflection coefficient w.r.t. the angle of incidence at the boundary layer between two layers (the air and the conductive fuselage).

Table 5.1: Scaling rules of the electrical parameters

Actual Parameter		1:n Scaled Parameter
Length	l	l/n
Frequency	f	nf
Wavelength	λ	λ / n
Conductivity	σ	$n\sigma$
Dielectric Constant	ε	ε
Magnetic Permeability	μ	μ

The reflection coefficient is given as [15]:

$$\Gamma = \frac{\eta_2 - \eta_1}{\eta_2 + \eta_1} \tag{5.1}$$

where, η_1 stands for the impedance of the first media and η_2 stands for that of the second. If air is taken for the first media and conductor for the second, the reflection coefficients are seperately calculated as $\Gamma_{air-alumnium} = -0.9999745$ and $\Gamma_{air-copper} = -0.9999381$. As can be seen from the results, the amount of error is negligible. The EMI frequency band conversion for the measurement setup is given in Table 5.2.

Table 5.2: Frequencies utilized at the numerical analysis and the measurement

Mode of Operation	Actual Frequency	Frequency for the Scaled Model
35 MHz VHF-FM	70 MHz	700 MHz
70 MHz VHF-FM	140 MHz	1.4 GHz
140 MHz VHF-FM/AM (ATC and Marine)	280 MHz	2.8 GHz

5.2. Construction of the Scaled Model

The model is constructed by using the the cross sections which also were utilized for preparing the numerical model. 1:72 scaled cross-sections were re-scaled to 1:10 by a CAD program. The prints of these cross-sections were used to cut the cross sections from 1mm thick aluminium. These cross-sections were installed on 8mm thick wooden spine. The process is shown in Figure 5.2. Next, long narrow strips of wood was laid down along these cross sections for a robust structure (Figure 5.3)

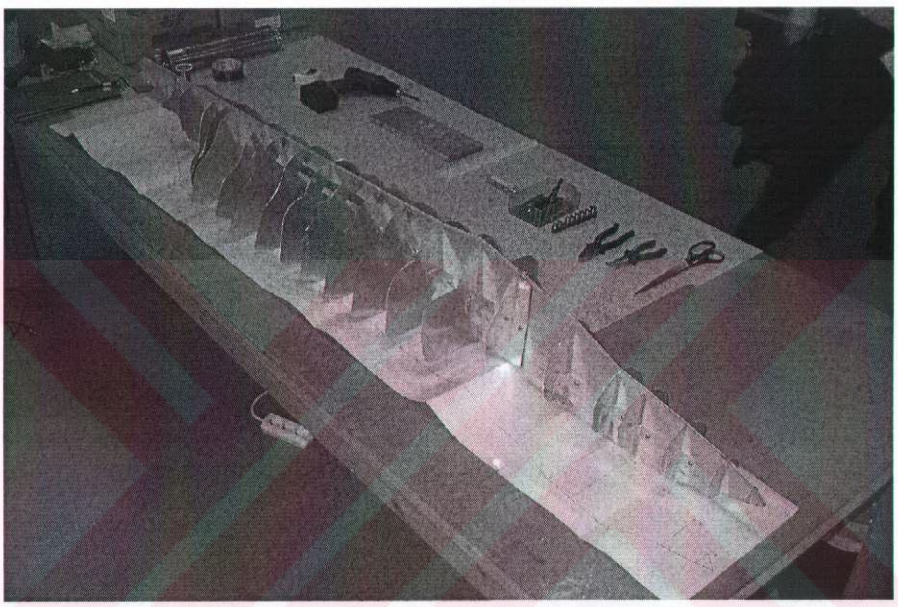

Figure 5.2: Cross sections and spine of the scaled model

Figure 5.3: Reinforcing the model by long narrow strips of wood

After forming the spine of the aircraft, the next thing to do was installing the antenna network. Coaxial cable with an impedance of 50 Ω was used for this purpose. SMA (Sub-Miniature Aperture) connectors were utilized for the installation of the network analyser feed and antenna output ports (Figure 5.4)

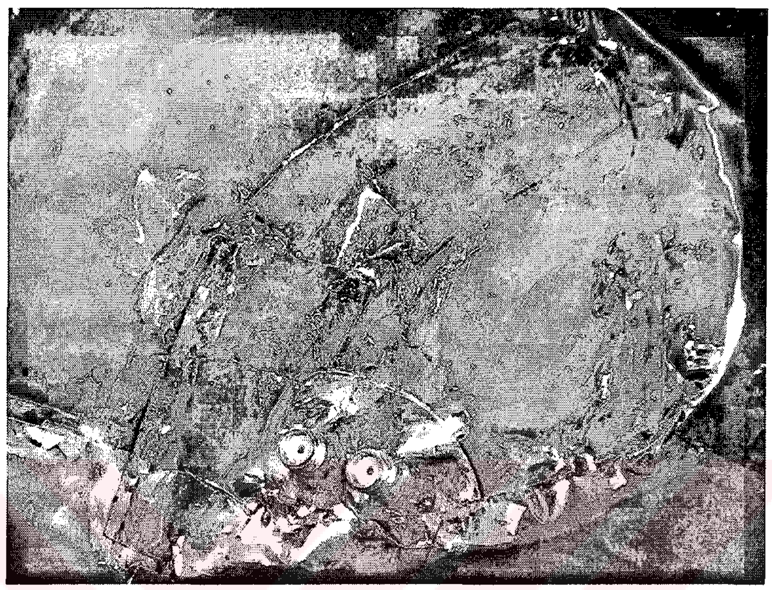

Figure 5.4: SMA jacks for network analyser feed ports at the nozzles of the aircraft

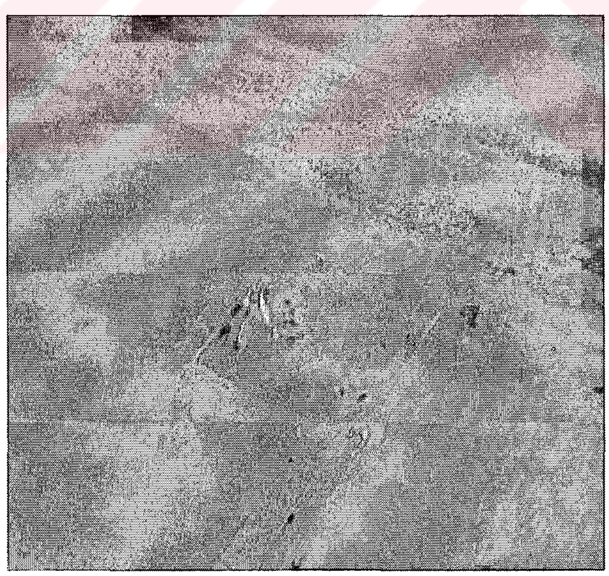

Figure 5.5: The SMA jack for upper antenna port

After the installation of the antenna network, the fuselage was covered with copper. The copper was cut in slices and was attached to the spine by hot-silicon glue gun. Next the copper layers were soldered with a strong soldering gun (Figure 5.6)

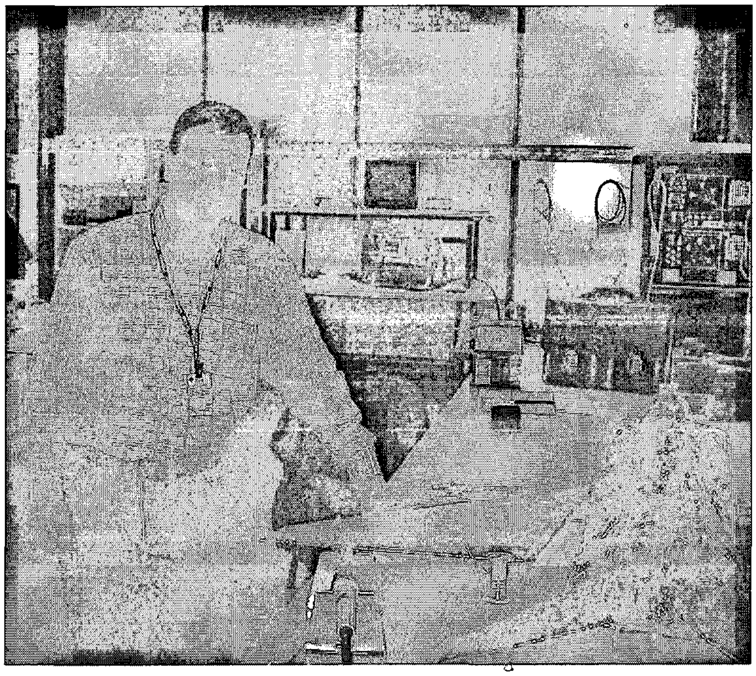

Figure 5.6: Soldering process of the scaled model

5.3. The Measurement Setup

For the measurement, the setup seen in Figure 5.7 is utilized. The network analyser is an Agilent brand, HP8753E model which can measure in the 300 kHz – 6 GHz range For the calibration of the analyser, full two-port calibration method and 3.5 mm's (SMA) calibration kit is used. Calibration is implemented at the antenna terminals and therefore all the antenna and cable losses are taken in to account.

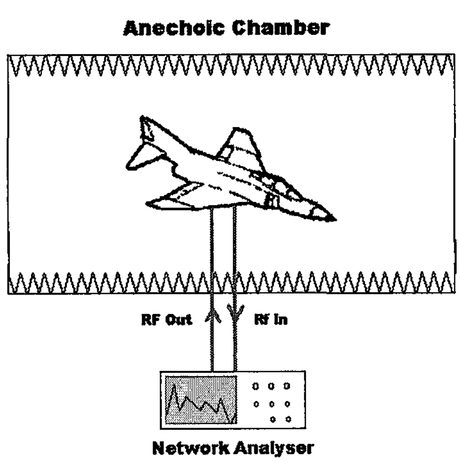

Figure 5.7: Schematic of the measurement setup

In Figures 5.8-9, the scaled model aircraft is seen inside the anechoic chamber. The network analyser probes extending from the SMA connectors at the nozzles of the aircraft are clearly visible. The pyramid-shaped absorbers are portable. So, once the model is installed, all the area surrounding the model can easily be filled with absorbers for representing free space.

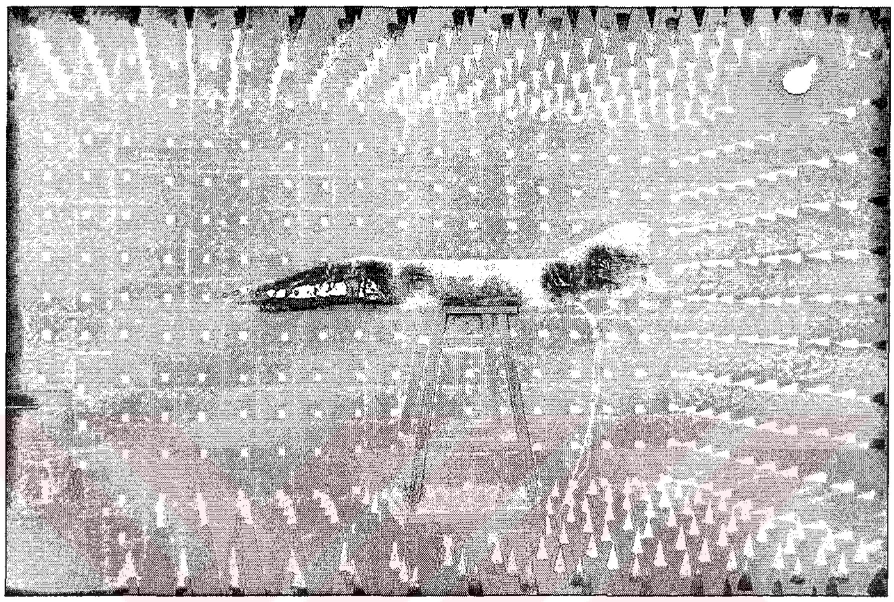

Figure 5.8: The scaled model inside the anechoic chamber

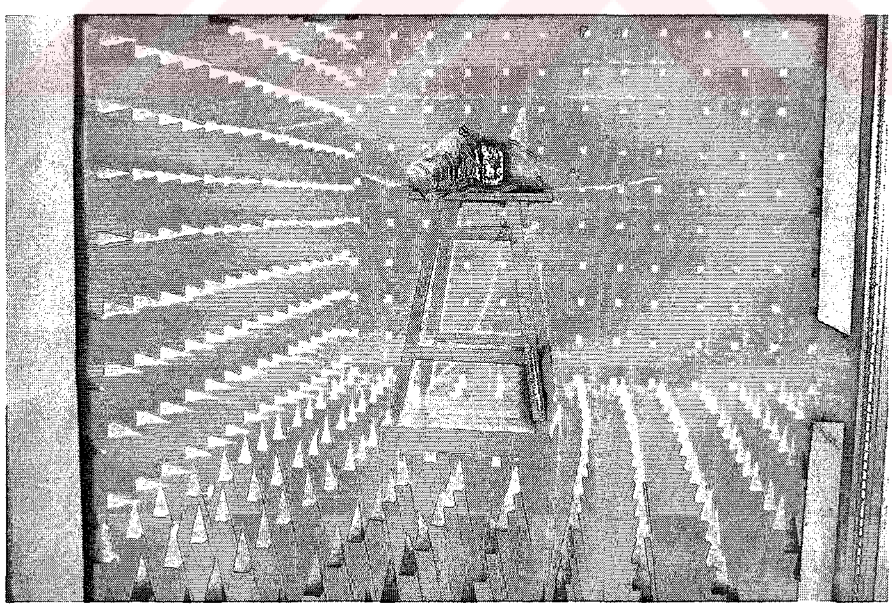

Figure 5.9: Front view of the scaled model inside the anechoic chamber

The antennas were modelled as quarter wavelength monopoles in the numerical analysis. Therefore on the scaled model, the antennas are implenented in the same manner. 1mm's thick emanated copper wires are used as the monopole antennas (Figure 5.10)

Figure 5.10: The upper VHF/UHF monopole antenna

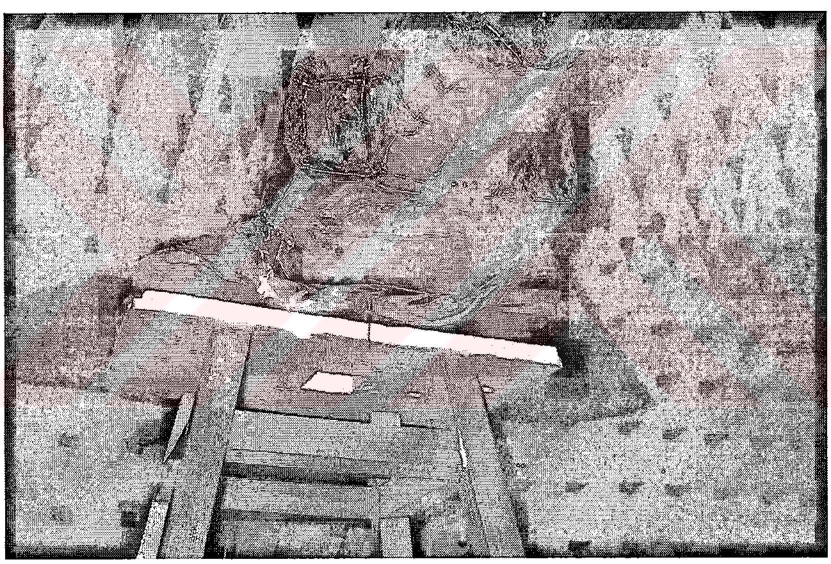

Figure 5.11: The lower VHF/UHF monopole antenna

As also seen from the Figure 5.11, the model is placed on a foam at the top of a wooden stand. These material are widely used for mechanical support purposes due to their EM transparent features.

In Figure 5.12, the anechoic chamber is seen. Inside the chamber is covered with EM absorbing material in pyramid shape. The isolation of the anechoic chamber with the outside media is more than -100dB's which is much more than the lowest coupling values in the numerical analysis.

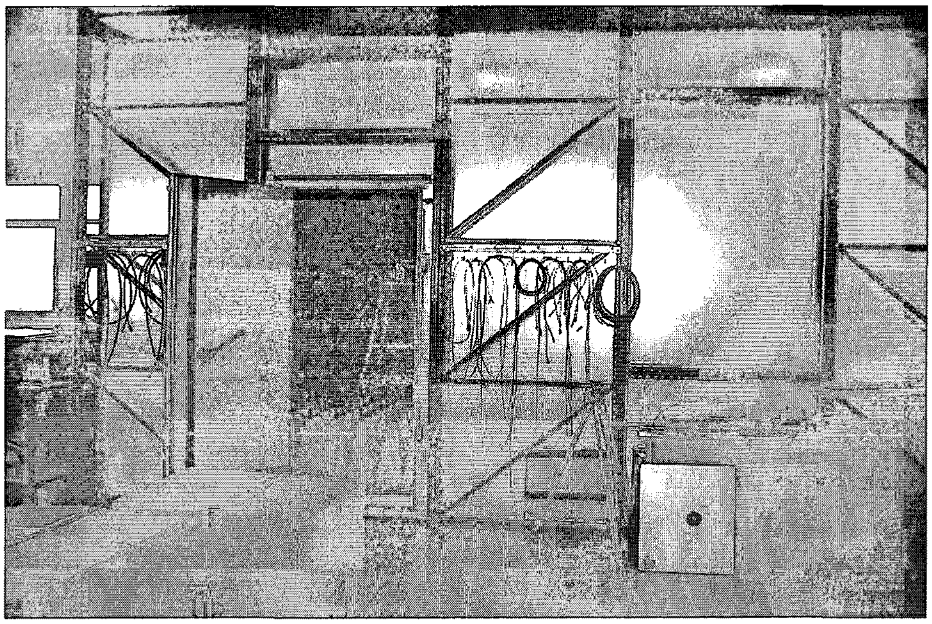

Figure 5.12: The anechoic chamber

5.4. The Measurement Parameters

The parameters measured on the scaled model are the S-parameters which represent the 2-port networks that model the monople VHF-UHF antennas. The parameters are measured on a 50Ω measurement setup, the measurement of S_{21} which represents the coupling between the two antennas and S_{11} & S_{22} which represent the mismatch at the input and output ports will be implemented. For making rasonable comparisons with the numerical analysis the mismatch losses at the input and output ports will also be included. The mismatch loss for port 1 and 2 (ML_1, ML_2) can be measured as:

$$\begin{aligned} ML_1 &= 10.\log(1-|S_{11}|^2) \\ ML_2 &= 10.\log(1-|S_{22}|^2) \end{aligned} \tag{5.2}$$

the maximum coupling can be defined as:

$$C_{\max\_measurement} = 20\log|S_{21}| - 10\log\left(1-|S_{11}|^2\right) - \left(1-|S_{22}|^2\right) \tag{5.3}$$

5.5. The Measurement Results

The coupling measurements are implemented for both the antenna positions calculated by the numerical analysis and random positions. These positions are given in Table 5.3 and shown in Figure 5.13.

Table 5.3: Actual position parameters of antennas used in measurement

Antenna Number	Antenna Position
1	Local Minimum (for comparison)
2	Local Minimum (for comparison)
3	1st antenna position calculated by the CPMA (for comparison)
4	2nd antenna position calculated by the CPMA (for comparison)
5	1st antenna position calculated by the CPGA
6	2nd antenna position calculated by the CPGA

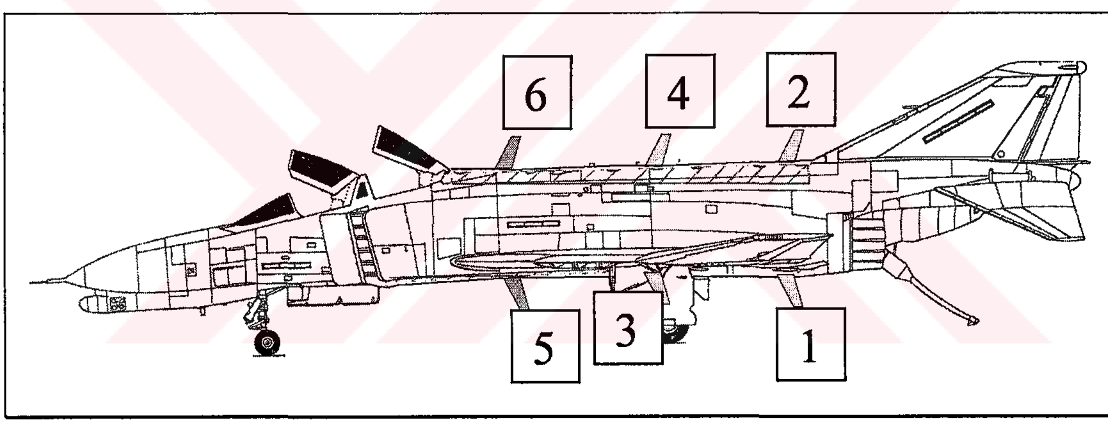

Figure 5.13: Positions of the antennas used in measurement.

5.5.1. Coupling between the antennas 6 and 5

The antennas 6 and 5 are the ones whose positions are calculated by the numerical analysis. The coupling w.r.t. frequency for antenna lengths of 10, 5 and 2,5 centimeters are given in the preceeding three figures respectively.

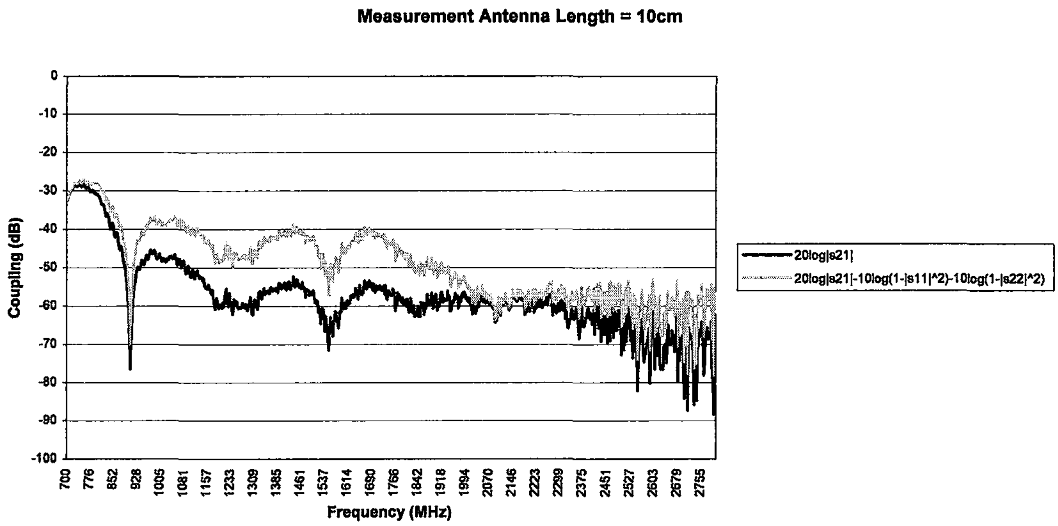

Figure 5.14: Coupling vs.frequency for antennas 6&5 with L=10cm.

In Figure 5.14 the mismatch loss in the 700-900 MHz region is close to zero. This is due to the fact that the antenna lengths are in the propagation wavelength range. There is a sharp descent at the 900 MHz range. The same characteristic appears at all the proceeding coupling plots. The mismatch loss increases after 1GHz and the measurements become inaccurate after 2,2 GHz range due to the mismatch errors at the antenna ports.

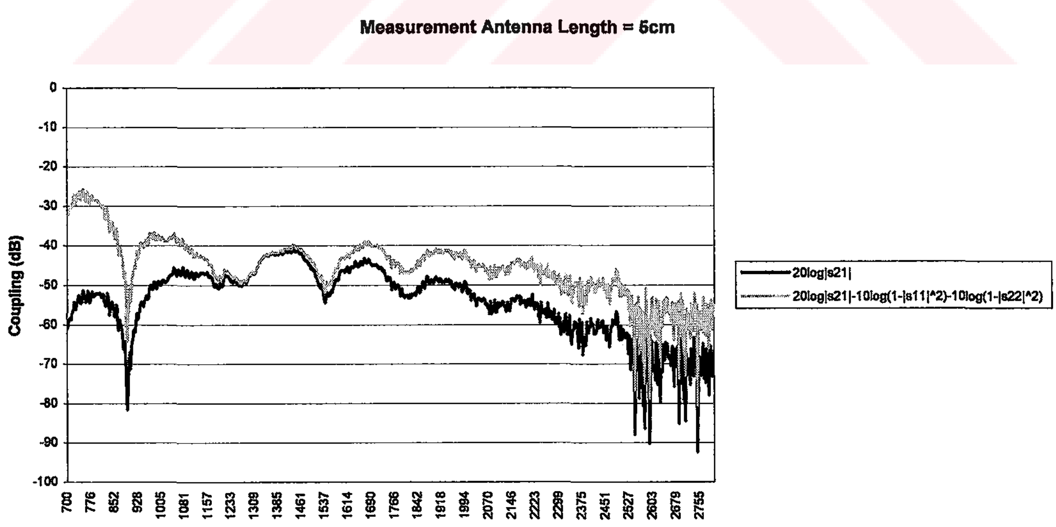

Figure 5.15: Coupling vs. frequency for antennas 6&5 with L=5cm.

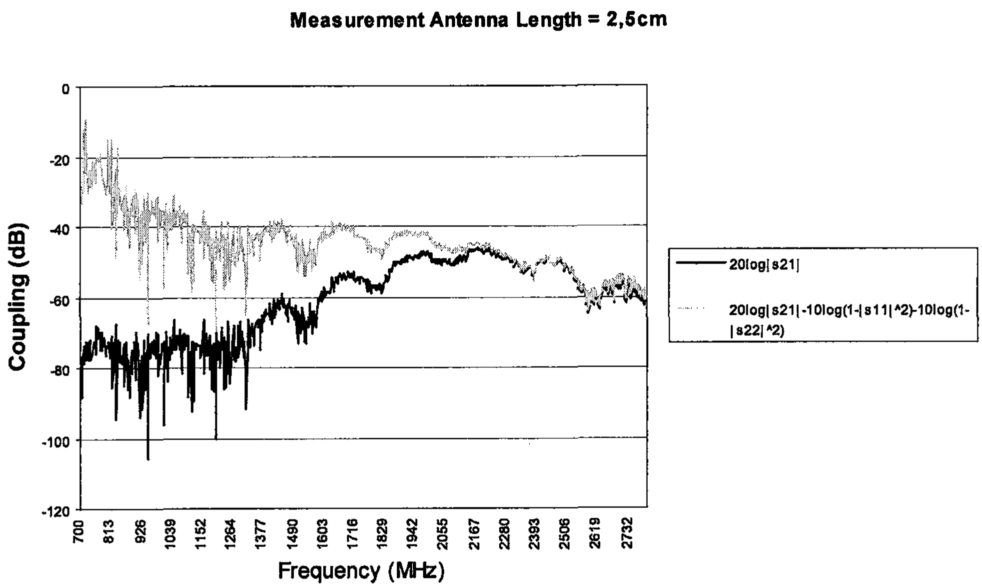

Figure 5.16: Coupling vs. frequency for antennas 6&5 with L=2,5cm.

In Figure 5.15, the mismatch loss in the 1,2-1,5 GHz region is close to zero. The sharp descent at the 900 MHz range is smilar to the one in figure 5.14. The mismatch loss increases after 1GHz and the measurements become inaccurate before 800 MHz and after 2,5 GHz range due to the mismatch errors at the antenna ports.

In Figure **5.16**, the mismatch loss in the 2,2-2,8 GHz region is close to zero. The mismatch loss increases before 1,9GHz and the measurements are inaccurate before 1,7 GHz due to the mismatch errors at the antenna ports.

Coupling values are generally under –20dB's except at a few frequencies shown in figure 5.16. The average coupling value without mismatch loss for (S_{21}) is –75.33 dB's and –64,33dB's when the mismatch losses are taken in to account.

5.5.2. Coupling between the antennas 6 and 3

The coupling w.r.t. frequency for antenna lengths of 10, 5 and 2,5 centimeters are given in the preceeding three figures respectively.

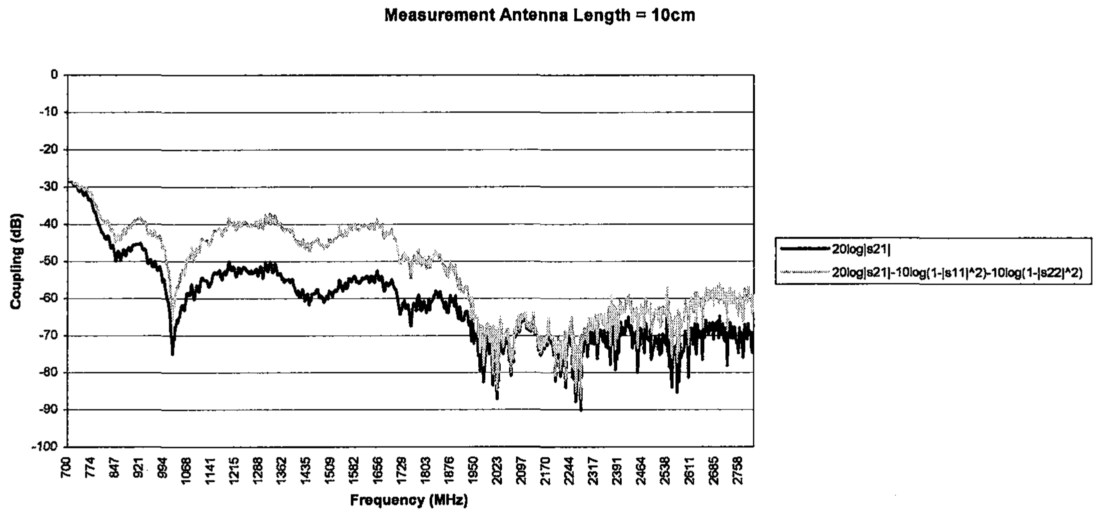

Figure 5.17: Coupling vs. frequency for antennas 6&3 with L=10cm.

In Figure 5.17, the mismatch loss in the 700-780 MHz region is close to zero. There is a sharp descent at the 970 MHz range. The measurements become inaccurate after 2,1 GHz range.

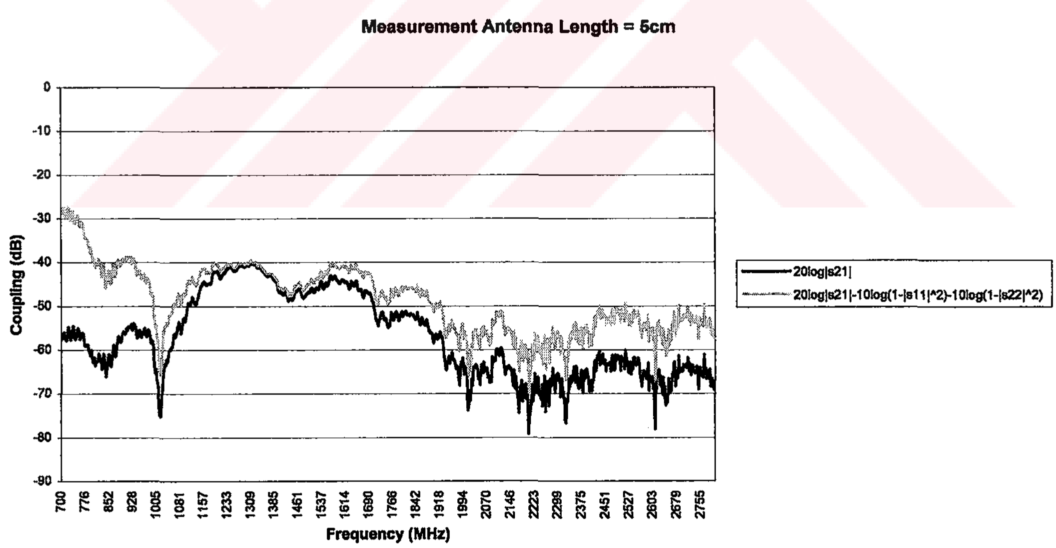

Figure 5.18: Coupling vs. frequency for antennas 6&3 with L=5cm.

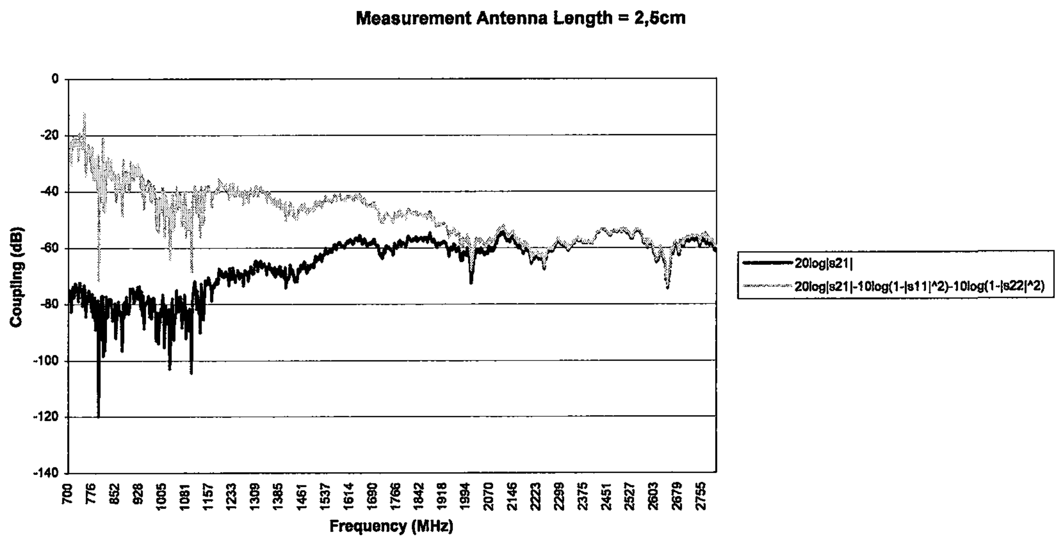

Figure 5.19: Coupling vs. frequency for antennas 6&3 with L=2,5cm.

In Figure 5.18, the mismatch loss in the 1,1-1,5 GHz region is close to zero. The sharp descent at the 970 MHz range is smilar to the one in figure 5.17. The mismatch loss increases after 1,9 GHz.

In Figure 5.19, the mismatch loss in the 2,4-2,8 GHz region is close to zero. The mismatch loss increases before 2,3 GHz.

Coupling values are generally under –25 dB's except at a few frequencies shown in figure 5.19. The average coupling value without mismatch error for (S_{21}) is –61 dB's and –49 dB's when the mismatch losses are taken into account.

5.5.3. Coupling between the antennas 6 and 1

The coupling w.r.t. frequency for antenna lengths of 10, 5 and 2,5 centimeters are given in the preceeding three figures respectively.

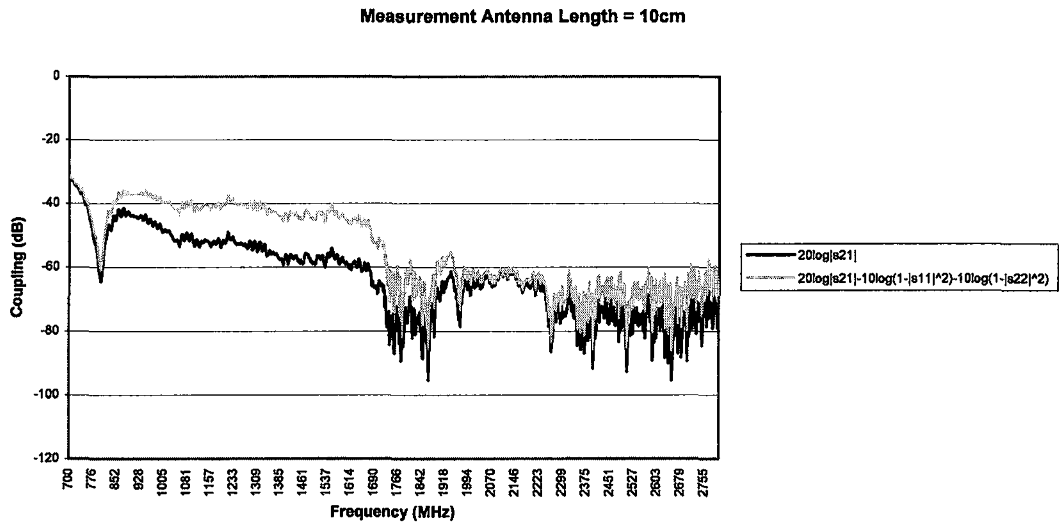

Figure 5.20: Coupling vs. frequency for antennas 6&1 with L=10cm.

In Figure 5.20, the mismatch loss in the 700-870 MHz region is close to zero. The measurements become inaccurate between the 1,6-1,9 GHz and after 2,3 GHz range.

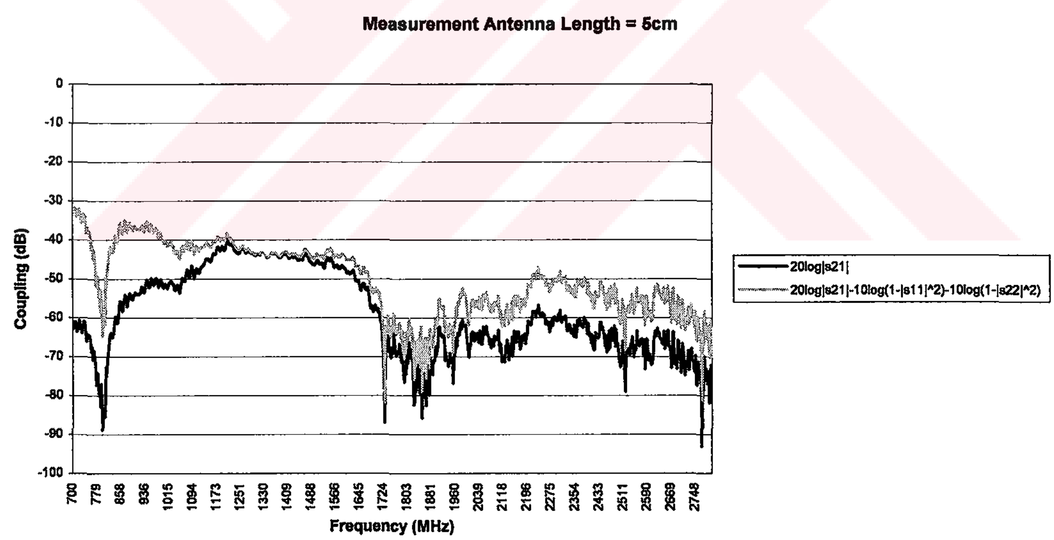

Figure 5.21: Coupling vs. frequency for antennas 6&1 with L=5cm.

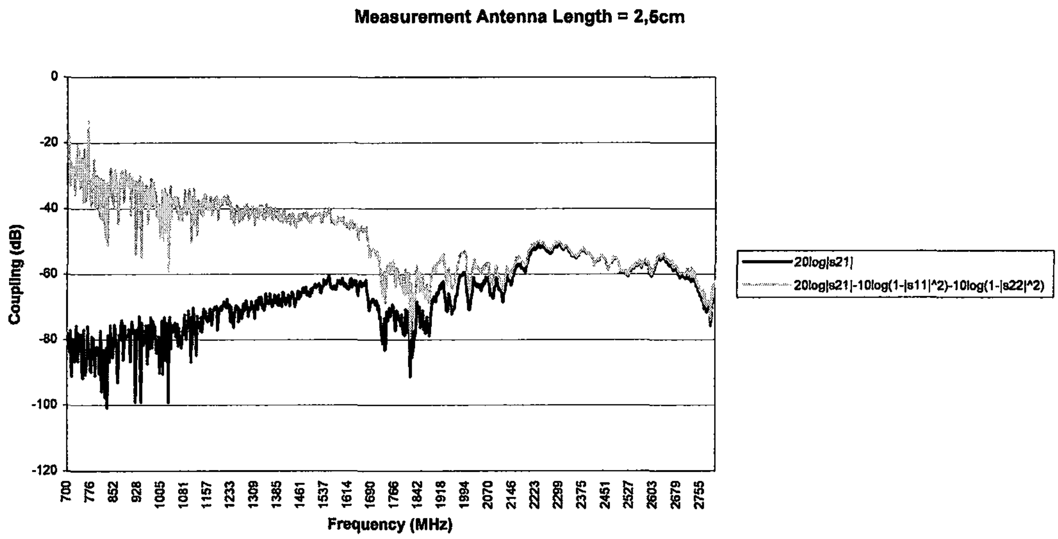

Figure 5.22: Coupling vs. frequency for antennas 6&1 with L=2,5cm.

In Figure 5.21, the mismatch loss in the 1,2-1,5 GHz region is close to zero. There is a sharp descent at the 790 MHz range. The mismatch loss increases after 2,3 GHz.

In Figure 5.22, the mismatch loss in the 2,1-2,8 GHz region is close to zero. The mismatch loss increases before 1,5 GHz.

Coupling values are generally under –20 dB's except at a few frequencies shown in figure 5.22 for these set of antennas. The average coupling value without mismatch loss for (S_{21}) is –61.3 dB's and –51 dB's when the mismatch losses are taken into account.

5.5.4. Coupling between the antennas 4 and 5

The coupling w.r.t. frequency for antenna lengths of 10, 5 and 2,5 centimeters are given in the preceeding three figures respectively.

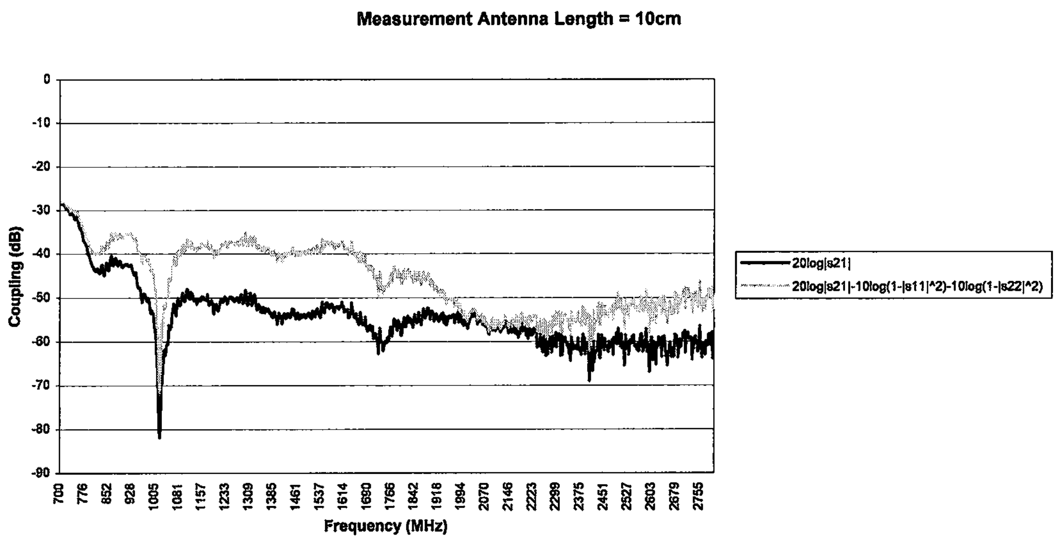

Figure 5.23: Coupling vs. frequency for antennas 4&5 with L=10cm.

In Figure 5.23, the mismatch loss in the 700-750 MHz region is close to zero. There is a sharp descent at the 1050 MHz range.

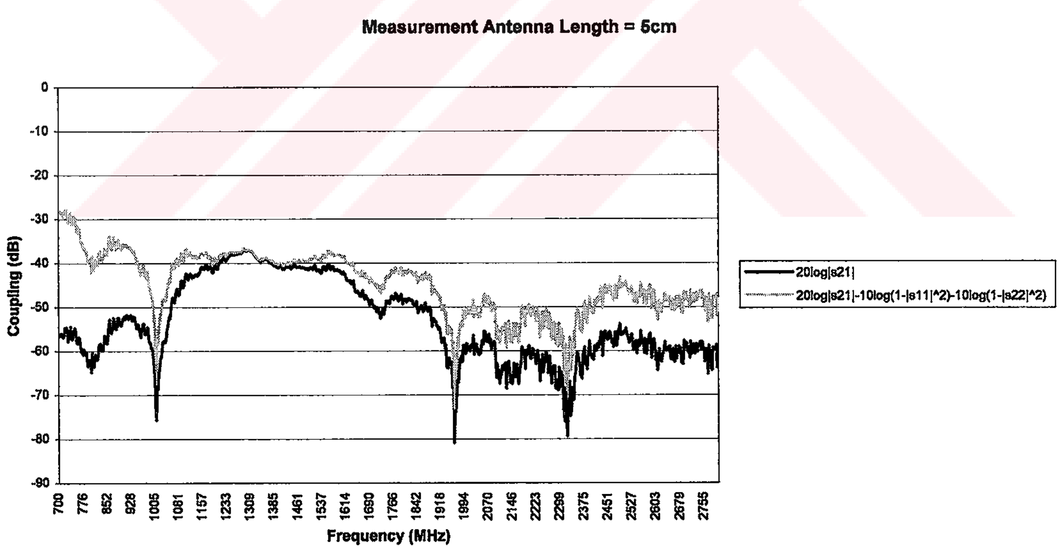

Figure 5.24: Coupling vs. frequency for antennas 4&5 with L=5cm.

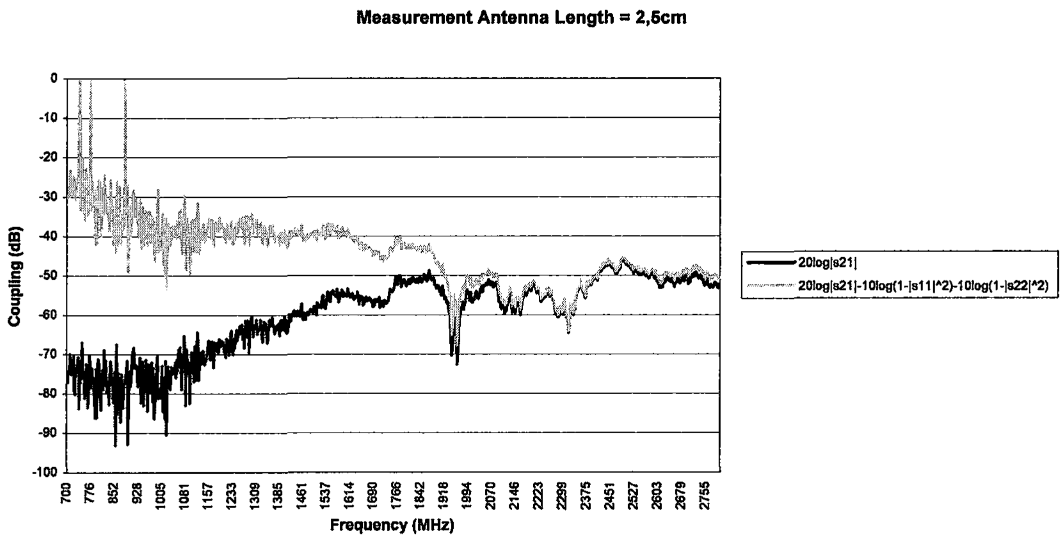

Figure 5.25: Coupling vs. frequency for antennas 4&5 with L=2,5cm.

In Figure 5.24, the mismatch loss in the 1,2-1,4 GHz region is close to zero. There is a sharp descents at the 1,015 and 1.96 GHz ranges. The mismatch loss increases after 2,065 GHz.

In Figure 5.25, the mismatch loss in the 2,050-2,8 GHz region is close to zero. The coupling increases to 0 dB's a number of times in the 700 – 800 MHz range which is bad for communication.

Coupling values are generally under –20 dB's except at a few frequencies shown in figure 5.25 for these set of antennas. The average coupling value without mismatch loss for (S_{21}) is –55 dB's and –44 dB's when the mismatch losses are taken into account.

5.5.5. Coupling between the antennas 4 and 3

The coupling w.r.t. frequency for antenna lengths of 10, 5 and 2,5 centimeters are given in the preceeding three figures respectively.

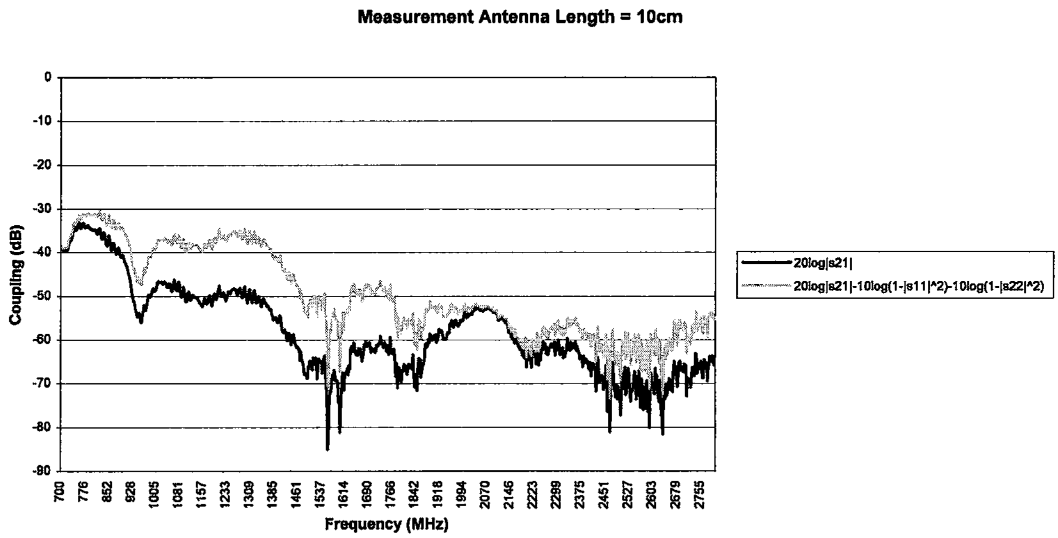

Figure 5.26: Coupling vs. frequency for antennas 4&3 with L=10cm.

In Figure 5.26, the mismatch loss in the 700-750 MHz and 2,0-2,1 GHz region is close to zero. The measurements become inaccurate after 2,1 GHz range.

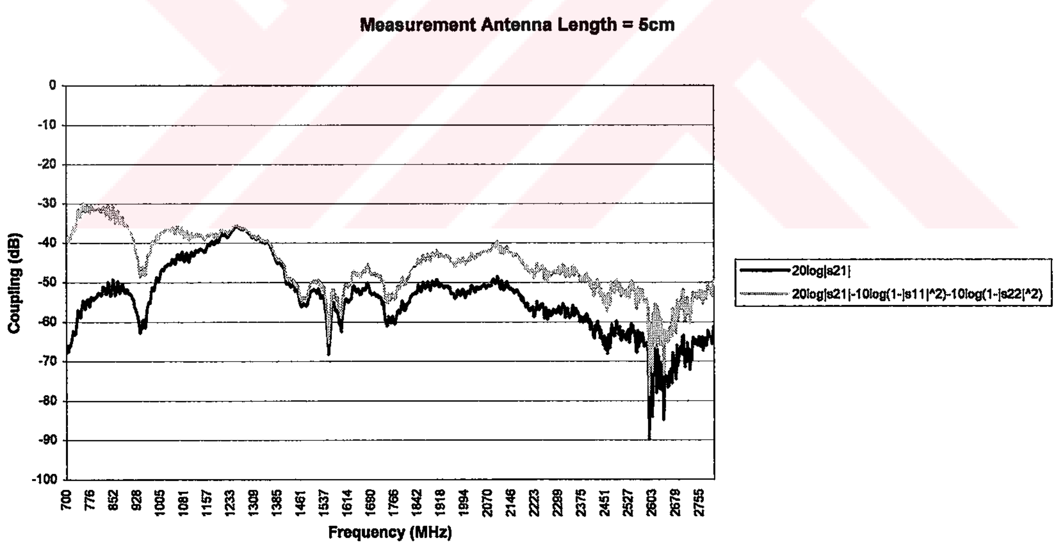

Figure 5.27: Coupling vs. frequency for antennas 4&3 with L=5cm.

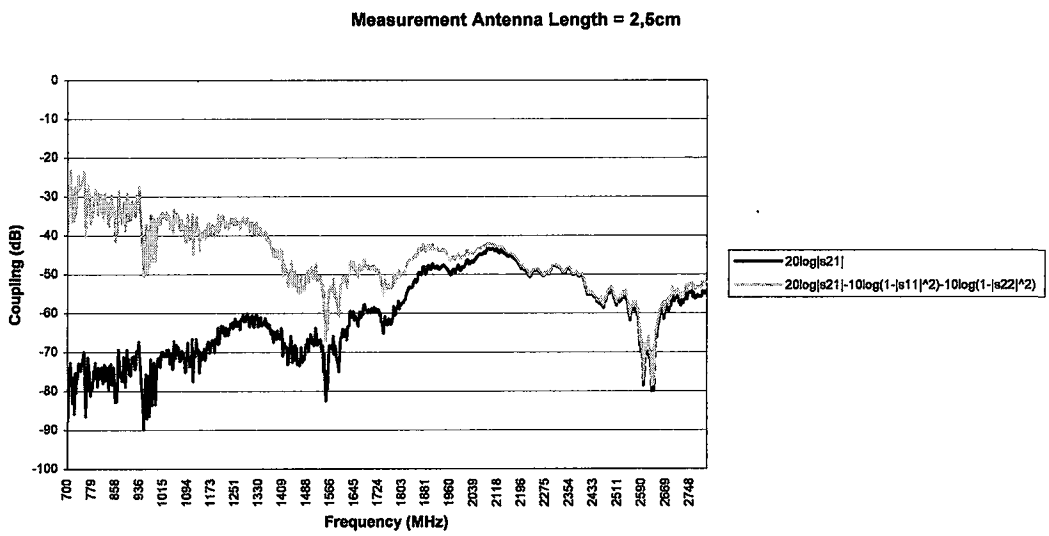

Figure 5.28: Coupling vs. frequency for antennas 4&3 with L=2,5cm.

In Figure 5.27, the mismatch loss in the 1,1-1,45 GHz region is close to zero. The mismatch loss increases before 1,05 and after 1,5 GHz.

In Figure 5.28, the mismatch loss in the 2,4-2,8 GHz region is close to zero. The mismatch loss increases after 2,1 GHz.

Coupling values are generally under –25 dB's except at a few frequencies shown in figure 5.28 for these set of antennas. The average coupling value without mismatch loss for (S_{21}) is –56 dB's and –46 dB's when the mismatch losses are taken into account.

5.5.6. Coupling between the antennas 4 and 1

The coupling w.r.t. frequency for antenna lengths of 10, 5 and 2,5 centimeters are given in the preceeding three figures respectively.

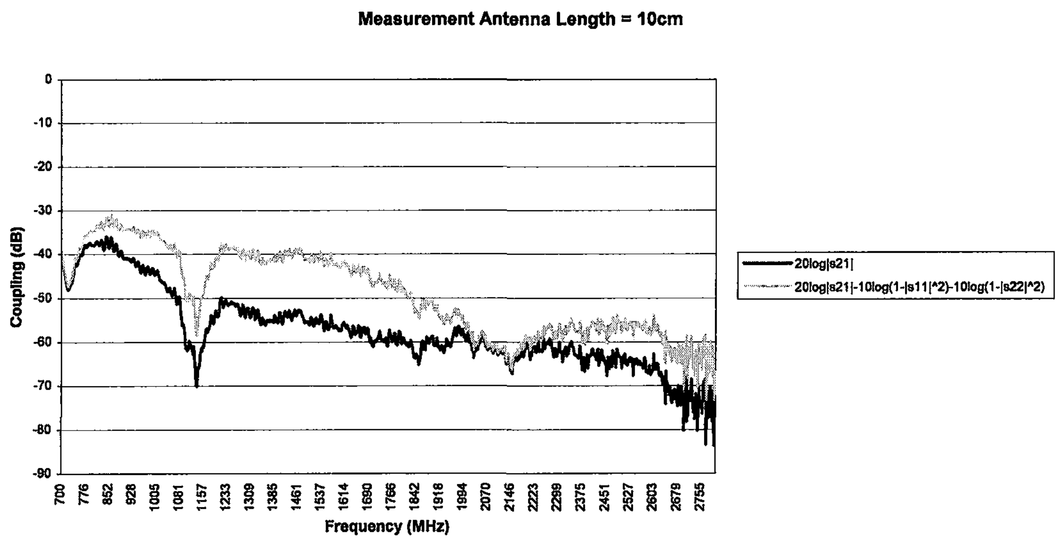

Figure 5.29: Coupling vs. frequency for antennas 4&1 with L=10cm.

In Figure 5.29, the mismatch loss in the 700-750 MHz and 2,0-2,1 GHz region is close to zero. The measurements become inaccurate after 2,1 GHz range.

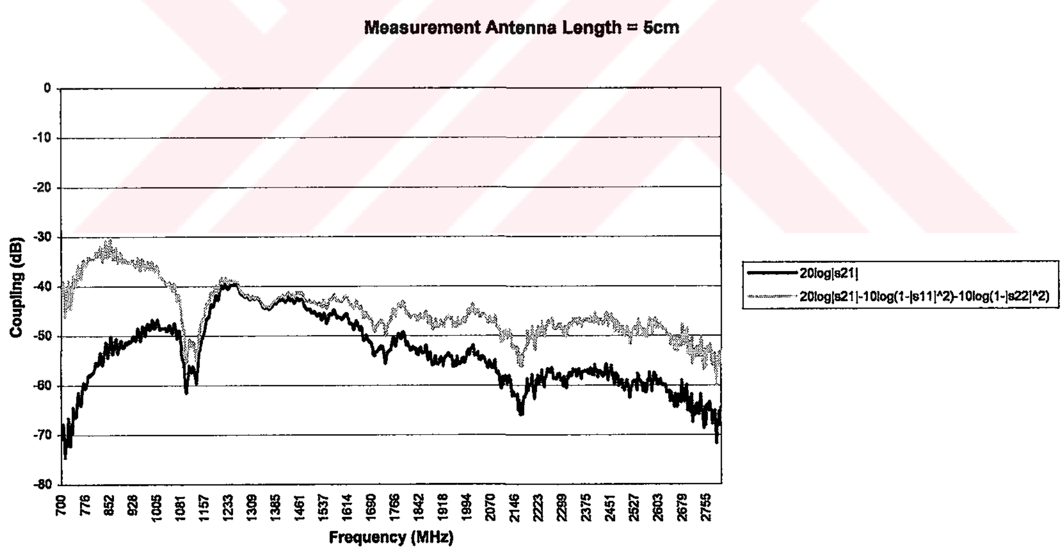

Figure 5.30: Coupling vs. frequency for antennas 4&1 with L=5cm.

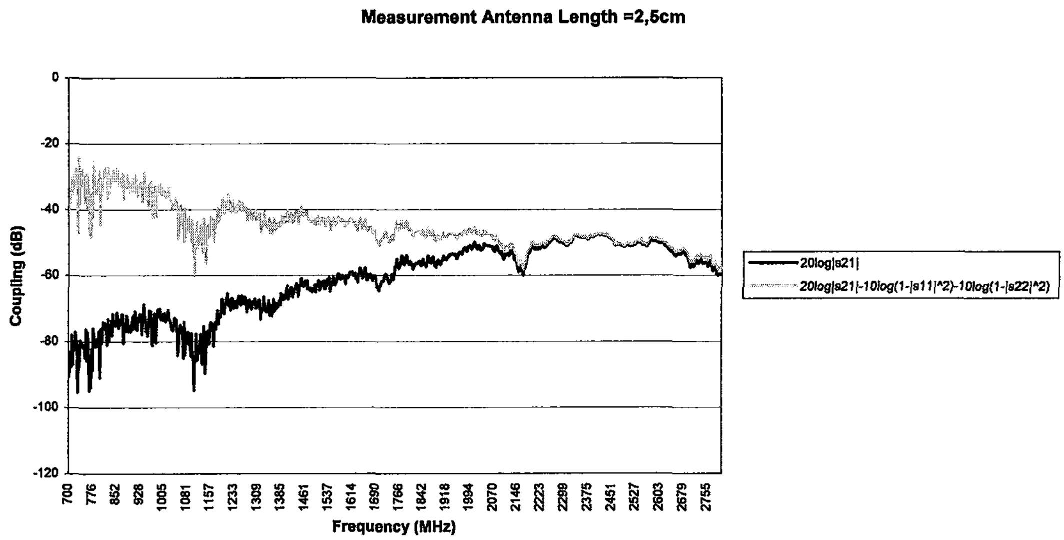

Figure 5.31: Coupling vs. frequency for antennas 4&1 with L=2,5cm.

In Figure 5.30, the mismatch loss in the 1,1-1,54 GHz region is close to zero.

In Figure 5.31, the mismatch loss in the 2,1-2,8 GHz region is close to zero. The mismatch loss increases after 2,1 GHz.

Coupling values are under –25 dB's for these set of antennas. The average coupling value without mismatch loss for (S_{21}) is –57 dB's and –46 dB's when the mismatch losses are taken into account.

5.5.7. Coupling between the antennas 2 and 5

The coupling w.r.t. frequency for antenna lengths of 10, 5 and 2,5 centimeters are given in the preceeding three figures respectively.

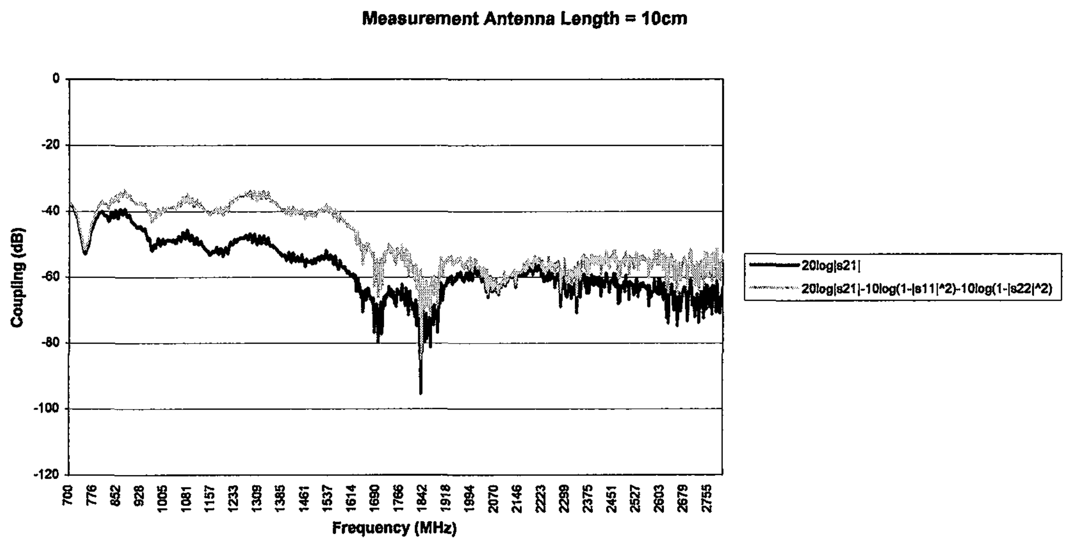

Figure 5.32: Coupling vs. frequency for antennas 2&5 with L=10cm.

In Figure 5.32, the mismatch loss in the 700-750 MHz and 1,9-2,1 GHz region is close to zero.

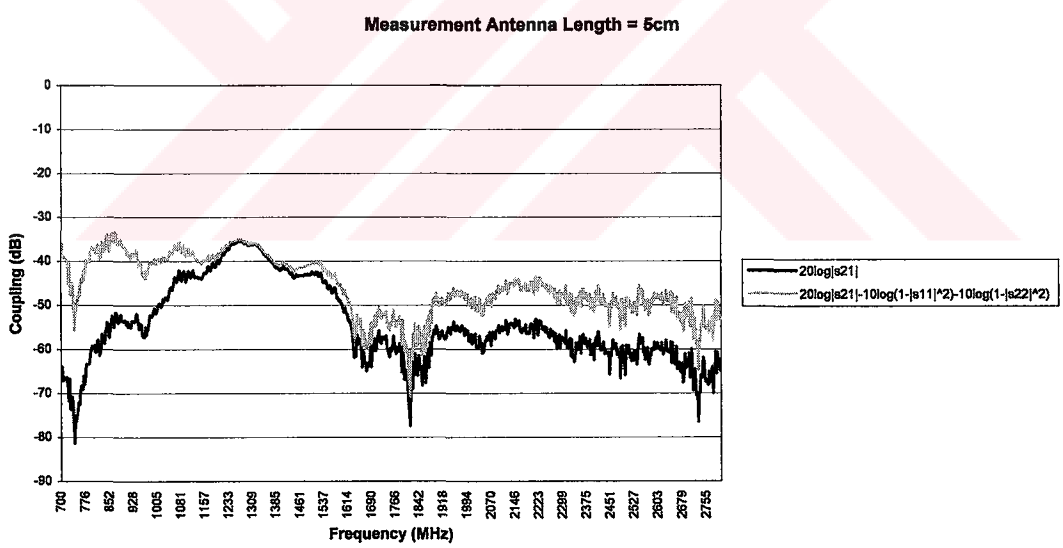

Figure 5.33: Coupling vs. frequency for antennas 2&5 with L=5cm.

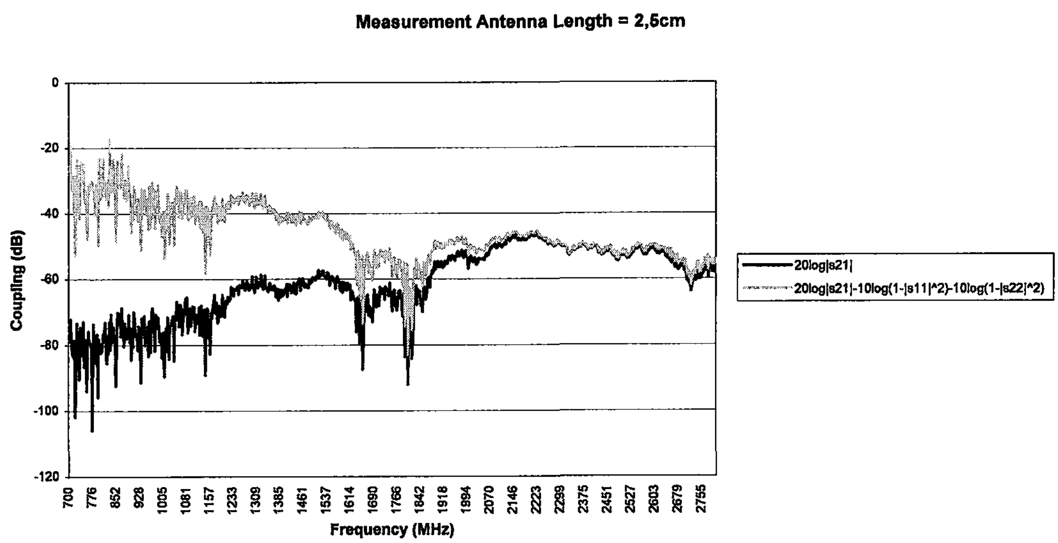

Figure 5.34: Coupling vs. frequency for antennas 2&5 with L=2,5cm.

In Figure 5.33, the mismatch loss in the 1,1-1,3 GHz region is close to zero.

In Figure 5.34, the mismatch loss in the 2,2-2,8 GHz region is close to zero. The mismatch loss increases after 2,1 GHz.

Coupling values are generally under –25 dB's except at a few frequencies shown in figure 5.34 for these set of antennas. The average coupling value without mismatch loss for (S_{21}) is –57 dB's and –46 dB's when the mismatch losses are taken into account.

5.5.8. Coupling between the antennas 2 and 3

The coupling w.r.t. frequency for antenna lengths of 10, 5 and 2,5 centimeters are given in the preceeding three figures respectively.

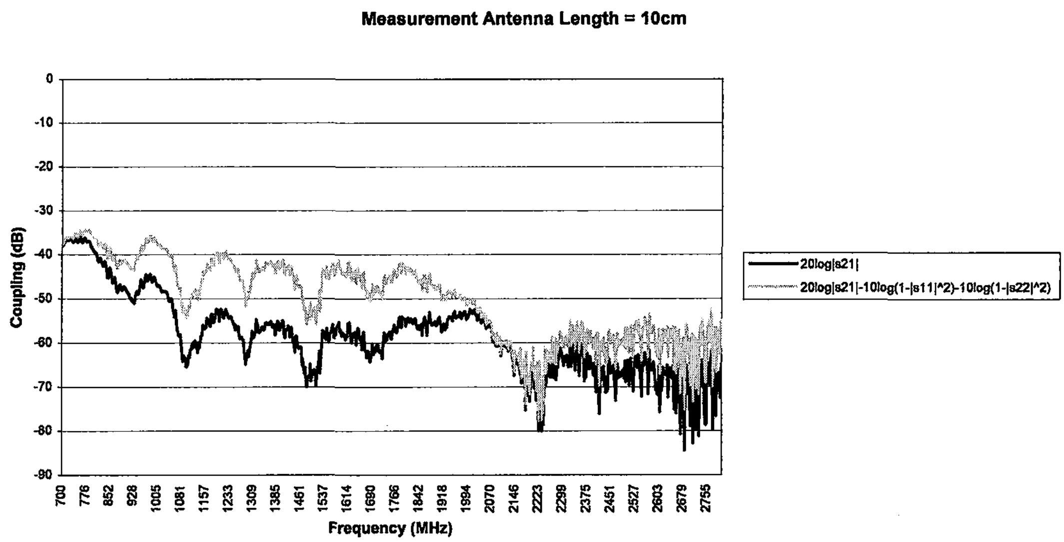

Figure 5.35: Coupling vs. frequency for antennas 2&3 with L=10cm.

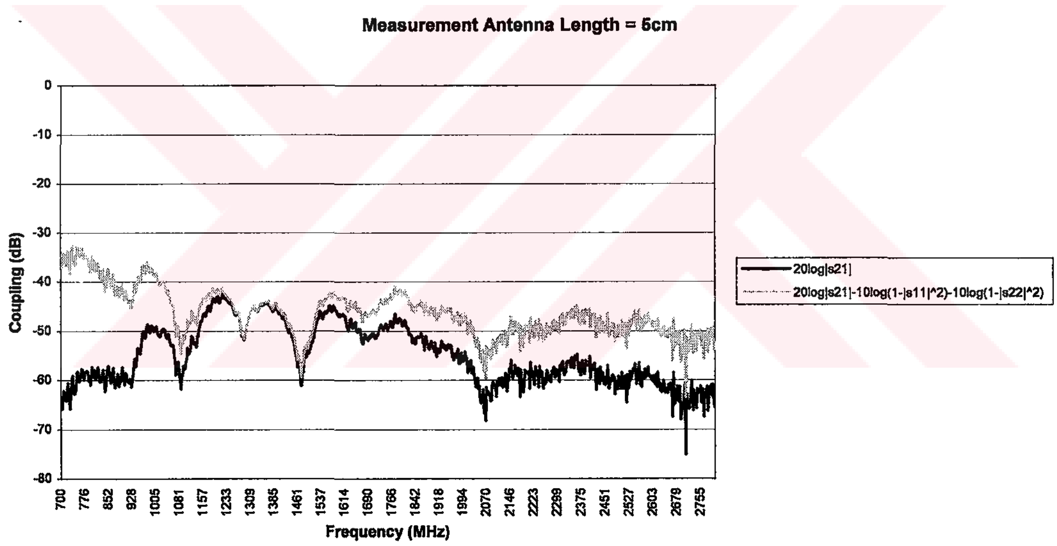

Figure 5.36: Coupling vs. frequency for antennas 2&3 with L=5cm.

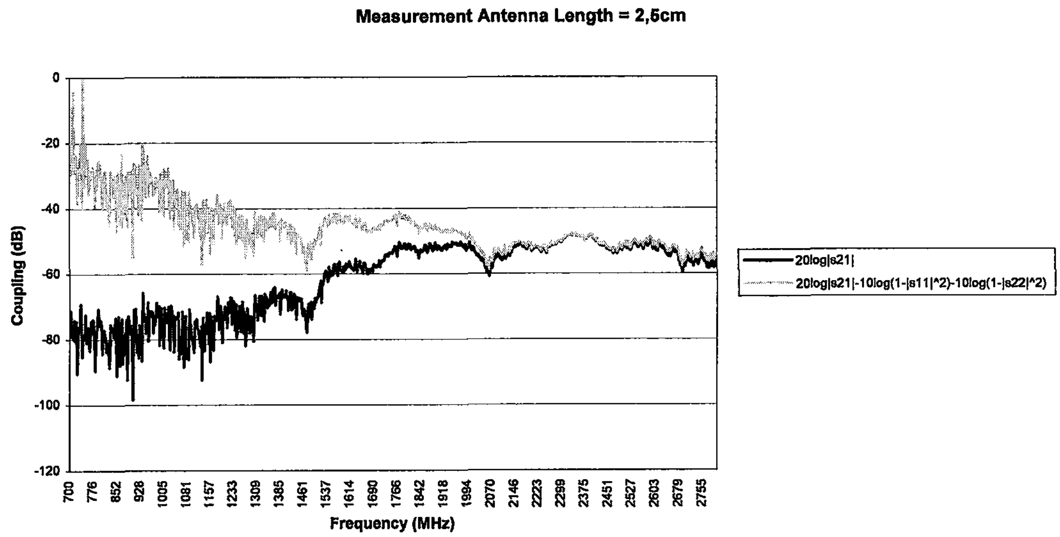

Figure 5.37: Coupling vs. frequency for antennas 2&3 with L=2,5cm.

In Figure 5.35, the mismatch loss in the 700-720 MHz is close to zero.

In Figure 5.36, the mismatch loss in the 1,2-1,5 GHz region is close to zero.

In Figure 5.37, the mismatch loss in the 2,0-2,8 GHz region is close to zero. The mismatch loss increases after 2,1 GHz. In the 700 MHz region, there are a number of 0dB couplings which is bad for communication.

Coupling values are generally under –25 dB's except at a few frequencies shown in figure 5.37 for these set of antennas. The average coupling value without mismatch loss for (S_{21}) is –56 dB's and –47 dB's when the mismatch losses are taken into account.

5.5.9. Coupling between the antennas 2 and 1

The coupling w.r.t. frequency for antenna lengths of 10, 5 and 2,5 centimeters are given in the preceeding three figures respectively.

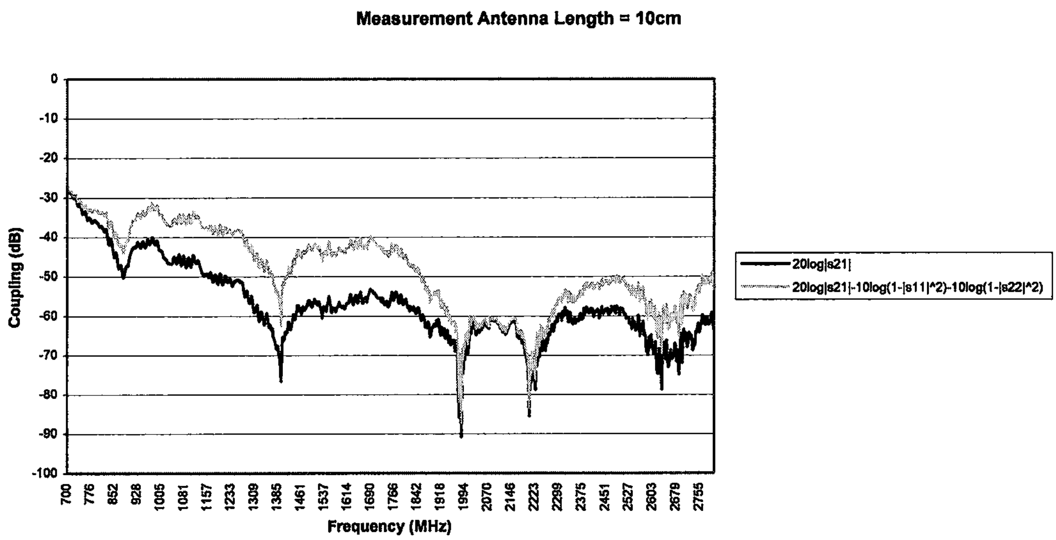

Figure 5.38: Coupling vs. frequency for antennas 2&1 with L=10cm.

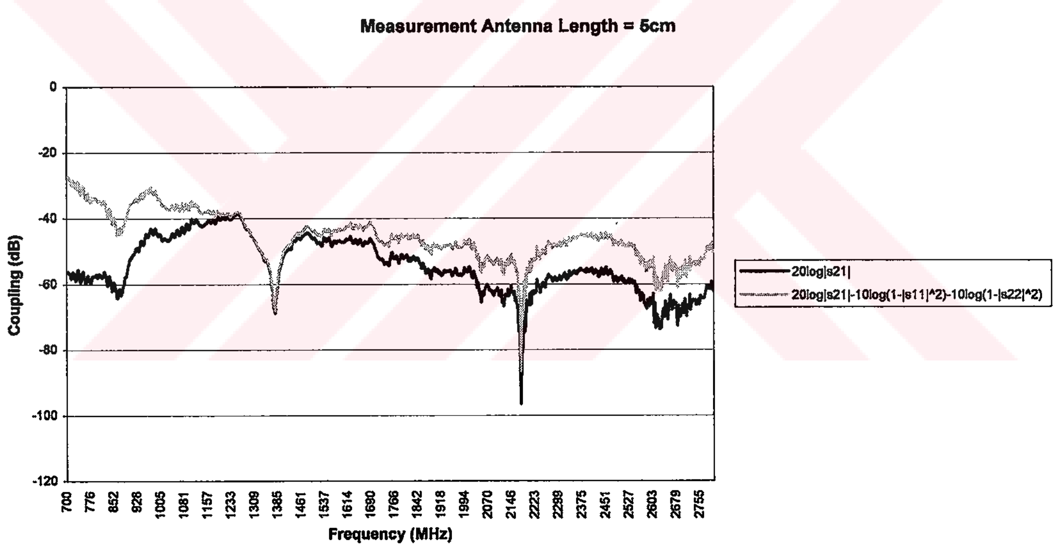

Figure 5.39: Coupling vs. frequency for antennas 2&1 with L=5cm.

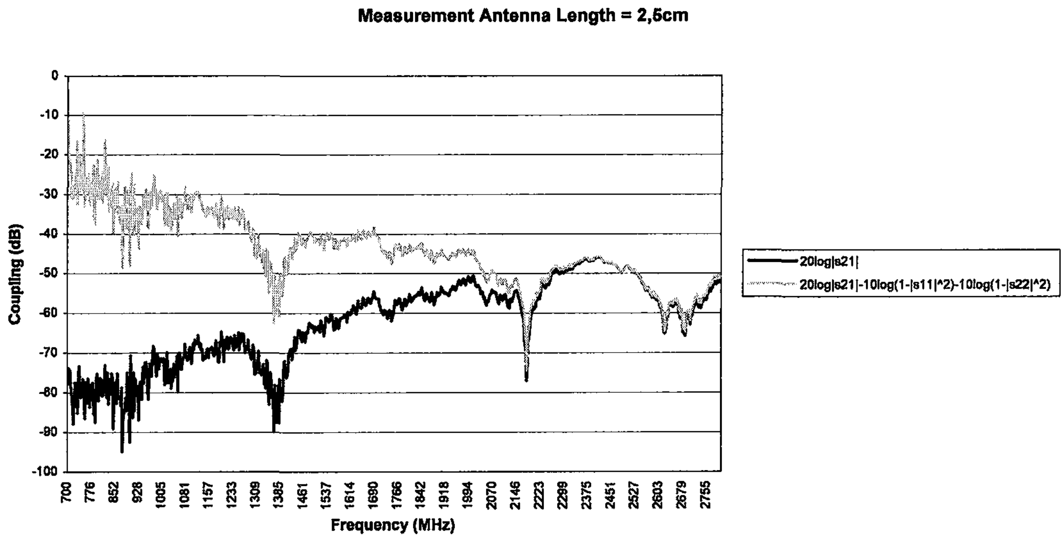

Figure 5.40: Coupling vs. frequency for antennas 2&1 with L=2,5cm.

In Figure 5.38, the mismatch loss in the 700-720 MHz region is close to zero. There are sharp descents between the 1,4 - 2,0 GHz.

In Figure 5.39, the mismatch loss in the 1,2-1,5 GHz region is close to zero. The sharp descents between the 1,35 - 2,2 GHz is smilar to the ones in figure 5.36.

In Figure 5.40, the mismatch loss in the 2,1-2,8 GHz region is close to zero. The mismatch loss increases before 2,15 GHz.

Coupling values are generally under –25 dB's except at a few frequencies shown in Figure 5.40 for these set of antennas. The average coupling value without mismatch loss for (S_{21}) is –57 dB's and –45 dB's when the mismatch losses are taken into account.

5.5.10. Coupling between the antennas 6 and 4

The coupling w.r.t. frequency for antenna lengths of 10, 5 and 2,5 centimeters are given in the preceeding three figures respectively.

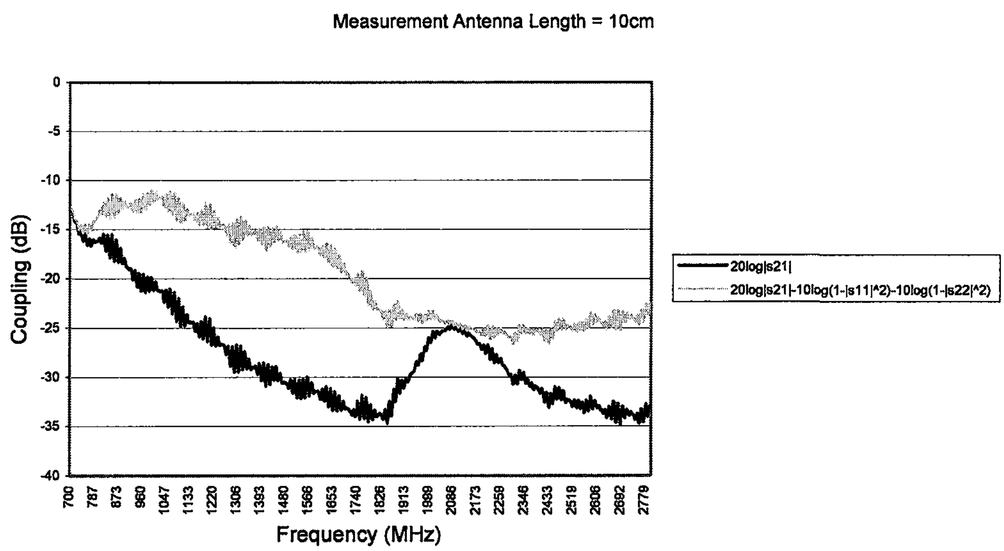

Figure 5.41: Coupling vs. frequency for antennas 6&4 with L=10cm.

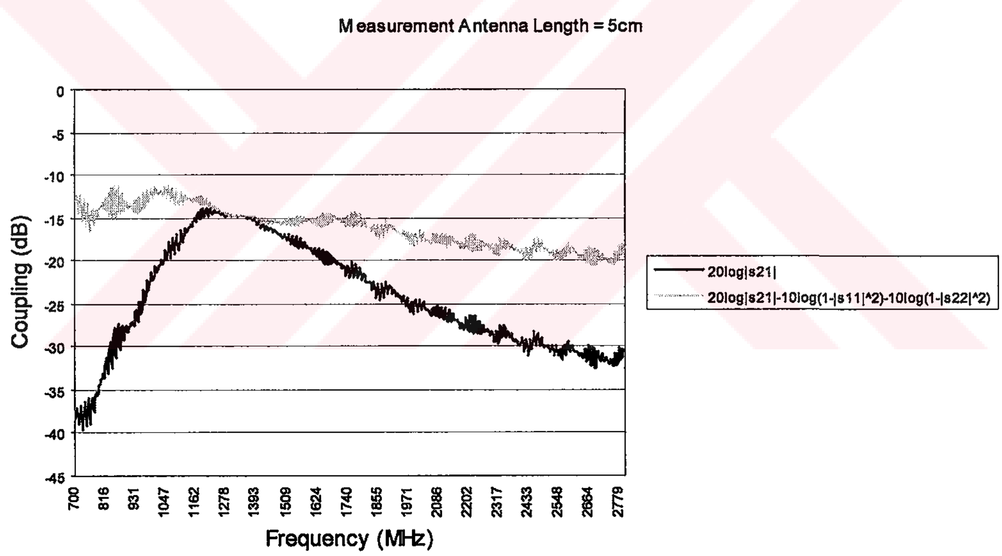

Figure 5.42: Coupling vs. frequency for antennas 6&4 with L=5cm.

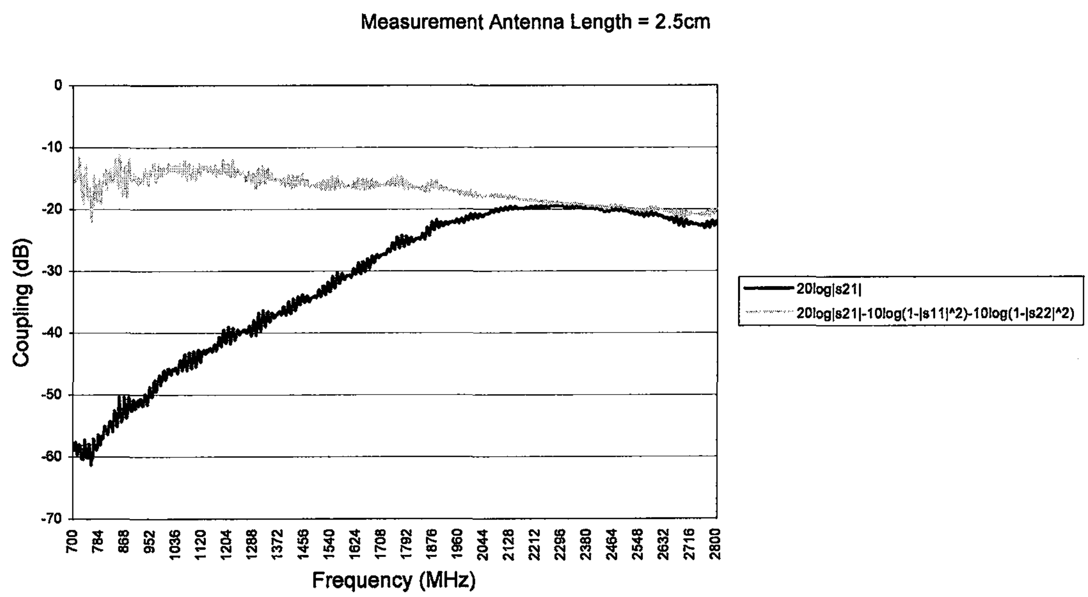

Figure 5.43: Coupling vs. frequency for antennas 6&4 with L=2,5cm.

In Figure **5.41**, the mismatch loss in the 700-720 MHz region is close to zero. The coupling values are relatively very higher when compared with the previous antenna positions.

In Figure 5.42, the mismatch loss in the 1,2-1,25 GHz region is close to zero.

In Figure 5.43, the mismatch loss in the 2,1-2,8 GHz region is close to zero. The mismatch loss increases dramatically before 1,5 GHz.

Coupling values are under –10 dB's for these set of antennas. The average coupling value without mismatch loss for S_{21} is –27 dB's and –18 dB's when the mismatch losses are taken in to account.

5.5.11. Coupling between the antennas 6 and 2

The coupling w.r.t. frequency for antenna lengths of 10, 5 and 2,5 centimeters are given in the preceeding three figures respectively.

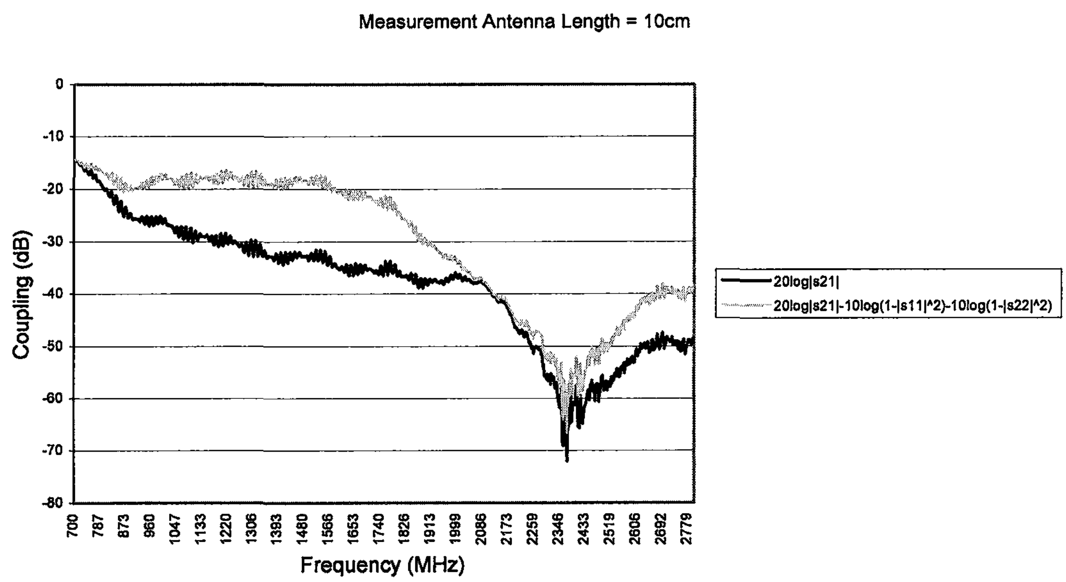

Figure 5.44: Coupling vs. frequency for antennas 6&2 with L=10cm.

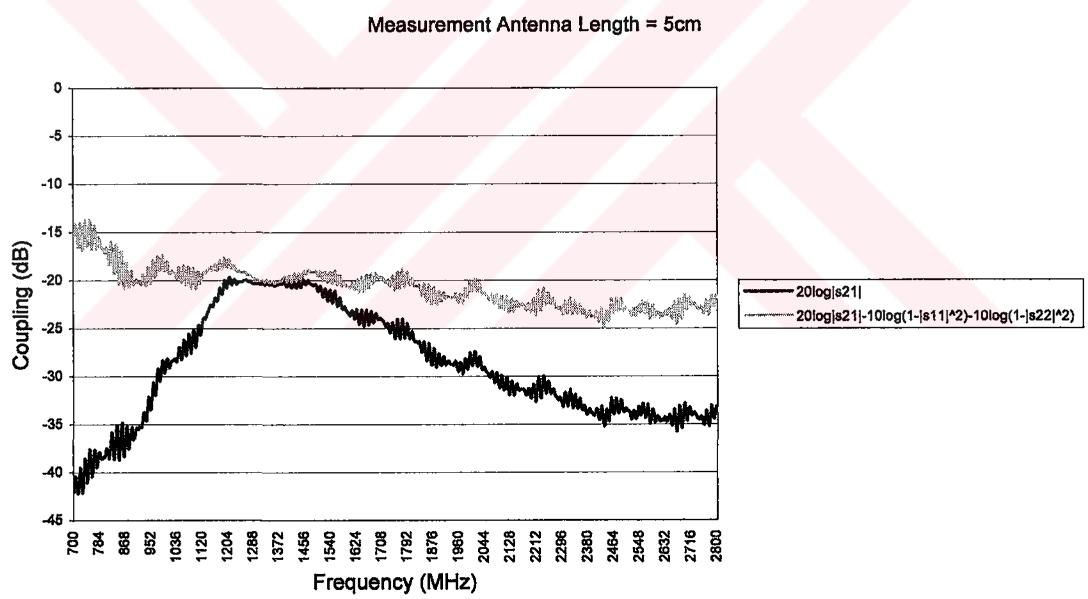

Figure 5.45: Coupling vs. frequency for antennas 6&2 with L=5cm.

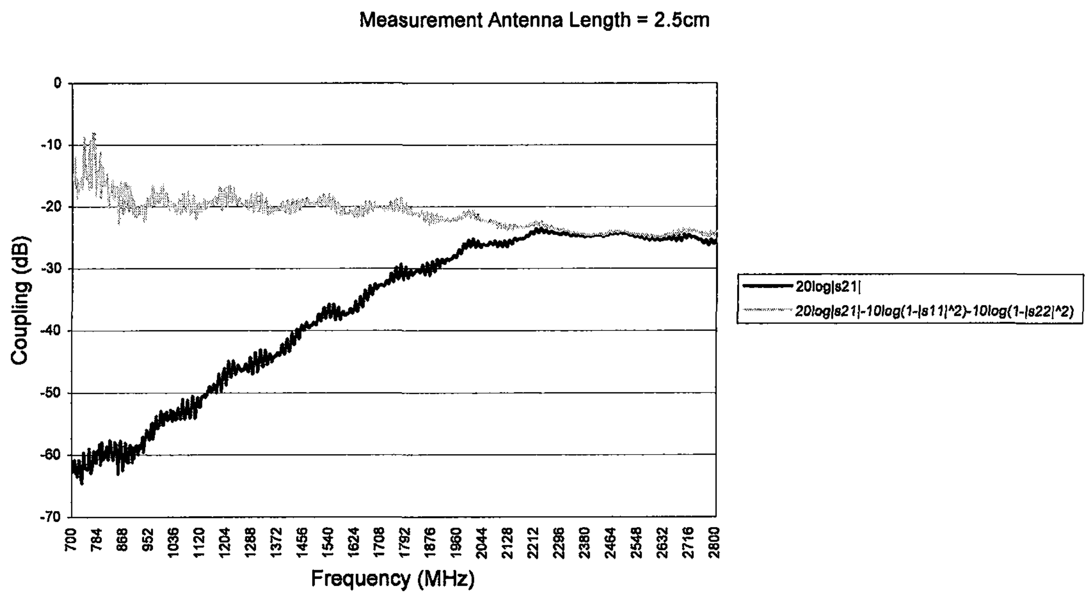

Figure 5.46: Coupling vs. frequency for antennas 6&2 with L=2,5cm.

In Figure 5.44, the mismatch loss in the 700-750 MHz region is close to zero. There is a sharp descent at 2300 MHz.

In Figure 5.45, the mismatch loss in the 1,2-1,5 GHz region is close to zero.

In Figure 5.46, the mismatch loss in the 2,15-2,8 GHz region is close to zero.

Coupling values are under –10 dB's for these set of antennas. The average coupling value without mismatch loss for S_{21} is –35 dB's and –24 dB's when the mismatch losses are taken in to account.

5.5.12. Coupling between the antennas 4 and 2

The coupling w.r.t. frequency for antenna lengths of 10, 5 and 2,5 centimeters are given in the preceeding three figures respectively.

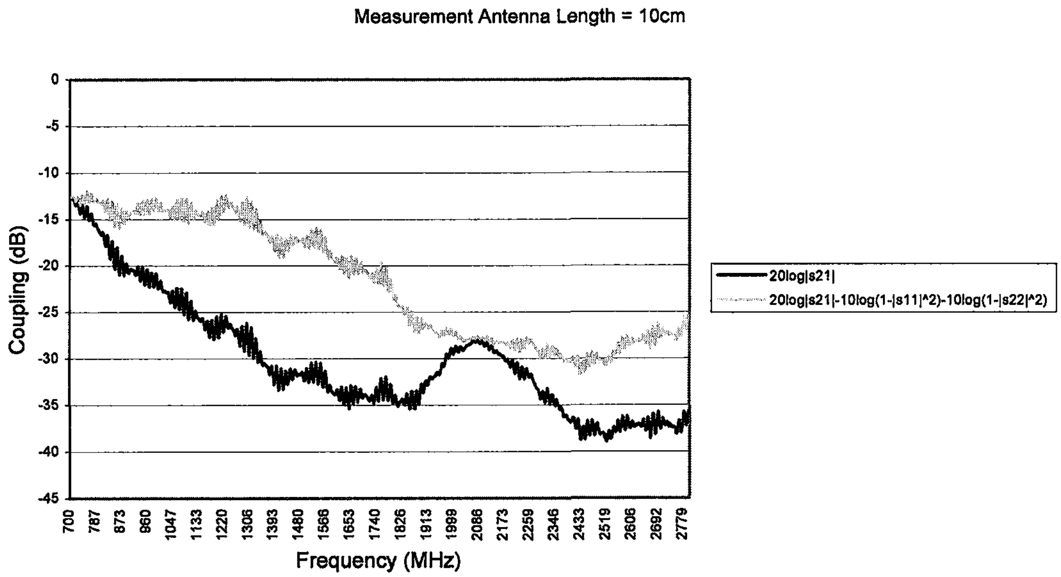

Figure 5.47: Coupling vs. frequency for antennas 4&2 with L=10cm.

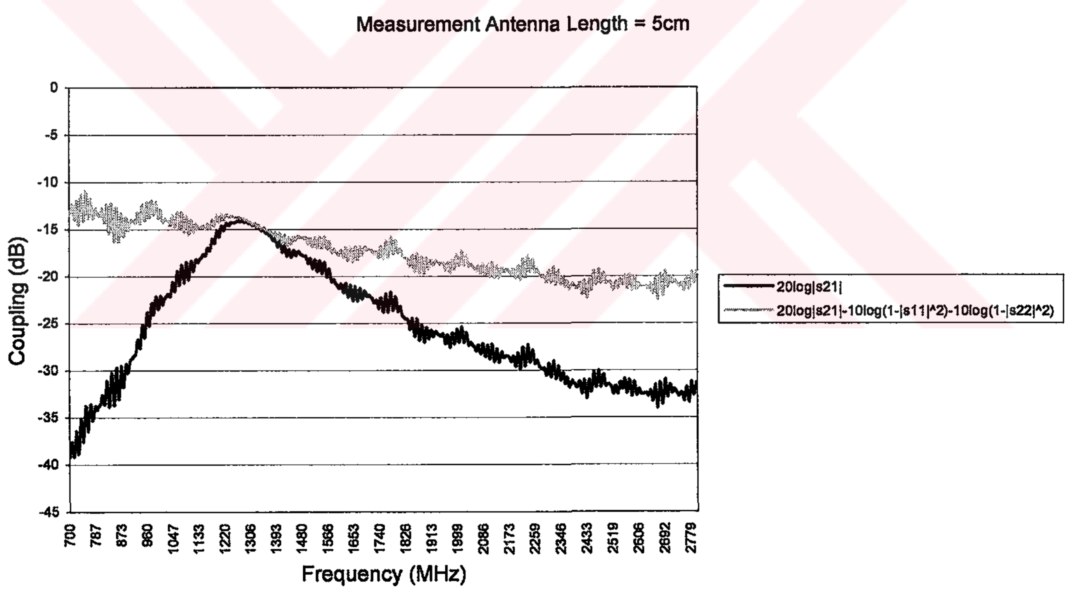

Figure 5.48: Coupling vs. frequency for antennas 4&2 with L=5cm.

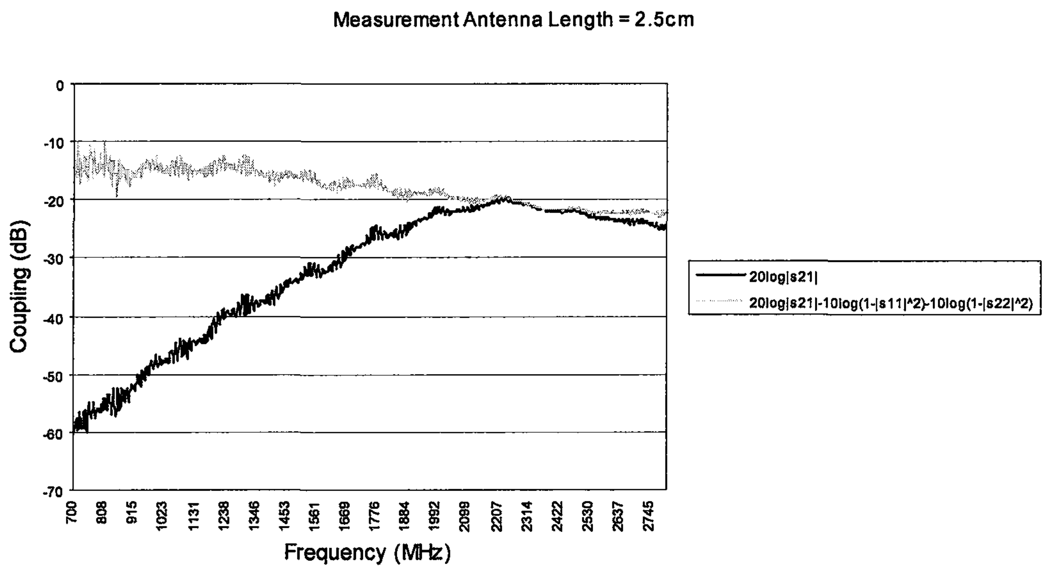

Figure 5.49: Coupling vs. frequency for antennas 4&2 with L=2,5cm.

In Figure 5.47, the mismatch loss in the 700 MHz region is close to zero. The measurements become inaccurate after this range.

In Figure 5.48, the mismatch loss in the 1,2-1,3 GHz region is close to zero. The mismatch loss increases before and after this range.

In Figure 5.49, the mismatch loss in the 2,2-2,6 GHz region is close to zero. The diference from the other measurements is that the the mismatch loss.

Coupling values are under –10 dB's for these set of antennas. The average coupling value without mismatch loss for S_{21} is –29 dB's and –19 dB's when the mismatch losses are taken into account.

5.5.13. Coupling between the antennas 5 and 3

The coupling w.r.t. frequency for antenna lengths of 10, 5 and 2,5 centimeters are given in the preceeding three figures respectively.

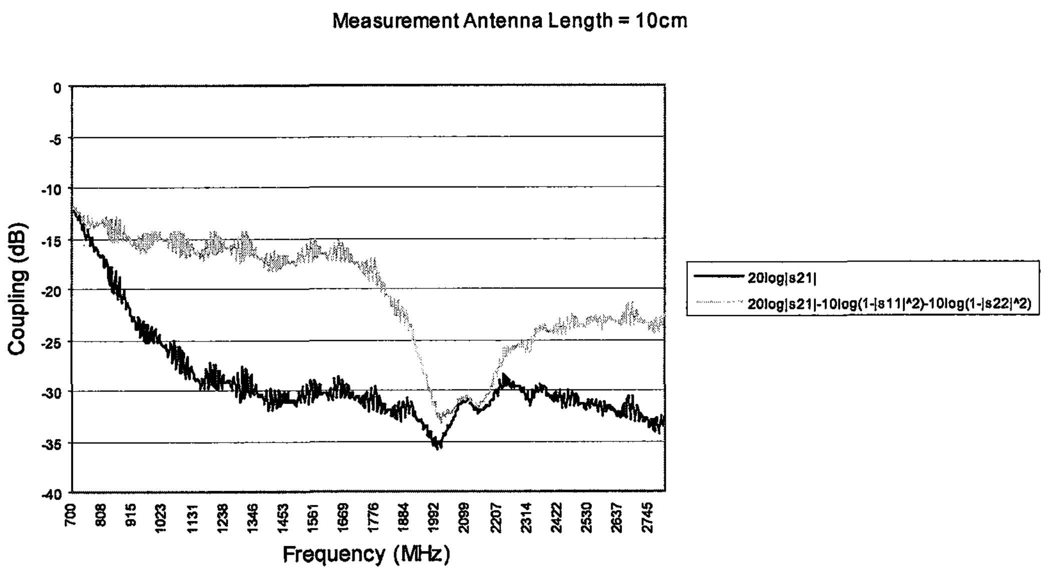

Figure 5.50: Coupling vs. frequency for antennas 5&3 with L=10cm.

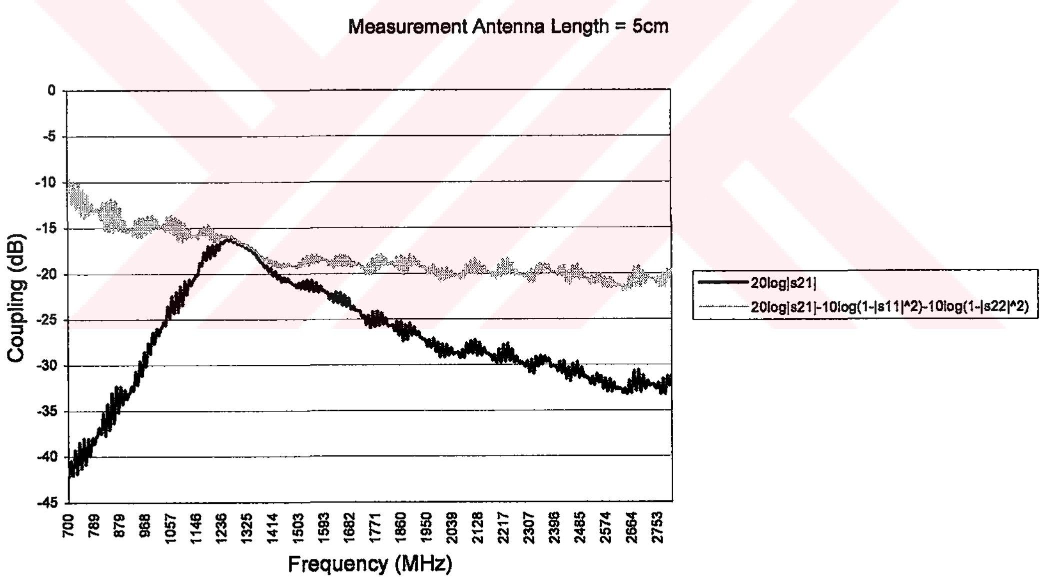

Figure 5.51: Coupling vs. frequency for antennas 5&3 with L=5cm.

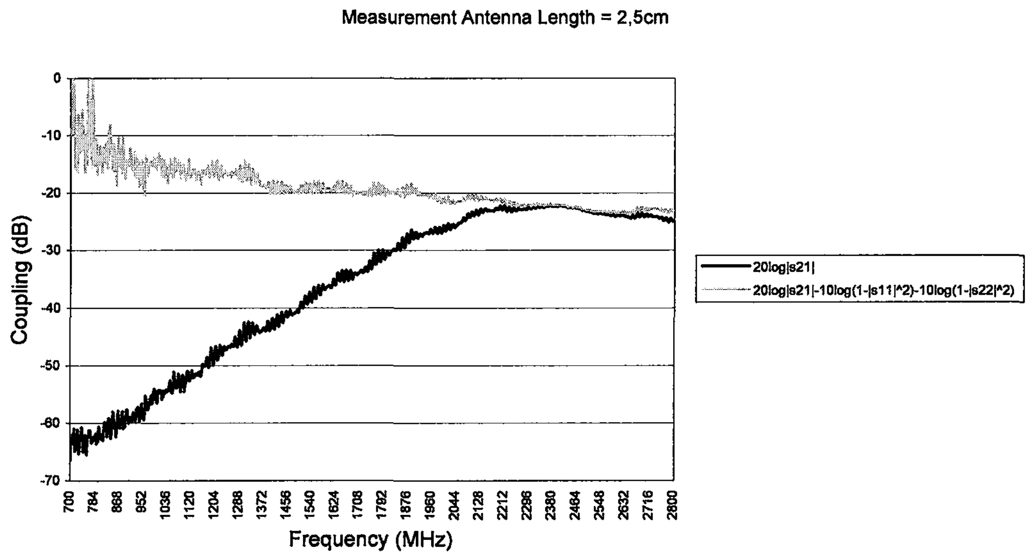

Figure 5.52: Coupling vs. frequency for antennas 5&3 with L=2,5cm.

In Figure 5.50, the mismatch loss in the 700MHz and 2,0-2,1 GHz region is close to zero.

In Figure 5.51, the mismatch loss in the 1,1-1,45 GHz region is close to zero. The mismatch loss increases dramatically on other regions.

In Figure **5.52**, the mismatch loss in the 2,2-2,5 GHz region is close to zero. The mismatch loss slightly increases after 2,6 GHz.

The average coupling value without mismatch loss S_{21} is –31 dB's and –19 dB's when the mismatch losses are taken in to account.

5.5.14. Coupling between the antennas 5 and 1

The coupling w.r.t. frequency for antenna lengths of 10, 5 and 2,5 centimeters are given in the preceeding three figures respectively.

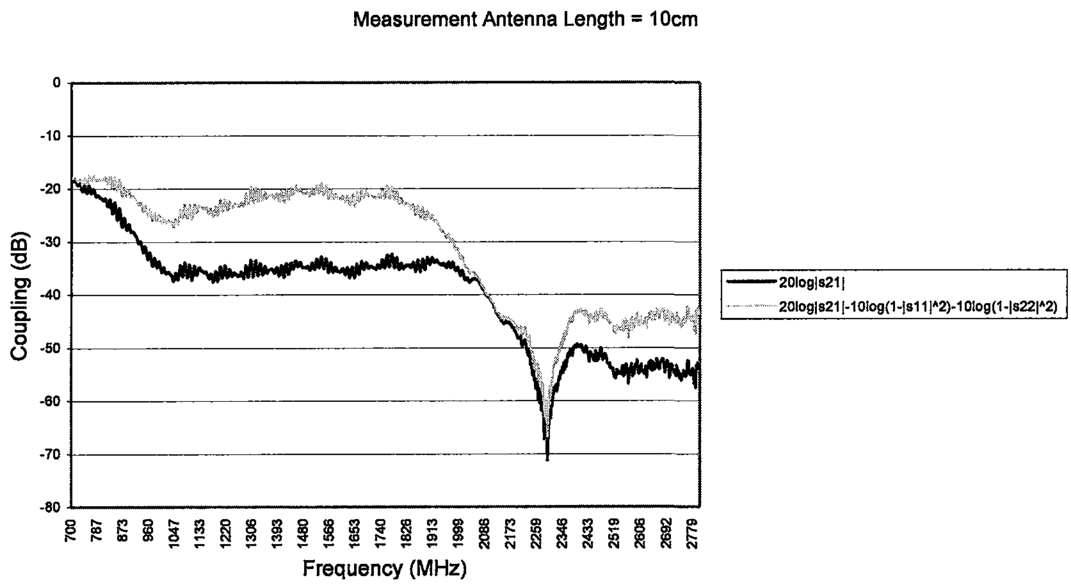

Figure 5.53: Coupling vs. frequency for antennas 5&1 with L=10cm.

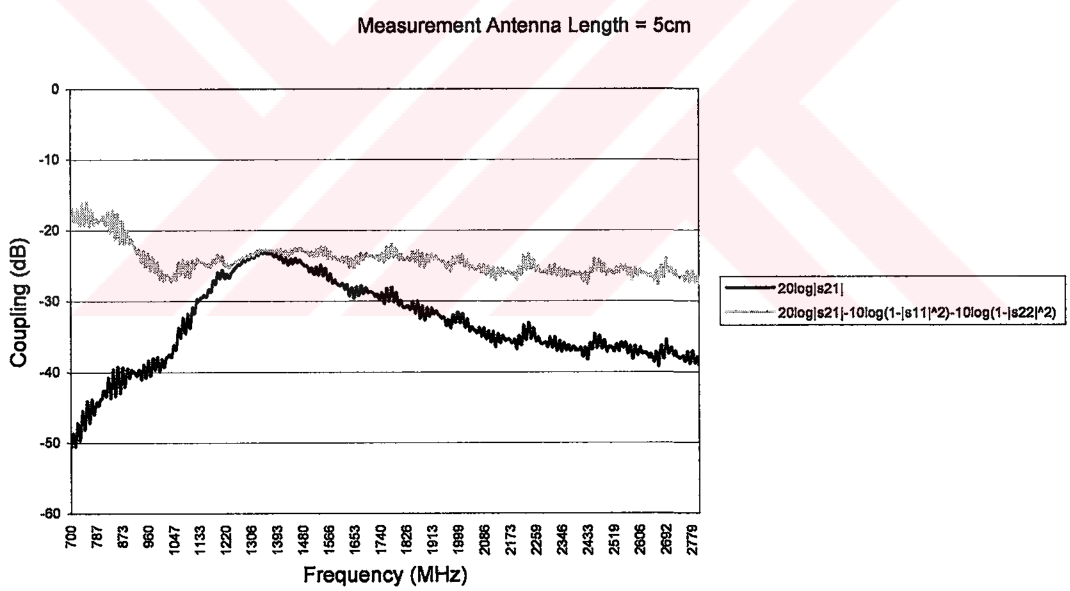

Figure 5.54: Coupling vs. frequency for antennas 5&1 with L=5cm.

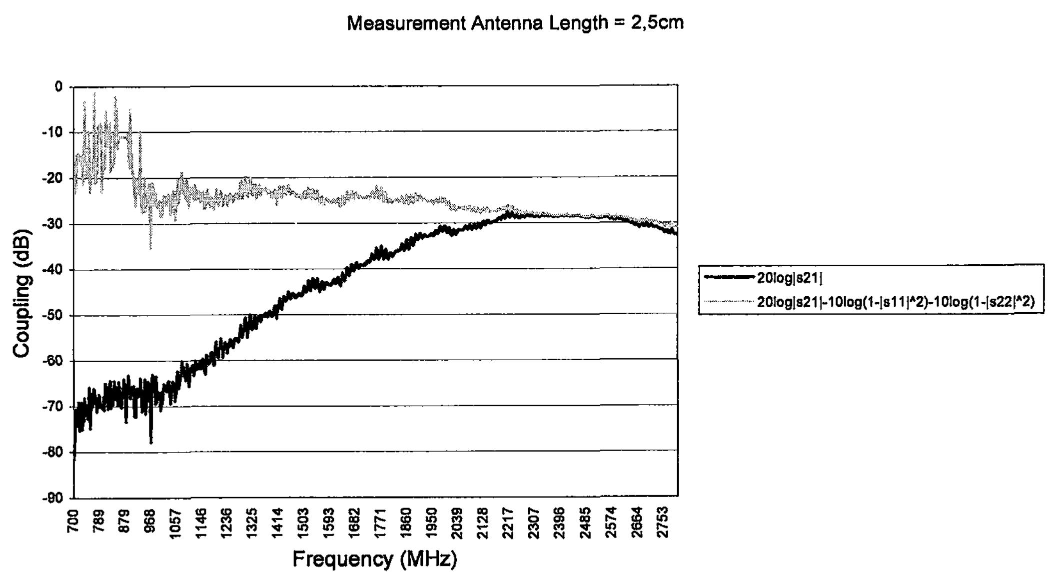

Figure 5.55: Coupling vs. frequency for antennas 5&1 with L=2,5cm.

In Figure 5.53, the mismatch loss in the 700 MHz and 2,0-2,3 GHz region is close to zero.

In Figure 5.54, the mismatch loss in the 1,3-1,45 GHz region is close to zero.

In Figure 5.55, the mismatch loss in the 2,3-2,8 GHz region is close to zero. The mismatch loss increases after 2,1 GHz. Also there are 0 dB coupling levels in the 700-900 MHz region which is bad for communication

The average coupling value without mismatch loss (S_{21}) is –39 dB's and –27 dB's when the mismatch losses are taken in to account.

5.5.15. Coupling between the antennas 3 and 1

The coupling w.r.t. frequency for antenna lengths of 10, 5 and 2,5 centimeters are given in the preceeding three figures respectively.

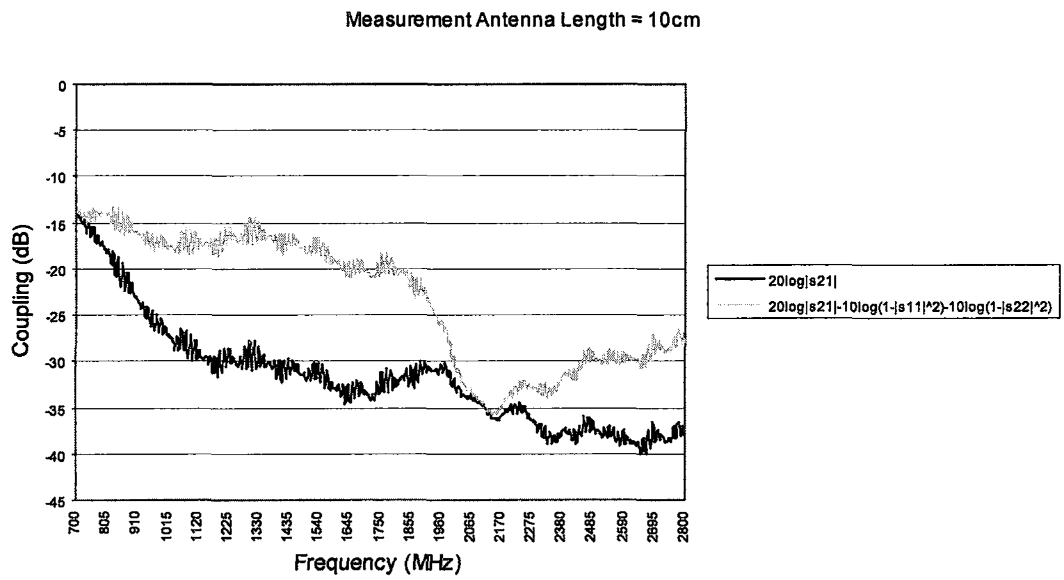

Figure 5.56: Coupling vs. frequency for antennas 3&1 with L=10cm.

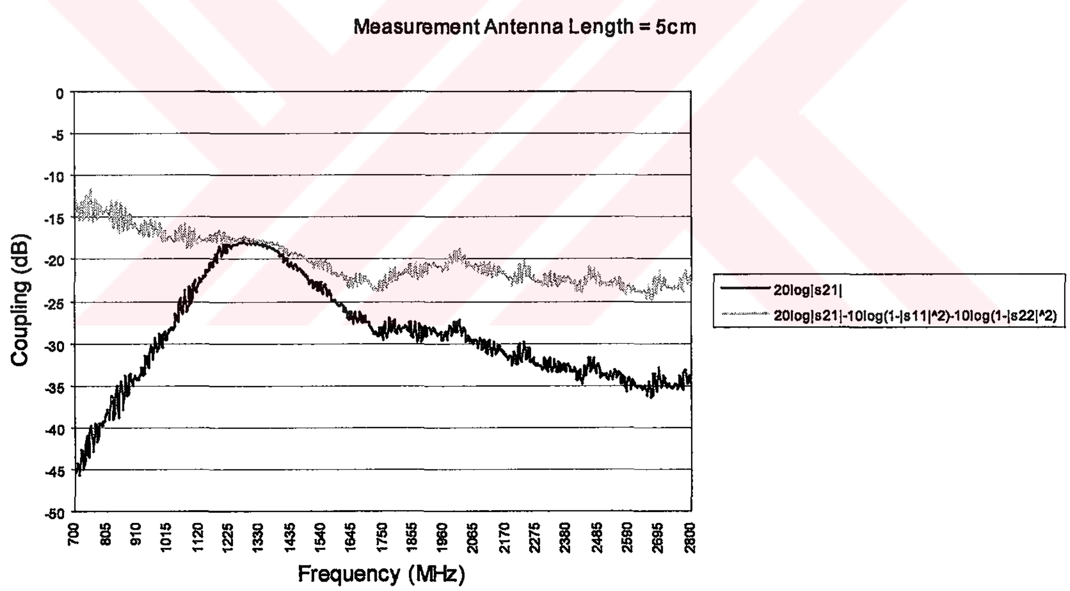

Figure 5.57: Coupling vs. frequency for antennas 3&1 with L=5cm.

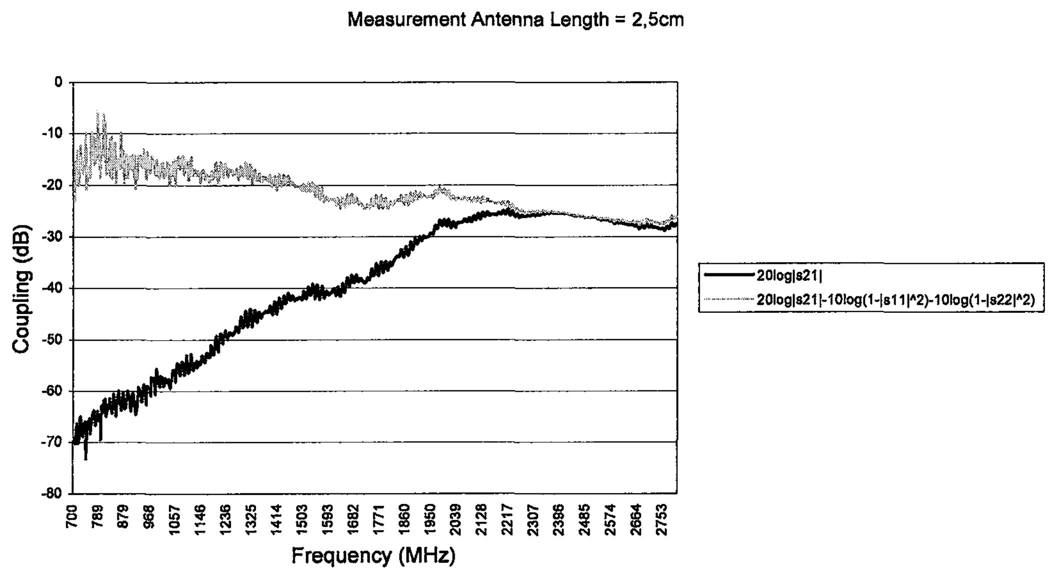

Figure 5.58: Coupling vs. frequency for antennas 3&1 with L=2,5cm.

In Figure 5.56, the mismatch loss in the 700 MHz and 2,0-2,2 GHz is close to zero.

In Figure 5.57, the mismatch loss in the 1,2-1,45 GHz region is close to zero.

In Figure 5.58, the mismatch loss in the 2,3-2,8 GHz region is close to zero. In the 800-900 MHz region, there are a number of –5 dB couplings which is bad for communication.

The average coupling value without mismatch loss (S_{21}) is –32 dB's and –21 dB's when the mismatch losses are taken in to account.

In the next section, the measurement results will be compared with each other and the numerical analysis results.

6. EVALUATION AND DISCUSSIONS

The results at the measurements section are evaluated by their averaged values. In Figure 6.1 and Figure 6.2 the average coupling with mismatch loss is plotted for various antenna locations.

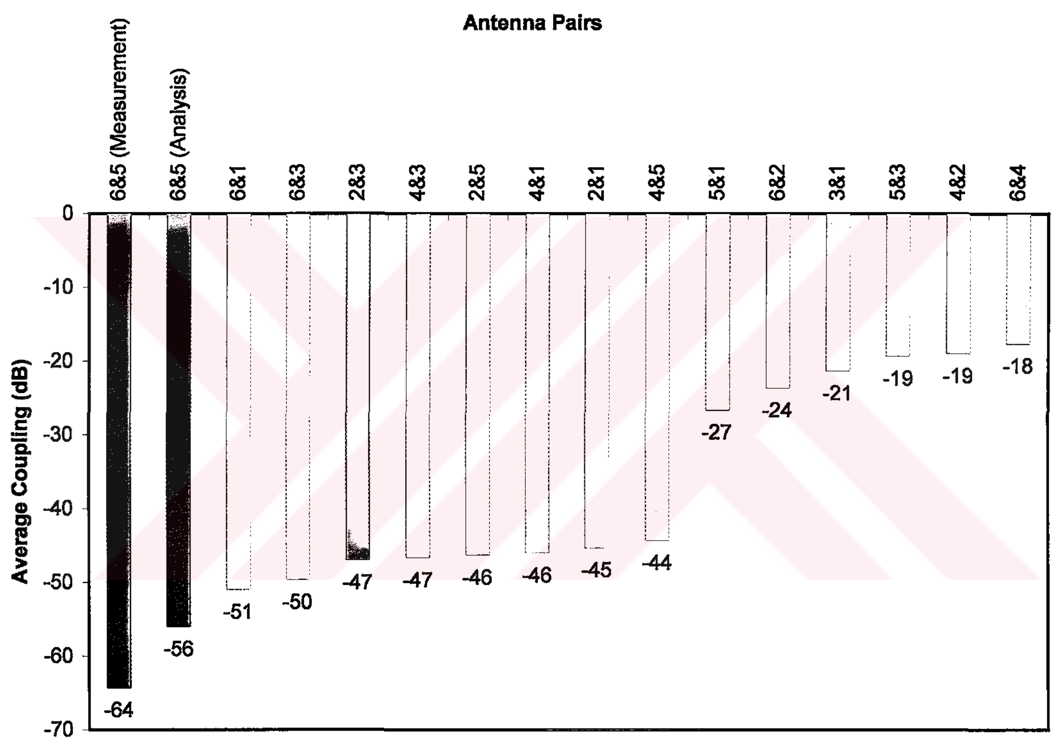

Figure 6.1: Average coupling mismatch loss of antenna pairs (CPGA: Green, CPMA:Purple)

It is seen that the average coupling value for the antenna positions six and five are evidently lower than the other eight sampled pairs. The average coupling value is at least 13 and mostly 46 dB's lower than the other antenna locations which is a good scale in terms of EMI avoidance. From these results it is possible to say that the genetic algorithm has done well in terms of finding the appropriate positions for the antenna pairs. It is easily seen that simply putting the antennas away from each other does not help much in decreasing EMI.

The next step in evaluation of the results is the comparison of the numerical analysis results with the measurement results. This step is important in terms of the numerical anlaysis' verification. The comparison is implemented for the antenna positions six and five at antenna measurment lengths of ten, five and two and a half centimeters.

In the next three figures there are 801 sample points for the measurement data. However, the numerical analysis coupling calculations are implemented for only for 80 equally-spaced frequencies between 70 and 280 MHz. The limited number of calculatios is due to the long duration of calculation. These calculated values are linear interpolated by a straight black line. Also note that the frequency axis range for the numerical analysis is 70-280 MHz while that for the measurement is 0.7-2.8GHz.

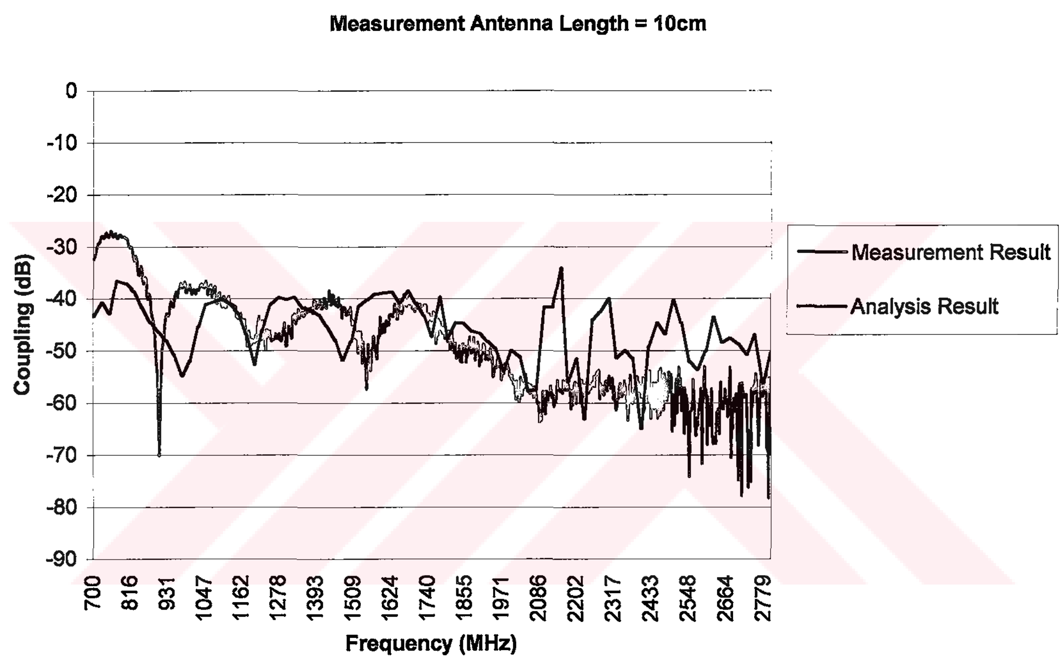

Figure 6.2: Numerical analysis results w.r.t. measurements for antenna length of 10 centimeters for the antenna pairs 6&5 with mismatch loss

In Figure 6.2, it is seen that the numerical analysis results are in 10 dB's deviation range with the measurement data in the 0.7-0.91 GHz range. This error is reasonable due to the irregularities in the model aircrafts fuselage and other measurement errors. Neglecting the error, it can be said that the proximity between the measurement and analysis lines is an indicator of the match of antenna lenght with the frequency. Between 1.1 and 2.1GHz, it is seen that the measured coupling follows the envelope of the numerical analysis with some shift. However, between 0.91-1.61 GHz, the analysis and measurement data are occasionally different up to 20dB's. The reason of this difference is mostly because that the segment lenght laws stated in the Numerical Analysis section are violated at higher frequencies. After 1.61 GHz it can be said that the numerical analysis results follows the path of measurement data with mismatch loss.

In Figure 6.3, it is seen that the numerical analysis results are in good agreement with the measurement data in the 1.4 - 1.9 GHz range. In this range it is also seen that the measured coupling with and without mismatch loss are also a good indicator of the match of antenna lenght with the propagation frequency. Also at 0.7 - 0.91 GHz range, the numerical analysis results match with the measurement results. This is due to the segment lenghts are longer than 0.1λ. After 1.9 GHz, the analysis and measurement data are occasionally different. The reason of this difference is mostly because that the segment lenght laws stated in the Numerical Analysis Section are violated at higher frequencies.

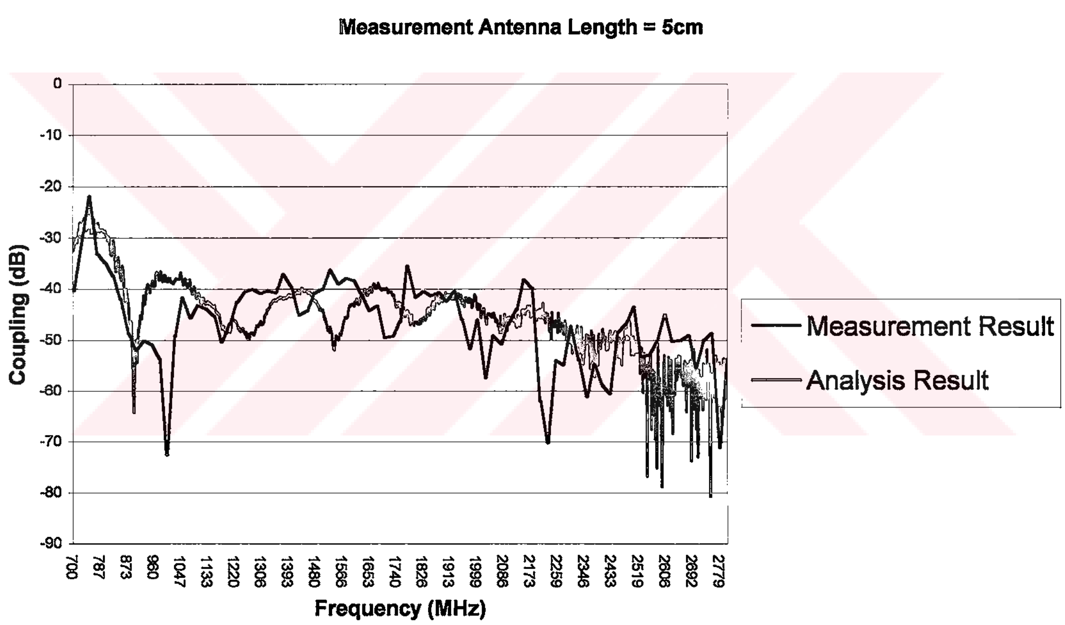

Figure 6.3: Numerical analysis results w.r.t. measurements for antenna length of five centimeters for the antenna pairs 6&5 with mismatch loss

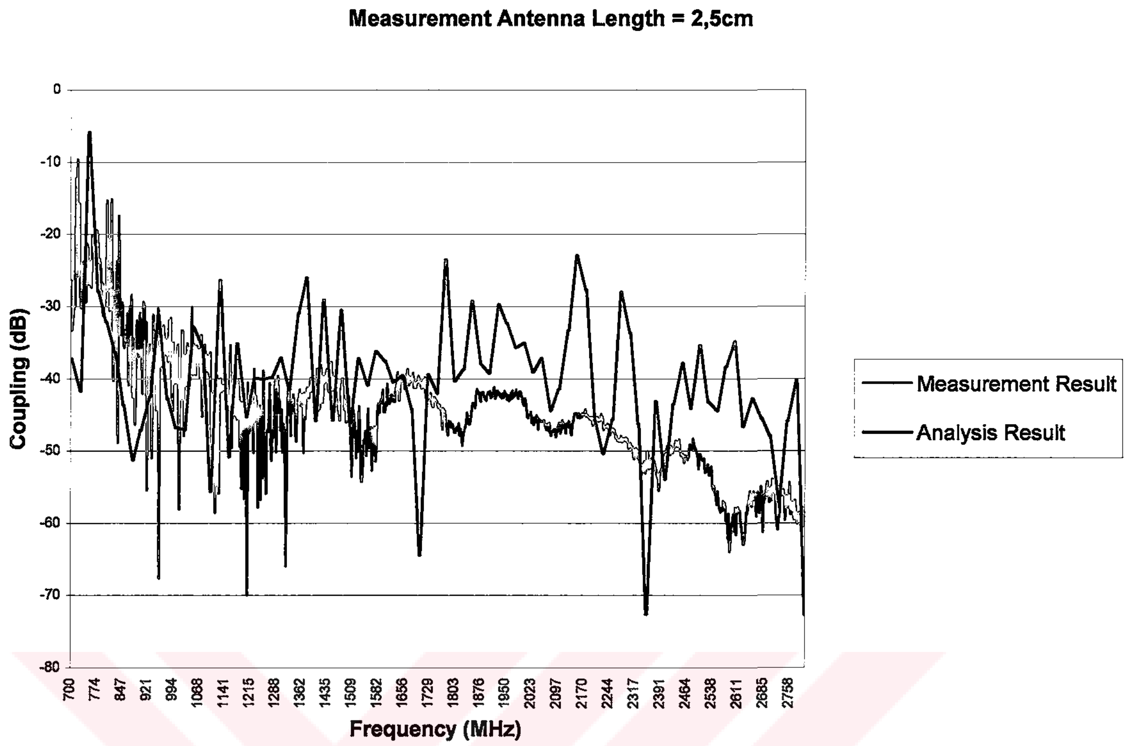

Figure 6.4: Numerical analysis results w.r.t. measurements for antenna length of two and a half centimeters for the antenna pairs 6&5 with mismatch loss

In Figure 6.4, it is seen that the numerical analysis results are in good agreement with the measurement data in the 0.7 - 2.2 GHz range. This is due to the segment lenghts are longer than 0.1λ. After 2.2 GHz, the analysis and measurement data are occasionally different in levels of +- 10dB's. However, the averaged values of numerical analysis results after 2.2 GHz are very close to the measurement results.

To summarize, it can be said that the numerical analysis' results follows the envelope of the measurement data. In the regions where the propagation frequency matches with the antenna length $\left(l = \lambda/4\right)$, the numerical analysis results are almost the same with the measurement data. However in some other regions, there are differences. But this is not important in terms of the numerical analysis' accuracy because, recalling the cost function in (4.88), the coupling is calculated at three different frequencies for three diffrent antennas. The numerical analysis is implemented in the regions where they match with the measurement data. In other words, if the antenna length is 1 meters in real world, the numerical analysis coupling (C_{70Mhz}) is calculated at 70 MHz only. This procedure is smilar for C_{140Mhz} and C_{280Mhz} coupling values for antenna lengths of 0.5 and 0.25 meters respectively. In these frequencies, the numerical analysis results matches exactly with the measurement data because the segmentation laws are applied exactly. Therefore the other differences between the analysis and measurement are not worth attention in terms of the accuracy of the procedures.

In this study a real life EMI problem has been investigated by using numerical analysis and measurement methods. The studies up to date generally consist of numerical analysis only. Also most of thesese studies have investigated antenna-to-antenna coupling only, neglecting the fuselage and the wings.

The innovation of this study is that it uses the one decade old GA search method for finding the suitable antenna positions on a F-4 Phantom by using the MoM for EM analysis. The procedure also includes the effects of aircraft's fuselage. From the results, it is seen that the calculated antenna positions meet the required EMI specifications in Section 3.2. Other random and "local minimum" positions are far from satisfying the desired performance. CPGA has proven very successful in searching for optimal solution in many areas where conventional model based approach is hard to be implemented. By implementing the CPGA, the EMI optimisation is shown to generate alternative optimal solutions, which may satisfy the requirements for the particular design.

The CPMA is also a successful search algorithm. Good results have been obtained in previous studies. However, for the present problem, it has been seen that the results are worse than that of the CPGA. The reason is that; there is a huge amount of discontinuity in the cost function calculated by the MoM. Therefore the amount of mutation is dominant in the search process. Some part of the mutation in CPGA is replaced by the local optimization in the CPMA. In this study, it was seen that the CPMA is more successful than the CPGA in finding the global minimum point.

Further studies in this field may be;

- A research on using different types of antennas instead of quarter wave monopole,
- Repetition of the measurements in the real-scaled anechoic chamber on a real F-4 Phantom aircraft
- Using other search techniqes such as the ant colony optimization, tabu search in the numerical analysis.

This study may also be helpful for future studies in the field as:

- Investigation of the effect of recently installed antennas or EMI sources on aircraft, boats and vehicles,
- Calculation and measurement of the radiation pattern an antenna which will be installed on the platform and,
- Design and implementation of EMI-free systems.

REFERENCES

[1] **Duff W.G.,** 1988. Electomagnetic Compatibility in Telecommunications, *Interference Control Technologies Inc.,* Gainesville, Virginia

[2] **Chatterton P.A. and Houlden, M.A.,** 1992. Electromagnetic Theory to Practical Design, *John Wiley&Sons Inc.*, Willshire, U.K.

[3] **Harrington, R.F.**, 1968. Field Computation by Moment Methods, *MacMillan*, New York

[4] **Holland J. H.,** 1992. Genetic Algorithms, *Scientific American*, **9**, 44-50

[5] **Caorsi S., Massa A., Pastorino M., Rafetto M. and Randazzo A.**, 2003. Detection of buried inhomogenius elliptic cylinders by a Memetic Algorithm, *IEEE Trans. Ant. And Prop.*, **51**, 2878-2884

[6] **Carter N.J.,** 1996. Aircraft EMC, the past, the present and the future: an overview, *EMC in Aerospace Digest,* **243**, 31 –37

[7] **Lee K. and Marin L.**, 1976. Broadband response of aircraft antennas, *Antennas and Propagation Society International Symposium*, **14**, 78 –79

[8] **Pelton E., Burnside W. and Wang N.,** 1978. Analysis for predicting near-field effects of on-aircraft antennas, *Antennas and Propagation Society International Symposium*, **16**, 81–84

[9] **Cooke W. and Ryan C. Jr.,** 1980. A GTD computer algorithm for computing the radiation patterns of aircraft-mounted antennas, *Antennas and Propagation Society International Symposium*, **18**, 631-634

[10] **Burnside W., Nan W. and Pelton E.,** 1980. Near-field pattern analysis of airborne antennas, *Antennas and Propagation*, **28**, 318–327

[11] **Givati, O. and Fourie, A.P.C.,** 1994. Radiation patterns of antennas mounted on a modified mirage aircraft, *AP-S. Digest* , **2**, 1158-1161

[12] **Kubina, S.J.**, 1983. Numerical modelling methods for predicting antenna performance on aircraft, *NATO AGARD*, 131-164

[13] **Orchard B.,** 1998. SuperNEC, *Poynting Software Inc.*, Cape Town, S.A.

[14] **Kubina S.J.**, 1988. *Numerical analysis and modelling techniques*, NATO AGARD , 225-257

[15] **Üstüner F.**, 2002. Analysis and simulation of antenna coupling on the UH-1 helicopter, *PhD Thesis,* Sakarya University, Adapazari

[16] **Obelleiro F., Taboada J.M., Landesea L., Castro I.T. and Rorriguez J.L.**, 2002. Determining near-field constraints for the synthesis of onboard array antennas, *Microwave and Optical Technology Letters*, **3**,34-39

[17] **Koper E.M. and Schneider S.W.**, 2004. Aircraft antenna coupling minimization using genetic algorithms and approximations, *IEEE Transactions on Aerospace and Electronic Systems*, **40**, 742-750

[18] **Haupt R. L.**, 1995. An ıntroduction to Genetic Algorithms for EM, *IEEE Antennas and Propagation Magazine*, **37**, 7-15design, *IEEE Antennas and Propagation*, **6**, 326-329

[19] **Günel T. and Kent S.**, 1998. An Optimization approach for the synthesis of microstrip radial stub, *AEÜ. Int. J. Electron. Commun.*, **52**, 337-340

[20] **Günel T. and Kent S.**, 1997. Dielectric permittivity estimation of cylindrical objects using genetic algorithm, *Journal of Microwave Power and Electromagnetic Energy*, **32**, 109-113

[21] **Günel T.**, 2000. An optimization approach to the synthesis of rectangular microstrip antenna elements with thick substrates for the specified far-field radiation pattern, *AEÜ. Int. J. Electron. Commun.*, **54**, 303-306

[22] **Günel T. and Aydemir M.E.**, 2002. Application of continuous parameter genetic algorithm to the problem of synthesizing bandpass distributed amplifiers, *AEÜ International Journal of Electronics and Communications*, Urban & Fischer Verlag, **5**, 351-354

[23] **Günel T., Aydemir M.E. and Karakuş G.**, 2001. Application of Genetic Algorithms to the synthesis of transmission lines for monolithic microwave ıntegrated circuits, *ELECO'2001 Second International Conference on Electrical and Electronics Engineering*, Bursa, 231-235

[24] **Aydemir M.E., Günel T., Erer I. and Kurnaz S.**, 2003. A novel method for SAR ımage processing using the genetic algorithm, *RAST'2003 International Conference on Recent Advances in Space Technologies*, November, Istanbul, 420-423

[25] **Günel T., Aydemir M.E. and Karaca A.E.**, 2001. Genetik Algoritma ile transmisyon hatlı empedans uydurucu devrelerin sentezi, *TMMOB Elektrik-Elektronik-Bilgisayar Mühendisliği 9. Ulusal Kongresi*, Kocaeli, 294-297

[26] **Günel T., Kent S., Aydemir M.E. and Kargın S.**, 2002. Genetik Algoritma ile yüksek mertebeden tomografik görüntüleme, *SIU'2002 10. Sinyal İşleme ve İletişim Uygulamaları Kurultayı*, Denizli, 818-823

[27] **Aydemir M.E., Günel T., Erer I., Kurnaz S. and Kargın S.**, 2005. SAR image processing by a Memetic Algorithm, *RAST'2005 International Conference on Recent Advances in Space Technologies*, June, Istanbul, 210-414

[28] **Mäkinen R.A.E., Neittaanmäki P., Periaux J. and Toivanen J.**,1998. A Genetic Algorithm for multiobjective design optimization in aerodynamics and electromagnetics computational fluid dynamics , *Proceedings of the ECCOMAS 98 Conference*, 258-264

[29] **Weile D. S. and Michielssen E.**, 1997. Genetic Algorithm optimization applied to electromagnetics: A review, *IEEE Transactions on Antennas and Propagation*, **45**, 343-353

[30] **Haupt R.L. and Haupt S.E.**, 1998. *Practical Genetic Algorithms*, Wiley

[31] **Johnson J.M. and Samii Y.R.**, 1994. Genetic algorithms and method of moments for the design of ıntegrated antennas, *IEEE Antennas and Prop.*,**28**, 326-329

[32] **http://www.militaryaircraft.de**

[33] **Gold, S. J.**, F-4 Technical Drawings, *Detail and Scale Inc.*, USA

[34] **Siegel M.Donald.**, 1976. Aircraft Antenna-Coupled Interference Analysis, *McDonnell Aircraft Company*, Missouri

[35] **Miller, E.K. et al.**, 1974. Report on an evaluation of computer program using integral equations for the electromagnetic analysis of thin wire structures, *Lawrence Livermore Laboratory*, CA

[36] **Ngan K.K.**, 2001. Design optimisation of a microstrip antenna using Genetic Algorithms, *MSc Thesis,* University of Warwick, Coventy

[37] **Winston P.H.**, 1992. Artificial Intelligence (3rd edition), *Addison-Wesley*, Wokingham

[38] **Dorigo M.**, 1992. Optimization, Learning and Natural Algorithms, *Ph.D.Thesis*, Politecnico di Milano, Italy

[39] **Glover R.**, 1989, Tabu Search - Part I, *ORSA Journal of Computing,* **3**, 190-206.

[40] **Metropolis N., Rosenbluth A., Rosenbluth M., Teller, A., and Teller, E.**, 1953. Equation of state calculations by fast computing machines, *Journal of Chemistry Physics,* **21**, 1087-1092

[41] **Coley D.A.,** 1999. An Introduction to Genetic Algorithms for scientists and engineer, *World Scientific Publishing*, Singapore,

[42] **http://www.genetic-programming.com**

[43] **Method of Moments Technical Reference Manual**, 1992. *Poynting Software Inc.*, Cape Town, South Africa

[44] **Yeh, Y.S. and Mei, K.K.,** 1967. Theory of conical equiangular spiral antennas, part i - numerical techniques, *IEEE Trans. Ant. and Prop.*, **15**, 634-641.

[45] **Wu, T.T. and King, R.W.P.**, 1976. The tapered antenna and its application to the junction problem for thin wires, *IEEE Trans. Ant. and Prop.*, **24**, 42-45

[46] **Ralston, A., A,** 1965. First Course in Numerical Analysis, *McGraw-Hill*, New York

[47] **Clayton R.P.,** 1981. EMC analysis at the equipment level, *Advisory Group for Aerospace Research & Development,* Lecture Series, **116,** Seine, France

[48] **Rockway J.W., Logan J.C. and Olsen R.G.**, 2003. EMC applications for expert MININEC, *EMC Society Newsletter.*

[49] **Nelder, J. A. and R. Mead,**1982. A Simplex Method for function minimization, *Computer Journal*, **7**, 308-313.

[50] **Dennis, J. E. Jr. and D. J. Woods,** 1987. New computing environments: microcomputers in large-scale computing, *SIAM*, 116-122.

[51] **Peng J., Balanis A.C.,** 1993. NEC and ESP codes: guidelines, limitations and EMC applications, *IEEE Transactions on Electromagnetic Compatibility,* **35**, 345-356

[52] **Standard Test Procedures for Antennas**, 1979. *IEEE Standard 149*, IEEE

[53] **Belrose, J.S.,** 1983, Scale modelling and full scale measurement techniques with particular reference to antennas in their operational environments, *NATO AGARD*, 131-165

[54] **Aydemir M.E., Günel T., Ustuner F,** 2004. F-4 Phantom uçağının VHF-UHF antenleri arasındaki kuplajın simülasyonu, HİTEK 2004, Havacılıkta İleri Teknolojiler Konferansı, İstanbul, 455-458

[55] **Aydemir M.E., Günel T.,** 2005 Electromagnetic Interference Supression between the GPS and IFF antennas on a UAV by Memetic Algorithm, IKS'2005 2nd International Conference on Intelligent Knowledge Systems, July 06-08, Istanbul, 145-149

BIOGRAPHY

Mustafa Emre AYDEMİR was born in Ankara in 1971. He completed his high-school education in Zonguldak, Ankara and Kayseri. He had a B.S. degree from Hacettepe University Department of Electronics Engineering in 1993. In 1994, he was commissioned as an Air Force Lieutenant and assigned to Turkish Air Force Academy, Yeşilyurt/İstanbul. He was awarded with an M.S. degree in 1998 from Bogazici University Department of Electronics Engineering. He has been giving many courses in the Department of Electronics Engineering in the Turkish Air Force Academy since 1995. He is mostly interested in the electromagnetic compatibility, microwaves, genetic algorithms and 8051 series microcontrollers. He is married and has one daughter.